INVESTIGATIONS OF SOLUTION-PROCESSED CUO NANOSTRUCTURES TOWARDS THE DEVELOPMENT OF WAVELENGTH TUNABLE PHOTODETECTORS

Ph.D. Thesis

By

AKASH TRIPATHI

DISCIPLINE OF ELECTRICAL ENGINEERING

INDIAN INSTITUTE OF TECHNOLOGY INDORE

May 2025

INVESTIGATIONS OF SOLUTION-PROCESSED CUO NANOSTRUCTURES TOWARDS THE DEVELOPMENT OF WAVELENGTH TUNABLE PHOTODETECTORS

A THESIS

Submitted in partial fulfillment of the
requirements for the award of the degree
of

DOCTOR OF PHILOSOPHY

by
AKASH TRIPATHI

DEPARTMENT OF ELECTRICAL ENGINEERING

INDIAN INSTITUTE OF TECHNOLOGY INDORE

May 2025

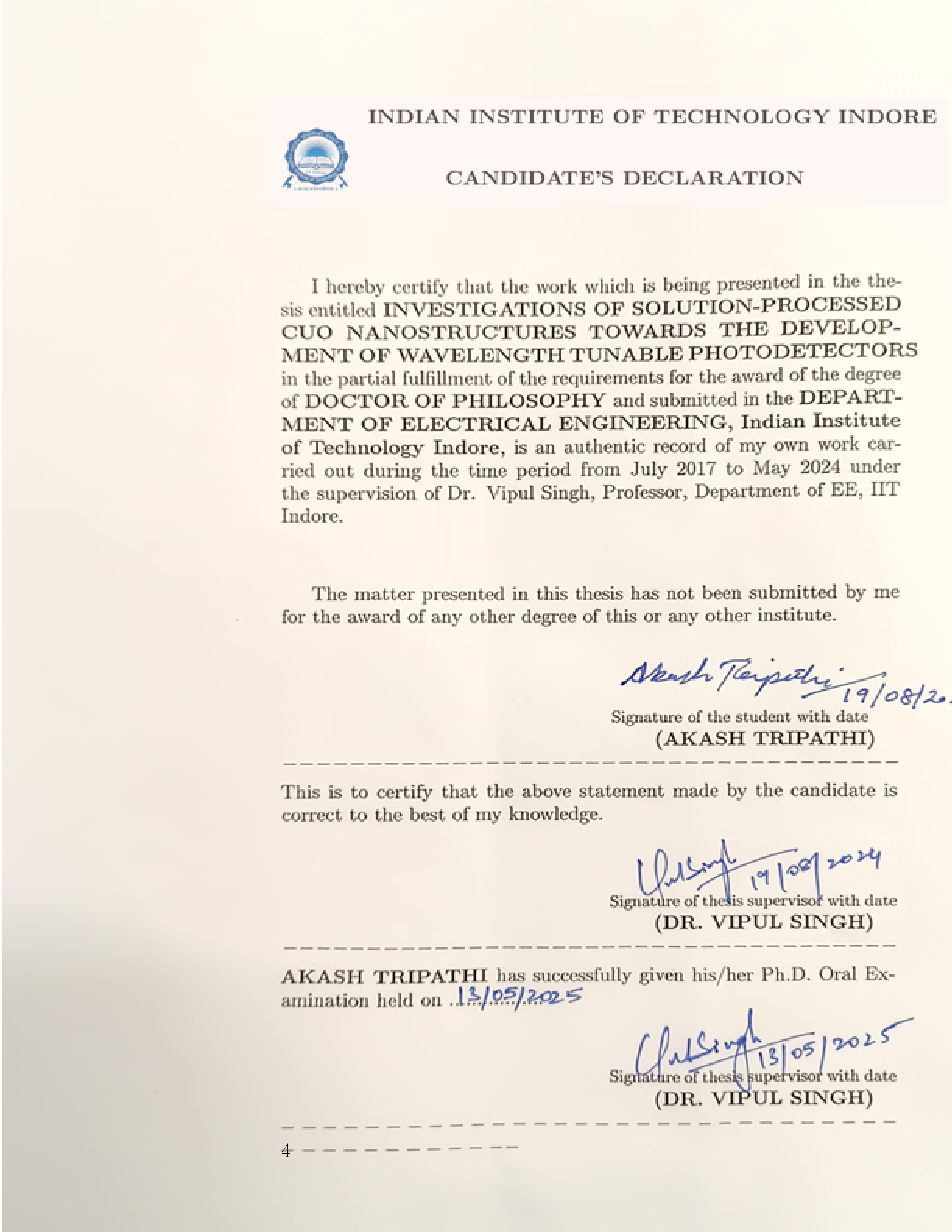

INDIAN INSTITUTE OF TECHNOLOGY INDORE

CANDIDATE'S DECLARATION

I hereby certify that the work which is being presented in the thesis entitled **INVESTIGATIONS OF SOLUTION-PROCESSED CUO NANOSTRUCTURES TOWARDS THE DEVELOPMENT OF WAVELENGTH TUNABLE PHOTODETECTORS** in the partial fulfillment of the requirements for the award of the degree of **DOCTOR OF PHILOSOPHY** and submitted in the **DEPARTMENT OF ELECTRICAL ENGINEERING, Indian Institute of Technology Indore**, is an authentic record of my own work carried out during the time period from July 2017 to May 2024 under the supervision of Dr. Vipul Singh, Professor, Department of EE, IIT Indore.

The matter presented in this thesis has not been submitted by me for the award of any other degree of this or any other institute.

Akash Tripathi 19/08/20

Signature of the student with date
(AKASH TRIPATHI)

- -

This is to certify that the above statement made by the candidate is correct to the best of my knowledge.

19/08/2024

Signature of thesis supervisor with date
(DR. VIPUL SINGH)

- -

AKASH TRIPATHI has successfully given his/her Ph.D. Oral Examination held on 13/05/2025

13/05/2025

Signature of thesis supervisor with date
(DR. VIPUL SINGH)

- -

ACKNOWLEDGMENTS

It's all grace of almighty that I got an opportunity to pursue a PhD from IIT Indore, an institute of excellence.

It is my sincere thankfulness towards my thesis supervisor **Dr. Vipul Singh**, who has given me an opportunity to explore this developing field of science and engineering. His emphasis on step-wise progress while achieving bigger goals is my key learning from him and is still in progress. His classroom teachings during the course work contributed to my understanding of concepts in semiconductor and device physics, which helped me immensely during the research work.

I express my deepest gratitude towards my parents **Late. Shri Jitendra Mohan Tripathi** and **Smt. Pushp Lata Tripathi** and other respected and beloved family members specially my brothers for all the sacrifices they made on my behalf and helping me achieve what I am today. They are a source of encouragement and inspiration to me throughout my life. This thesis was not possible without their support and help.

Pursuing PhD research work without the help of colleagues is not possible. I am thankful to my colleagues from the **Molecular and Nanoelectronics Research Group (MNRG)**, Dr. Tejendra Dixit, Dr. Jitesh Agrawal, Dr. Mayoorika Shukla Bharadwaj, Dr. Pramila, Dr. Shalu Chaudhary, Dr. Nidhi Yadav, Ms. Tejswini K. Lahane for their company and being supportive during my work. I would like to specially thank **Dr. Tejendra Dixit** for his all encouragements, ideas, and discussions in my research. I thank **Dr. Jitesh Agrawal** for his all support, discussions and being the help throughout my Ph.D.

My sincere thanks and appreciation to the PSPC (Ph.D. Student Progress Committee) members, **Dr. Abhinav Kranti** and **Dr. Preeti**

Bhobe for their precise observations and valuable suggestions to improve the quality of my doctoral work. I extend my gratitude to **Dr. M. S. R. Rao (IIT Madras)** for allowing me to access the research facilities in his well equipped laboratory.

I thank **SIC IIT Indore**, most specifically **Mr. Kinny Pandey**, **Mr. Nitin Upadhyay**, **Mr. Ravindra**, and **Mr. Ghanshyam** for their support.

I want to express my gratitude towards **Dr. Shilpa**, **Dr. P. Matkar** and other staff members of **Health Center**, IIT Indore, who, apart from all their general day's service, provided medical support during the COVID-19 pandemic.

I want to thank all staff members of IIT Indore for providing all comfort and convenience. Besides this, several people have knowingly and unknowingly helped me successfully complete this work.

Lastly, I also acknowledge **Council for Scientific and Industrial Research (CSIR)** for providing me with financial assistance.

Dated: Akash Tripathi

Dedicated

to

my family

ABSTRACT

One of the ways to sense this colourful world is by sensing different wavelengths of light emitted or reflected by different objects. Presently, photodetectors are crucial devices widely used to convert the emitted photons into electrical energy. In recent times, there has been immense emphasis given to fabricating photodetectors with wavelength tunability. The research on semiconductor-based photodetectors with UV-C (200 nm-280 nm), wideband [i.e., UV-C to near-infrared (NIR) (up to 1000 nm)], and multi-band or dual-band spectra has been given immense importance for a wide range of applications by the scientific community. A common approach for fabricating broadband photodetectors is to form heterojunctions between the high and low-bandgap semiconductors. Recently, high-performance photodetectors based on hetero-junctions of perovskites and 2D materials with other semiconductors, such as ZnO, NiO, etc., have been reported. However, these semiconductors have certain associated disadvantages, viz., instability of perovskites in the ambient environment and a dearth of a facile technique for the synthesis of graphene (other 2D material systems). Therefore, solution-processed metal-oxide-based photodetectors possess major advantages, viz., facile and low-cost synthesis process and stability toward the ambient environment.

Generally, metal-oxides are intrinsically n-type semiconductors and for device fabrication, incorporation of p-type character through doping poses certain challenges such as self-compensation, instability, and reproducibility. Therefore, CuO has gained the attention of the research community due to its intrinsic p-type character that has been utilised for optoelectronic applications and possesses both an indirect bandgap (1 eV-1.4 eV) and a direct bandgap (2 eV-4 eV). The range of bandgap offered by pristine CuO can be utilised to tune the optoelectronic properties, and further, it can be made useful in different optoelectronic

applications.

The performance of the photodetector is graded on the basis of certain parameters such as responsivity, sensitivity, and detectivity, which should desirably be at higher values, and the transient response should be faster. Lately, the sluggish response of the device has found future applications in optical memory and neuromorphic computation. One of the reasons for the slow response of photodetector is a phenomenon known as persistent photoconductivity (PPC).

Bandgap engineering is a technique that has been utilised to tune the bandgap of semiconductors to improve the device performance of solar cells, photodetectors, LEDs, gas sensing, biosensing, etc. There are several methods, such as doping, alloying, and morphological modification, which have been used to tune the bandgap of a material. However, techniques such as doping and alloying are complex processes, and therefore, morphological modification is the right option for tuning the optical bandgap of CuO.

In this thesis, we have employed hydrothermal techniques to synthesise bandgap tunable CuO semiconductors and fabricated UV-C, broadband, and NIR photodetectors. The smooth CuO thin-film-based UV-C solar-blind photodetector was fabricated, and its performance was improved by fabricating a nanostructures-based device. A unique phenomenon of persistent photoconductivity was employed to achieve a set and reset mechanisms for optical memory application.

Lastly, a morphological transition engineering technique was developed for the synthesis of CuO nanostructures. This technique was employed to improve the performance of the CuO smooth thin-film-based photodetector.

List of publications

(A) Peer-reviewed Journals

A1. Peer-reviewed Journals: From Thesis Work

1. Tejendra Dixit*, **Akash Tripathi***, Swanand V. Solanke, K. L. Ganapathi, M. S. Ramachandra Rao, and Vipul Singh, Solution-Processed Transparent CuO Thin Films for Solar-Blind Photodetection, *IEEE Electron Device Letters*, vol. 40, 2, 255-258, 2019.

2. **Akash Tripathi***, Tejendra Dixit*, Jitesh Agrawal and Vipul Singh, Bandgap engineering in CuO nanostructures: Dual-band, broadband, and UV-C photodetectors, *Appl. Phys. Lett.*, 116, 111102, 2020.

3. **Akash Tripathi**, Jitesh Agrawal, Tejendra Dixit and Vipul Singh, Trap Assisted Persistent Photo-Conductivity in Solution-Processed CuO Thin Film, *IEEE Journal of Quantum Electronics*, vol. 56, 1, 7000105, 2020.

4. Tejendra Dixit*, **Akash Tripathi***, Swanand V. Solanke, K. L. Ganapathi, M. S. Ramachandra Rao, and Vipul Singh, Solution-Processed Transparent CuO Thin Films for Solar-Blind Photodetection, *IEEE Electron Device Letters*, vol. 41, 12, 1790-1793, 2020.

A2. Peer-reviewed Journals (under review): From Thesis Work

1. **Akash Tripathi**, Vipul Singh, Post-synthesis Morphological Transition Engineering A Novel Technique for the Synthesis of

CuO Nanostructures for Improved Photoresponse, *IEEE Transactions on Nanotechnology*, under review since 28 May 2024.

A3. Peer-reviewed Journals: Outside of Thesis Work

1. Tejendra Dixit*, **Akash Tripathi***, K. L. Ganapathi, M. S. Ramachandra Rao, and Vipul Singh, Long-Lasting Persistent Photoconductivity in Au/CuO Thin Films for Optical Memory, *IEEE Photonic Technology Letters*, vol. 41, 12, 1790-1793, 2020.

(* Equally Contirbuted Authors)

(B) Conference Proceedings

1. **Akash Tripathi**, Tejendra Dixit, I. A. Palani and Vipul Singh, “Optoelectronic Applications of CuO Nanoleaves and Nanowalls Synthesized by Poly(ethylene glycol) Assisted Hydrothermal Method”, *Indo-Japan Workshop on Biomolecular Electronics-2018*, National Physical Laboratory, New Delhi.

2. **Akash Tripathi**, Jitesh Agrawal, Tejendra Dixit, I. A. Palani and Vipul Singh, “Evidence of Large and Persistent Photoconductivity in CuO Thin Films”, *ICMAT-2019*, National Technical University, Singapore.

3. **Akash Tripathi**, Jitesh Agrawal, Tejendra Dixit and Vipul Singh, “Solution-Processed Ultrawide Bandgap CuO

Nanostructure", *International Conference on Precision, Meso, Micro and Nano Engineering-2019 (COPEN-11)*, Indian Institute Technology Indore, India.

4. **Akash Tripathi**, Tejendra Dixit and Vipul Singh, "Development of CuO nanostructures-based dualband photodetector", *12th JKJSBT-2019*, Kyushu Institute of Technology, Japan.

5. **Akash Tripathi**, Tejendra Dixit and Vipul Singh, "Development of CuO nanostructures-based braodband photodetector", *2nd ASCB-2019*, Kyushu Institute of Technology, Japan.

Contents

List of Figures

List of Tables

List of Abbreviations

PD: Photodetector

IR: Infrared

UV: Ultravoilet

NIR: Near Infrared

R: Photoresponsivity

S: Photosensivity

D^*: Specific detectivity

EQE: External Quantum Efficiency

FESEM: Field Effect Scanning Electron Microscopy

XRD: X-ray diffraction

UV-Vis: Ultraviolet-Visible

DRS: Diffused Reflectance Spectroscopy

PVD: Physical Vapour Deposition

XPS: X-ray Photoelectron Spectroscopy

DOS: Density of States

LED: Light Emitting Diode

DI: Deionised

PPC: Persistent Photoconductivity

MTE: Morphological Transition Engineering

List of Symbols

λ: Threshold voltage

E_v: Valene band maxima

E_c: Conduction band minima

E_g: Bandgap

V_{gs} and:and Gate to source voltage

Chapter 1

Introduction

1.1 Photodetector

The consciousness towards the universe is possible by sensing it. One of the most prominent sensory organs in living beings is the eyes. The eyes capture the light incident on it. The captured lights are converted into electrical signals and transmitted to the mind to be processed into meaningful information. The mind interprets different wavelengths of light corresponding to their colour.

Therefore, the means to sense this colourful world is by sensing the different wavelengths (λ) of light emitted or reflected by different objects. The device which converts the photons into electrical energy is known as a photodetector (PD). Semiconductor-based PDs find wide usage because of their advantages over others, including their simple design, compact size, and miniaturisation ability. PDs are made from various semiconductors, including Si, GaAs, GaN, ZnO, Ga_2O_3, etc. The working spectrum of the device is determined by the semiconductor selection and its bandgap. Henceforth, the devices' spectrum offering plays a crucial role in deciding their applications, such as imaging, missile detection, fire detection, optical communication, etc [1-3].

Depending upon the sensitive range of the PD in the electromagnetic spectrum, PDs can be classified as:

- **IR Photodetector**: The electromagnetic spectrum's infrared (IR) region is from 750 nm to 1 mm wavelength. The PD working in this region is known to be an IR PD. The whole IR region has been further divided into three regions: near-IR (NIR, 750 nm to 3 μm), mid-IR (MIR, 3–15 μm), and far-IR (FIR, 15 μm to 1 mm). The IR PDs have been widely used in modern multifunctional technologies such as thermal imaging, biomedical imaging, night vision, information communication, and military [4-5].

- **Visible Photodetector**: The visible light falls in the range from 400 nm to 750 nm, and the PD active in this region is known as visible light PD. The application of visible light PD has been in telecommunications, video imaging, and artificial vision [6,7].

- **UV Photodetector**: The PD is sensitive to ultraviolet (UV) light, which falls in the range from 10 nm to 380 nm wavelength. UV photodetection has applications in ozone layer monitoring, flame detection, missile tracking, and terrestrial communication [8, 9].

Semiconductors are materials with a bandgap of 1 eV to 6 eV. PDs based on semiconductors work on the phenomenon of conductivity change of the semiconductor when exposed to the light source of the appropriate wavelength. Here, the choice of the proper wavelength of light depends mainly on the semiconductor's bandgap. Before further discussion, below are a few terminologies defined:

- **Valence band**: The valence band of the semiconductor is the available set of ground energy states of electrons confined by the highest allowed energy states, which is called the valence level

(E_v). The electrons in this band do not participate in the conduction of electricity.

- **Conduction band**: The conduction band of the semiconductor is defined by the available excited energy states of electrons confined by the lowest allowed energy level, which is called the conduction level (E_c). The electrons of the conduction band are free to move and participate in the conduction of electricity.

- **Bandgap**: The difference between the conduction band level and valence band level is called the bandgap of a semiconductor (E_g=E_c-E_v).

The basic working of semiconductor-based PDs is based on the phenomenon of change in conductivity of the active area of the device in response to the light source. As the appropriate wavelength of light falls on the semiconductor, the valence band electrons get excited to the conduction band, resulting in enhanced conductivity. Figure 1.1 (a) shows the PD device schematic when the bias is off in the dark condition with the semiconductor energy band levels. In this condition, there will be scant free charge carriers, and hence, the conductivity of the semiconductor will be lower. As light falls on the semiconductor, the electrons from the valence band are excited to the conduction band, leaving behind holes in the valence band (Figure 1.1 (b)). Now, as the bias applies across the metal electrodes, there will be a flow of charge carriers due to the potential gradient (Figure 1.1 (c)).

The performance of a PD is evaluated on the basis of the figure of merit of the device as defined below:

- **Photoresponsivity (R(λ), mA/W)**: It is the amount of photocurrent generated per unit incident light power. The following equation is used for the calculation of photoresponsivity:

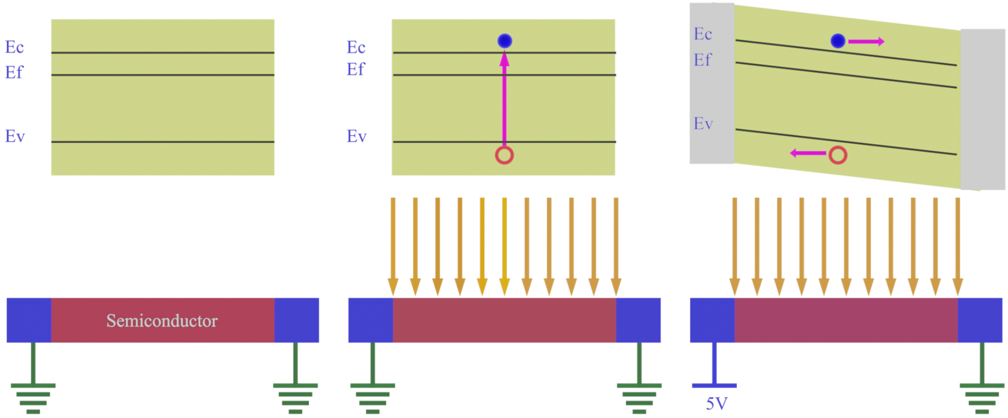

Figure 1.1: PD schematic and energy band levels of semiconductor a) without any external bias or photo-excitation, b) without any external bias and photo-excitation, and c) applied with external bias and under photo-excitation.

$$R(\lambda) = \frac{(I_{ph} - I_d)}{P} \tag{1.1}$$

where I_{ph} is the current after illumination with light of wavelength k, I_d is the dark current, and P is the power of light incident on the device.

- **Photosensitivity (S**(λ): It is the ratio of photocurrent generated to the dark current of the device and given by the following equation:

$$S(\lambda) = \frac{(I_{ph} - I_d)}{I_d} \tag{1.2}$$

- **Specific detectivity (D*, cmHz$^{0.5}$W^{-1} or Jones)**: It is the smallest detectable signal, equivalent to noise normalised to a bandwidth of 1 Hz and an area of 1 cm^2 (Ref. 11) and is given by the following equation:

$$D^* = \frac{(A)}{(2qI_d)}^{0.5} R(\lambda) \tag{1.3}$$

where A is the area of the channel region, and q is the electronic charge.

- **External Quantum Efficiency (EQE, %)**: It is the number of photonically generated charge carriers reaching to the electrodes per photon incident. It is given by equation (4):

$$EQE = \frac{hcI_{ph}}{e\lambda P} \tag{1.4}$$

Further, the categorisation of the PDs is done based on the nature of the photo-response curve. Here, the photo-response curve of the PD is the plot of the values of the particular parameter against the corresponding wavelength of the incident light, which is called the PD response curve. These specific categories of PDs have niche applications.

1.1.1 Classification of photodetectors

Device architecture-based classification

Based upon the basic device architecture or configuration, the PD device can broadly have the following types:

- **Plannar symmetric electrode PD**: These have a simple architecture device configuration. The light-sensitive semiconductor active layer is sandwiched between two electrodes side by side in the planar configuration, as shown in Figure 1.2 (a).
- **Lateral electrodes PD**: The light-sensitive semiconductor active layer is sandwiched between two electrodes in the lateral configuration (Figure 1.2 (b)).

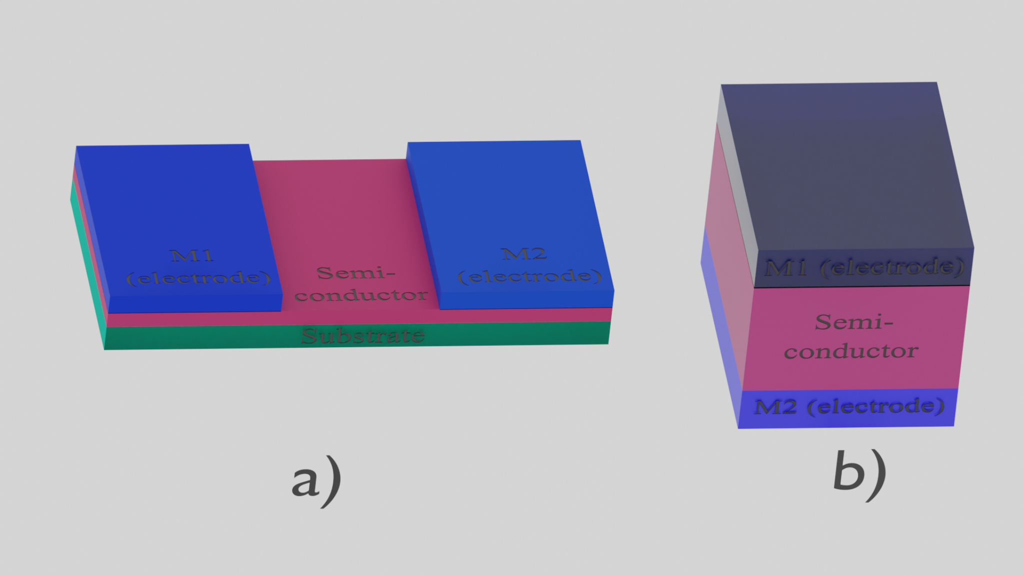

Figure 1.2: Schematic for basic device architecture a). planar or lateral electrode, and b). vertical electrode configuration, respectively

Device physics-based classification

The PDs can be fabricated by selecting different combinations of semiconductors and electrodes. These combinations of materials give rise to different underlying device physics. Therefore, based on the device physics, the following are the classifications of PDs:

- **Photoconductor**: The photoconductor configuration consists of two symmetrical ohmic contacts deposited over the active layer of the device. An external bias voltage is applied to drift the photo-excited electrons and holes towards their respective electrodes, which leads to the flow of photocurrent. Usually, one type of photo-excited charge carrier is trapped by a variety of defects or trap states in the bandgap of the active layer, which significantly increases the lifetime of the charge carriers and facilitates the recirculation of other charge carriers in the external circuit, resulting in higher responsivity.

- **Photodiodes**: The photodiode consists of a pn junction between a p-type and n-type semiconductor or a Schottky junction between a semiconductor and metal. The built-in the electric field at the interface drifts the photo-excited charge carriers in opposite directions, towards their respective electrodes to generate photocurrent.

- **Phototransistors**: Phototransistors are generally used as optoelectronic amplifiers and switches in which the output signal can be amplified and modulated by incident light.

Spectral response-based classification

The characteristic response curve corresponding to the wavelength of incident light on the PD is used to classify them. Based on the nature of the response curve, the PD can be classified into the following categories:

- **Broadband photodetector**: Broadband photodetectors are those devices which are sensitive to larger sets of wavelengths with a single flat band response curve. Figure 1.2 (a) shows a schematic of a broadband response curve sensitive within the band from λ_1 to λ_2. These devices have varied applications in machine vision, artificial eyes, and telecommunication [10].

- **Multiband or dual-band photodetector**: When the sensitivity of the photodetector is within two or more bands of wavelength, it is a multiband or dual-band photodetector. The response curve of the device has multiple bands of sensitivity (Figure 1.2 (b)). These photodetectors have applications in environmental monitoring and machine vision [11].

- **Solarblind photodetector**: Solarblind PDs are immune to solar interference by rejecting the light with λ>280 nm. Due to immu-

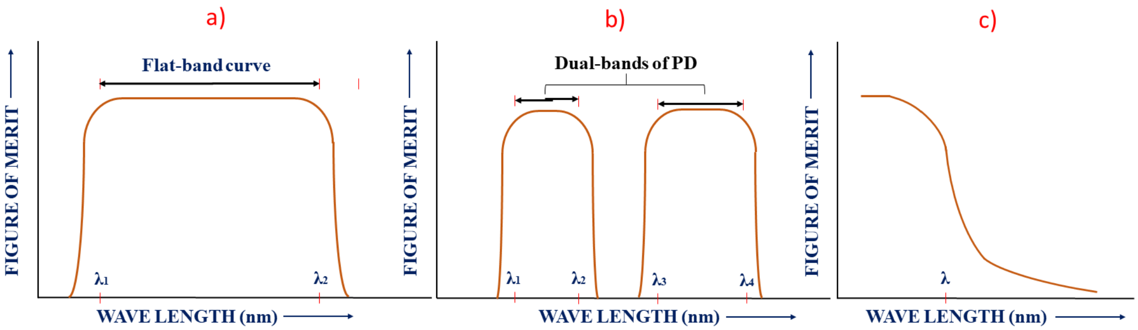

Figure 1.3: Response curve schematic representing a). broadband, b). multiband or dualband and c) solarblind photodetectors.

nity from background noise, solar-blind deep-ultraviolet (DUV) PD performance is better compared to other PDs with similar figures of merit [12]. These PDs have potential applications in satellite communication, UV astronomy, military defence, and flame and missile plume detection [13].

Currently, Si-based photodetectors and photomultipliers are generally used as commercial UV, visible and NIR photodetectors due to their extremely mature processing techniques and per unit low-cost manufacturing. However, due to the smaller bandgap of 1.1 eV to 1.3 eV, intrinsic Si can only be used for detection in the visible and near-infrared (NIR) spectral range. Silicon-based devices also have low intrinsic quantum efficiency and poor robustness. Additionally, with the continuous evolution of technology, the demand for high-performing photodetectors have been increasing in diverse applications. Moreover, conventional Si-based photodetectors could not fulfil the requirements of emerging portable and wearable optoelectronic technologies, such as low manufacturing cost, transparency and flexibility. Therefore, to satisfy the need for modern UV photodetectors, wideband metal oxide semiconductors like WO_3, SnO_2, NiO, ZnO, Nb_2O_5 and Ga_2O_3 etc. have been explored. The wide bandgap semiconducting materials exhibit strong radiation hardness and high thermal and chemical stability;

therefore can be used in a harsh environment.

1.2 Cupric Oxide (CuO)

Cupric oxide (CuO), which is derived from the abundantly available copper in the Earth's crust, has garnered significant attention in transition metal-oxide research due to its intriguing characteristics as a p-type semiconductor with a small bandgap (1.2 eV in bulk) [1]. Moreover, CuO is fundamental to various high-temperature superconductors, and as a component of extensive magnetoresistance material, it is a thoroughly researched material system [15-22]. Due to its high theoretical capacity, safety, and environmental friendliness, CuO nanostructures are also regarded as electrode materials for advanced rechargeable lithium-ion batteries [23]. Perhaps CuO has potential applications in gas sensors, bio-sensors, solar cells, field emissions, supercapacitors, removal of inorganic pollutants, and magnetic storage media [24-30].

Although CuO has been explored for the above-mentioned application, its characteristics for optoelectronic applications have been comparatively less explored. It has been

1.2.1 CuO lattice structure

The electronic shell configurations of Cu and O are [Ar]$3d^{10}4s^1$ and [He]$2s^2 2p^4$, respectively. CuO is a transition metal-oxide with a monoclinic crystal structure [1, 34]. Figure 1.3 shows the crystal structure in which one Cu atom is coordinated by four coplanar O atoms forming a parallelogram, while O is coordinated by four Cu atoms forming a distorted tetrahedron. The dimensions of unit cell are a=4.7, b=3.4, c=5.1, β=99.5°, Cu and O bond length=1.96 [35, 36].

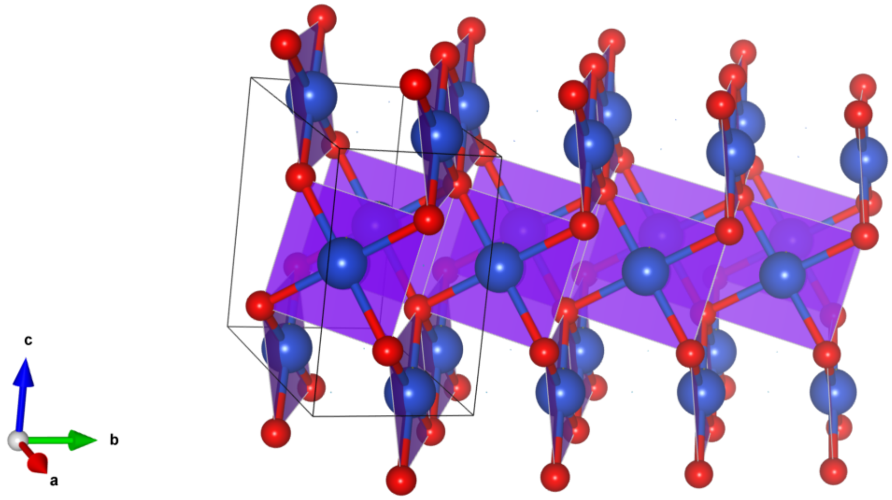

Figure 1.4: Monoclinic lattice structure of CuO.

1.2.2 Band structure and optoelectronic properties of CuO

Although CuO has been known among transition metal-oxides since earlier, its convincing electronic band structure has been scantly reported [36]. CuO falls under the category of compounds known as Mott insulators, where general band theory fails. There have been some preliminary theoretical studies to predict the electronic band structure, but their results could not verify the experimental results [35, 37, 38].

1.2.3 Magnetic property

The bulk transition metal monoxides, including MnO, FeO, CoO, NiO, and CuO, are all antiferromagnets, where CuO occupies a special place because of its unique magnetic properties. Unlike MnO, FeO, CoO, and NiO, CuO has a low-symmetry monoclinic crystal structure and a magnetic susceptibility temperature behaviour that is unusual for 3d antiferromagnets.

1.2.4 Transport mechanism

The polaron hopping mechanism is predominantly found responsible for charge transport in CuO semiconductors at room temperature. In this type of transport mechanism, the mobility of the charge carriers is very low. However, due to the higher concentration of defects in CuO, the concentration of holes is prominently high [39-41].

Defect-induced thermal activation and space charge limited current (SCLC) are the transport mechanisms responsible at room temperature [39, 42].

1.3 Challenges

In today's perspective, to cater to future applications, there is a quest for semiconductors which offer a wide range of bandgaps upon which different PDs could be fabricated. However, tuning the bandgap of semiconductors for specific applications is done either through doping of semiconductors or sandwiching of two semiconductors with different combinations of bandgaps [12, 30, 32]. Although these are well-practised methods, they are associated with the problem of synthesis process complexity. Alternatively, tuning the surface morphology of the semiconductor can be used to modify the bandgap effectively [32, 33].

Metal-oxide semiconductors offer various morphology nanostructures suitable for tuning the optoelectronic properties.

Very little study on the band structure of CuO; therefore, only recently has it gained attention concerning its optoelectronic applications. CuO has a direct bandgap transition (1.2 eV) as well as an indirect bandgap (2 eV) transition. Initially, it was largely believed that CuO could only have a bandgap as large as 3 eV. However, Palker et al. reported size-dependent phase transition in CuO, and they argued that at smaller sizes Cu_2O phase was more stable. Further, as different research groups reported, the synthesis of CuO nanostructures with the absorption bandgap varied from the NIR to the visible to the UV region [43-46].

Usually, researchers have used basic 1D nanostructures such as nanorods, nanopillars, nanocolumns, nanotubes, etc., for the development of photodetectors, which eventually could not generate high sensing responses due to their low charge transportation efficiency and several other factors. Therefore, it has become quite critical to synthesise more complex nanostructures that could provide a larger surface area and better charge transportation between the electrodes at lower fabrication costs. However, developing such a high-responsivity and low-cost broadband photodetector is still a big challenge.

Therefore, for the development of UV-C to visible and NIR light detection, the development of tunable bandgap nanostructures over the glass substrate is highly likely. For the adhesivity of CuO over the glass substrate, the seed layer-assisted growth is required.

As several reports suggest the deep UV absorption [45, 46], the demonstration of CuO-based solar-blind UV-C photodetector can pave the way for attracting the interest of the scientific and engineering community to carry on further research on optoelectronic properties and applications of CuO.

1.4 Review of past work

CuO has both indirect and direct bandgap transitions with 1.2 eV and 2 eV E_g values. However, the E_g of the CuO has been reported widely from 1.2 eV to 3.02 eV for nanostructures. The highest E_g is reported as high as of 4.13 eV for CuO quantum dots. Therefore, there are enough reports suggesting the tunability of the bandgap in CuO depending upon the synthesising process, morphology, and size of the nanostructure.

The I–V characteristics of the single CuO nanowire photodetector device were measured in a dark room and under white illumination with different light intensities. The conductance exhibits a relative increase of 25–87% for light intensities from 1.62 $mWcm^{-2}$ to 45 $mWcm^{-2}$, respectively. Remarkably, an IR photodetector based on CuO nanowires has been successfully fabricated and investigated by Wang et al. [94] reported a visible light photodetector made of mesoporous CuO dandelion structures synthesised by a simple template-free hydrothermal route. Therefore, the present status of the CuO-based photodetector indicates that it can be explored for varied wavelength-tunable devices sensitive from NIR to UV-C spectral region.

1.5 Objectives of this work

The main objective of this work is to develop and utilise the direct as well as indirect bandgap of CuO to fabricate high-performance UV-C, broadband and NIR photodetectors. The goals of this work in detail are as follows:

1. To control and tune the morphology of CuO nanostructures of hydrothermally grown ZnO nanostructures for the fabrication of UV-C, broadband and NIR photodetectors.

2. To fabricate a smooth thin-film-based UV-C solar-blind photodetector and investigate the persistent photoconductivity (PPC) effect.

3. To develop a high-performance nanostructure-based UV-C solar-blind photodetector.

4. To develop an environmentally benign technique for the synthesis of CuO nanostructures for the improvement of the device's performance.

1.6 Organisation of the thesis

1. **Chapter 1** includes the introduction to a different class and the working principle of a photodetector. A detailed discussion about the material properties and transport mechanisms has been done.

2. **Chapter 2** discussed the material and the deposition process used during this work. Further, the different structural and optical techniques used for device characterisation have been briefly discussed.

3. **Chapter 3** discusses the hydrothermal growth to control and tune the CuO nanostructures by using additives in the precursor solution. The fabrication of UV-C, broadband and NIR photodetectors has also been discussed.

4. **Chapter 4** has demonstrated CuO thin-film-based UV-C solar-blind photodetectors with the investigations on PPC effect.

5. **Chapter 5** has developed a high-performance nanostructure-based UV-C solar-blind photodetector.

6. **Chapter 6** has developed an environmentally benign technique for the synthesis of CuO nanostructures and demonstrated its usage for the improvement of the device's performance.

7. **Chapter 7** is the conclusion of the work that has been presented in the thesis and a small description of the future scope of this work.

1.7 Thesis Contributions

The key contributions of this thesis are to (i) exploration new optoelectronic CuO-based device applications, (ii) tune the bandgap of CuO for the fabrication of UV-C, broadband, and NIR photodetector, (iii) fabricate CuO-based UV-C solar-blind photodetector as well as improve its performance to comparable levels with devices based on other established wide-bandgap semiconductors for UV-C photodetection, (iv) developed PPC photonic set and reset mechanism for optical memory application, and (v) developed an environmentally benign technique for the post morphological transition engineering for transforming CuO thin-film to nanostructure.

Chapter 2

Experimental methods and characterisation techniques

2.1 Introduction

Several key points need to be considered for the development of photodetector devices, like the selection of proper material, the material synthesis and deposition processes and the characterisation techniques used to evaluate various device parameters. This chapter discussed a variety of materials employed in the presented research work. Further, it describes various material synthesis and nanostructures fabrication processes. After that, different characterisation tools used throughout the work are discussed in detail. This chapter discusses the synthesis methods of the CuO semiconductor and the other experimental details. Further, to investigate the phase purity and other properties of the semiconductor, different spectroscopic techniques such as XRD, Raman spectroscopy, Field emission secondary electron microscopy (FESEM), UV-vis absorption spectroscopy, and X-ray photoelectron spectroscopy (XPS) were performed. Upon optimisation of the CuO semiconductor synthesis process, the photodetector device was fabricated. Electrodes of the devices were deposited by the thermal evaporation technique (physical vapour deposition). The electrical characterisation of the devices was first performed, followed by optical characterisation. The experiments and characterisation techniques followed are discussed in the following subsections.

2.2 Materials used for device fabrication

The device's physics is governed by the materials used for the fabrication; therefore, choosing the proper materials is the criterion for efficient device performance. The selection of the materials for the active layer of the device is done in such a manner that satisfies the necessary conditions of the energy bandgap, energy levels, and absorption spectra peaks. For the design of different types of photodetectors, it is decisive to select the material capable of offering different bandgaps and, accordingly, having strong absorption for the particular set of wavelengths. All the materials are used as it is acquired from the vendor without any further treatment.

2.2.1 CuO

Copper Oxide (cupric oxide, CuO) is a metal oxide semiconductor with excellent electrical, optical and magnetic properties. It has a monoclinic crystal structure with a varied bandgap ranging from 1 eV to 4 eV. As the CuO semiconductor has an intrinsically variable bandgap, it is potentially applicable for a large electromagnetic spectrum (NIR to UV). For the sake of device fabrication, the CuO semiconductor was deposited over the glass substrate through the hydrothermal process.

2.2.2 Gold (Au)

Au is a noble metal usually used for making electrical contacts in devices since it is non-reactive in ambient conditions. As Au has a work function of 5.1 eV, it is widely used to make ohmic contact with CuO semiconductor-based devices. PVD technique was employed to deposit it, and the boiling point was 2700 °C.

2.2.3 Copper (Cu)

Cu is a relatively low-cost metal that has been used to form contact with CuO semiconductors. It has a work function of 4.7 eV. It is deposited by the PVD technique and has a boiling point of 2600 °C.

2.3 Substrate preparation

2.3.1 Glass substrate cleaning process

Substrate cleaning has been regarded as one of the most basic and critical steps for device fabrication. This is because commercially available materials are contaminated with different kinds of impurities. During the process of manufacturing, packaging and transportation, the surface of substrate material gets congregated by the layers of organic and inorganic impurities. However, for the purpose of device fabrication, the quality of semiconductor deposition has to be ensured. Even the smallest traces of contamination lead to undesired distortions and defects in the crystal lattice. Therefore, a multi-step cleaning process has to be followed to eliminate all undesired contaminations from the surface of the substrate.

In this work, commercially available borosilicate glass has been used as a substrate since it has properties such as a smooth surface, chemically inert in ambient conditions, and transparent to visible light. For the device fabrication, 1.5 cm×1.5 cm×0.1 cm pieces of glass were cleaned to ensure the surface of the glass substrate is rid of all impurities. To clean the samples, they were dipped in an ultrasonic bath of acetone, isopropanol and deionised (DI) water, respectively, for 10 min each. Then, the samples were allowed to dry in ambient air in a clean environment.

2.3.2 Deposition of CuO over glass substtrate

The hydrothermal process is a chemical-based approach for synthesising nanostructured semiconductors at controlled temperature and pressure in solution. Nowadays, the hydrothermal technique has been as much evolved as it is utilised in niche applications to synthesise good quality semiconductors. Throughout this work, hydrothermal technique has been used to deposit CuO over the substrate.

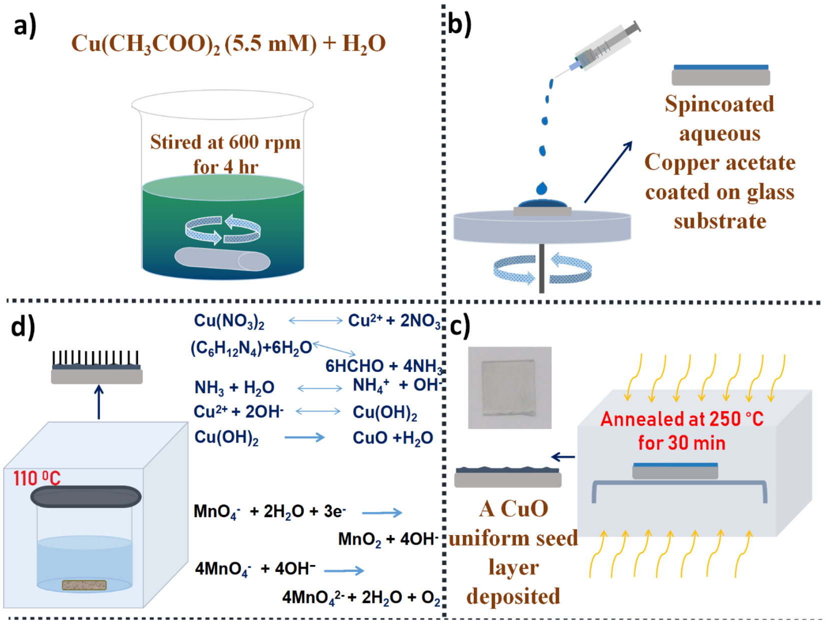

Figure 2.1: Schematic representation of the growth process: a) seed solution preparation technique, b) spin coating of seed solution over the glass substrate, c) annealing of the sample for seed-layer deposition and d) solution-process for nanostructure growth over seed-layer deposited glass substrate and involved chemical reactions.

Deposition of CuO thin-film

For the deposition of CuO thin-film over the glass substrate, a solution of copper acetate ($Cu(CH_3COO)_2$, Sigma-Aldrich, 99% purity) in the DI water of concentration 2 M is prepared by continuously stirring the solution for several hours. The obtained solution was spin-coated over the substrate and annealed in an ambient oven at 200 ° C for 30 min. Figure 2.1 (a-c) represents all the above steps. A black colour organic residue is removed from the top of the sample by washing it in DI water. After drying the sample, a transparent and smooth thin-film of CuO is left over the glass substrate.

Growth of CuO nanostructures

For the growth of CuO nanostructures seed-layer assisted hydrothermal technique has been followed. The thin-film deposited over the glass substrate in the previous step has been used as a seed-layer for the further growth of CuO nanostructures. In the process of the growth of all types of nanostructures, discussed later, the precursor solution composition and growth temperature were the same. Precursor solution was

Growth in pristine solution Seed-layer assisted hydrothermal growth of the CuO nanostructures over the glass substrate was performed in the pristine solution of copper nitrate ($Cu(NO_3)_2$, Sigma-Aldrich, 99% purity) and hexamethylenetetramine ($(CH_2)_6N_4$) in deionised water. The respective concentrations of copper nitrate and hexamethylenetetramine (HMTA, $(CH_2)_6N_4$, Sigma-Aldrich, 99% purity) are

Growth in solution with additive For the growth of CuO nanostructures, the seed layer-assisted hydrothermal growth technique is used. The thin-film deposited using the technique mentioned previously is used as the seed layer for the further growth of nanostructures. For the pristine growth, a precursor solution of copper nitrate and hexamethylenetetramine. To tune the growth of CuO nanostructures, different concentrations of $KMNO_4$ were used as an additive while the precursor solution remains the same as mentioned above. Different morphologies of CuO nanostructures were obtained by varying the $KMnO_4$ concentration from 0.1 mM to 50 mM.

Morphological transition in CuO thin-film

The catalytic activity of Cu^{+2} in dissociation of hydrogen peroxide (H_2O_2) has been used for the morphological transition in CuO thin-film. In this experiment, the CuO thin-film sample synthesised by the same previously mentioned method was used for further synthesis. A few drops of concentrated H_2O_2 was disperssed over the sample uniformaly. Further, the sample was allowed to get dry in the ambient oven. These simple steps were followed to achieve the morphological transition in the CuO thin-film.

2.4 Sample characterisation

2.4.1 Field emission scanning electron microscope (FESEM)

FESEM is a non-destructive instrumentation tool primarily used to investigate the morphology of the surface at the microscopic level.

2.4.2 X-ray diffraction (XRD) spectroscopy

X-ray diffraction (XRD) is a powerful, reliable, simple and non-destructive technique to determine the crystal structures, lattice constants, orientation of single crystals, defects, stresses and the chemical composition of the material. The wavelength of incident electromagnetic radiation onto the substrate is of only a few angstroms (ranging between 0.7-2 Å), i.e. the order of lattice spacing. In order to analyse a thin film or powder sample, a monochromatic X-ray beam is directed at the sample, and a detector is placed at the opposite angle of incidence. There are different metals like Cu, Co, Mo, Cr, etc., which can be used as a cathode for X-ray generation. In our work, Cu has been used as an X-ray source, as its wavelength is close to the lattice parameters of ZnO, with ease of cooling and availability of standard data. Generally, the X-ray incident angle (2θ) is varied from 10° to 90°, and the diffracted light intensity is measured from a detector to obtain a diffraction intensity plot with respect to different angles of incidence. Diffraction peaks occur only when constructive interference takes place between the reflected X-rays. The condition for constructive interference is given by Bragg's law, defined as:

$$n\lambda = \times 2d\sin(\theta) \tag{2.1}$$

where, n = Order of refraction λ = X-ray wavelength d = spacing between atomic planes θ = Angle between X-ray and scattering planes

The relative intensity of diffraction peaks depends on the type and arrangement of the atoms in the crystals [80]. The peak positions are compared with the standard JCPDS files of the material, and based on the shift in peak position or broadening in the peak, useful information about the crystal lattice is obtained. In this work, a Rigaku D/Max-2000 PC diffractometer was used, using CuKα radiation (λ= 1.54056 Å) at an X-Ray source operating voltage of 40 kV in the 2θ range of 30°– 80° at a scanning rate of 2°/min.

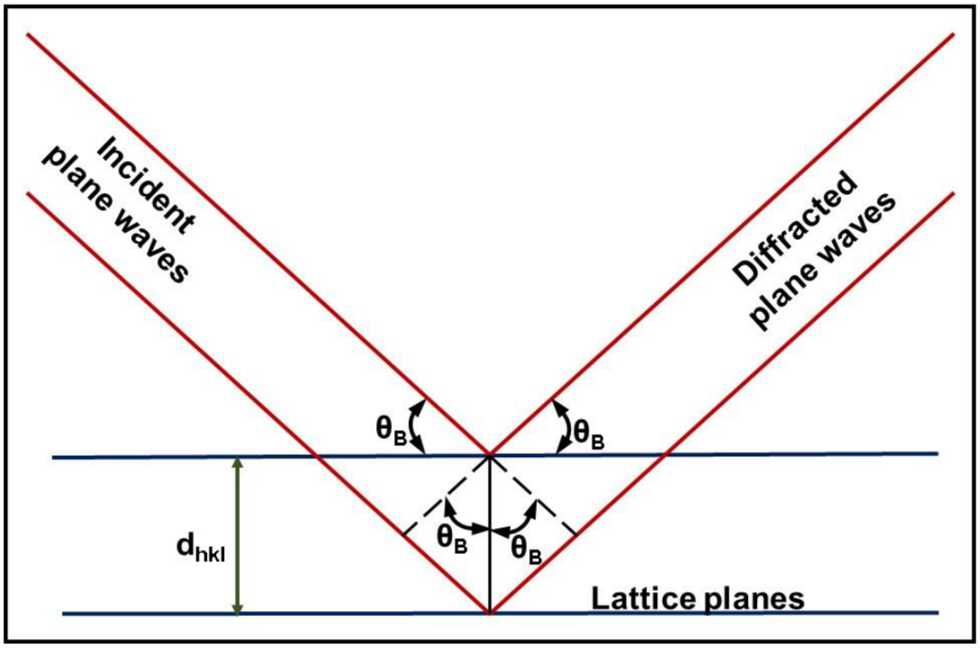

Figure 2.2: Schematic representation of XRD characterisation.

2.4.3 Ultraviolet-visible (UV-vis) absorption spectroscopy

When electromagnetic waves incident on a matter, a variety of phenomena could take place like scattering, reflection, transmission, absorption and fluorescence/ phosphorescence. The incident wave would be absorbed by the matter when the energy of the wave is equal to or greater than the bandgap of the matter. The schematic of the operation of a typical UV-Vis spectrophotometer is shown in Figure 2.5. As the light is incident on the sample, it would transmit through the sample or be absorbed by it. Therefore, the amount of light absorbed by the sample could be calculated as the difference between the incident light intensity (I_o) and the transmitted light intensity (I). Quantitatively, absorbance is described by the equation:

$$A = -\log T = -\log(\frac{I}{I_o})] \tag{2.2}$$

In the above equation, A is absorbance, T is transmittance, I_o and I are the intensity of the incident light and the transmitted light, respectively, at a given wavelength. The absorbance A of a material is a dimensionless quantity. In general, a UV-Vis spectrophotometer consists of a broadband light source such as a tungsten-halogen or deuterium lamp, a dispersion device for the separation of different wavelengths and a detector to convert visible light intensity into an electrical signal. Firstly, the absorption of the bare substrate has been taken as a baseline, which would be subtracted from the sample data to obtain the absorption data of the sample only. The monochromatic light coming from the dispersion device is passed through a beam splitter, which would split the beam and now one beam fall on the sample and another one falls on the reference cell. The light transmitted through the sample and reference cells is detected and recorded by the detectors. Absorption results of thin films are obtained by subtracting the reference spectra from the substrates. Absorption of the materials also depends on the sample thickness, which is given by the Beer-Lambert law:

$$I(\lambda) = I_o X \exp -(\alpha)(\lambda)(d) \tag{2.3}$$

Where I_o is the incident light intensity, α is the absorption coefficient, and d is the thickness of the sample.

All absorption spectra included in this thesis were measured with a Varian Cary 300 UV-Vis spectrophotometer. Optical UV-Visible (UV-Vis) absorption measurements were taken within the wavelength range of 300-800 nm in normal incidence mode from ZnO honeycomb structures, nanorods, thin film and nanocolumns grown over glass substrates. Cleaned glass samples were used as a reference.

Low scattering of incident light by the solid thin film facilitates the calculation of bandgap (Eg) for the absorption data. However, in the case of powder, nanostructures, or colloidal samples, where the scattering phenomenon is more dominant due to a large surface area, the dispersed light is also counted as absorbed light and is not distinguishable from each other. Therefore, to overcome these difficulties in the measurement of absorption spectra, diffuse reflectance spectroscopy (DRS) has been used, which is based on the theory proposed by Kubelka and Munk.

This theory uses diffuse reflectance measurements to estimate the Eg values with good accuracy when the material scatters perfectly diffusely. The diffuse reflectance R is related to the Kubelka–Munk function F(R) by eq. (2.3):

$$F(R) = \frac{(1-R)^2}{2R} \tag{2.4}$$

Where R is the percentage reflectance from the sample. The graph of $[F(R)\times E]^2$ versus energy E in electron-volt is used to measure the bandgap of the material. An attachment to a UV-Vis spectrometer has been used to measure the diffuse reflectance. Here an integrating sphere detector (Fig. 2.6(b)) is attached to Cary 60 (Agilent) UV-Vis instrument (Fig. 2.6(a)).

In Cary 60 white lamp source (xenon lamp) is used and the grating is used to select monochromatic wavelength. Here in this setup, the initial beam split into two parts, one is taken as a reference beam and the second goes on the sample. Finally, the output is compared to the reference beam and data has been collected. Since output photons come through scattering from the samples, so there is an integrating sphere detector.

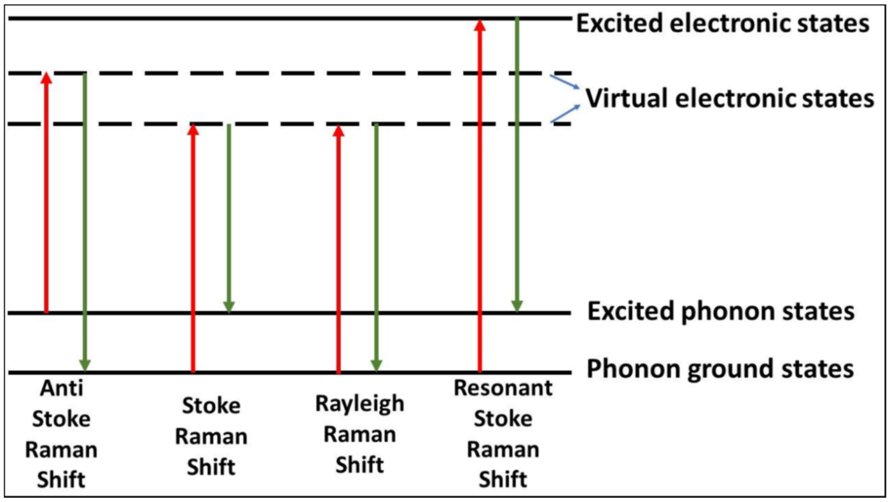

Figure 2.3: Different kinds of scattering phenomena.

2.4.4 Raman spectroscopy

The Raman spectroscopy is used to analyse lattice dynamics, structural properties, chemical composition, orientation, crystalline quality and electronic and magnetic properties of the system. Raman is the inelastic scattering of photons by phonons. As direct phonon-phonon coupling is weak for UV-Vis photons, their interaction occurs mainly through the mediation of electrons. As photons interact with the material, an electron-hole pair is created. The electron-hole pair is then scattered into another state by emitting or absorbing a phonon via electron-phonon interaction. Finally, it recombines radiatively, emitting the scattered photon with lower or higher energy, while leaving the electronic states of the matter unchanged. If the scattered light is of lower frequency, then it is denoted as Stokes Raman scattering, and if the scattered light exhibits a higher frequency, then it is called anti-Stokes Raman scattering.

The experimental set-up of Raman spectroscopy is shown in Fig. 2.4. The scattered light from the sample is collected with the help of a lens. The major challenge here is to filter out the weak inelastic scattered light from the intense Rayleigh scattered light. A notch or bandpass filter is used to filter the useful Raman scattered light and discard Rayleigh scattered light [83, 84]. In this work, Raman measurement was carried out on an Horiba, Labram HR Evolution, from 200 cm-1 to 800 cm-1, using a 532 nm line of a diode laser as an excitation source with 75 mW power.

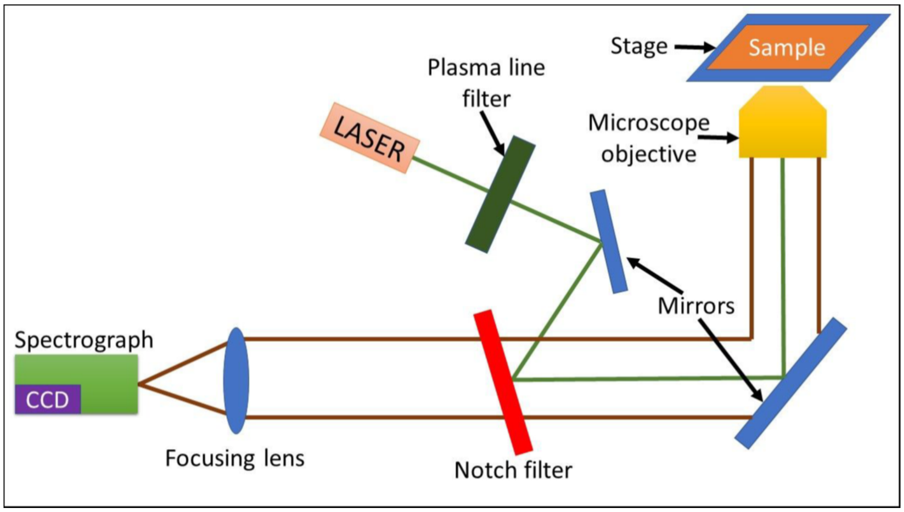

Figure 2.4: Experimental set-up of Raman spectroscopy.

2.5 Device fabrication

2.5.1 Physical vapour deposition (PVD)

: Thermal evaporation is a conventional method for the deposition of metals, metal oxides and small organic molecules on a variety of rigid as well as flexible substrates. The deposition process involves two major steps: evaporation and condensation of the target material. In the first steps, the target material is kept in the boat and is made of high resistance materials like tungsten (W) and molybdenum (Mo). The boat is heated to the melting temperature of the target material for its evaporation (see Figure 2.4). The boat temperature is controlled by changing the input electrical power. The deposition process takes place in the ultra-high vacuum condition (usually 10^{-6} mbar to 10^{-7}

mbar) to avoid interactions between the evaporated material and impurities present in the air. Further, the mean free path of the vapour under the high vacuum conditions is longer than the distance between the boat and the samples. Therefore, the vapour of the target material could travel without colliding with foreign species from the source to the substrate. In the second step of the deposition process, the material vapour condenses and is deposited over the substrate surface. A crystal oscillator monitors the film thickness and deposition rate. One of the major advantages of PVD techniques is that the evaporated material has a gentle impact on the substrate surface; therefore, it is more suitable for soft substrate materials. Two planner Ag electrodes of 50μm x 2 mm x 100 nm (channel length × width × thickness) for the development of planar photodetector were deposited using a PVD system purchased from Hind High Vacuum Private Limited Company, India. The schematic of the thermal evaporation set-up is shown in Figure 2.2. The initial rate of Ag deposition was kept at 0.1 Å/s, which was increased up to 1 Å/s as the thickness reached 10 nm.

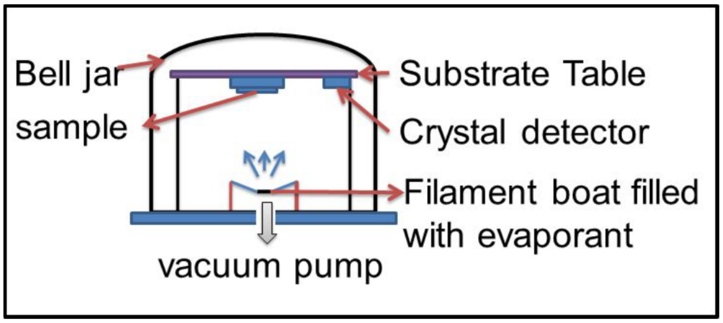

Figure 2.5: Schematic representation of PVD system.

2.6 Device characterisation

During the process of fabrication, the physical parameters like temperature, pressure, humidity and other environmental conditions local to the device under fabrication have an unintended effect on the device's performance. Therefore, post-device fabrication, characterising the device is the next step to investigating the behaviour of the device. For the device characterisation, a voltage swap is applied across the device's terminals, and the corresponding current is recorded.

The plot of the device current (I) vs applied voltage (V), i.e. I-V characteristics, has been predominantly used to investigate the quality of contact formation between the electrode and the semiconductor. Broadly, there are two types of contacts, namely, ohmic and non-ohmic contacts. Ohmic contacts are electrical interfaces between metal and semiconductors distinguished by the linear I-V plot i.e. the current linearly varies with the applied voltage.

$$I = \frac{V}{R} \tag{2.5}$$

here, I is the current, V is the voltage across the terminals, and R is the resistance of the contact. The formation of an ohmic contact can be ensured by ensuring the alignment of energy band levels. The misaligned energy levels of the metal and semiconductor are the reason behind the non-linear behaviour of the contact formed.

In non-ohmic contacts, the current nonlinearly varies with the applied voltage. In certain cases, this kind of contact shows rectification behaviour, i.e., it allows for a unidirectional flow of current. The following is the current equation for the rectifier:

$$J = J_{sT}[\exp\left(\frac{eV_a}{KT}\right) - 1] \tag{2.6}$$

here, J is the current density flowing through the cross-section, J_{sT} is the reverse saturation current density, and V_a is the applied voltage.

The ohmic and rectifying contacts are two ideal cases. However, the practical contacts fall between the two extreme cases of ohmic and rectifying contacts. The I-V characteristic plot tells the quality of contact formation as desired by comparing it with the standard results.

2.6.1 Current-Voltage (I-V) characterisation: Keithley current source

I-V characterisation is a widely used and essential method to measure various device parameters of a photodetector. The photocurrent measurement setup is shown in Figure 2.15. The electrical characteristics of the photodetectors are measured by a Keithley 2612B source meter unit. Current is measured under a swept voltage bias and a constant bias voltage. All the devices are measured under dark first and then measured under the monochromatic light source.

Further, in order to investigate the device photoresponse, IV measurements have been taken, and various device parameters like sensitivity, responsivity, specific detectivity, and external quantum efficiency (EQE) and linear dynamic range (LDR) were calculated, which can be explained as follows:

1. **Dark Current (I_d)**: The current present in the sample, when it is kept in dark conditions, is known as dark current. The variety of defects causes the dark current in the samples when the operating temperature is more than absolute zero, which could produce a large number of charge carriers under dark conditions. It restricts the capability of the device to sense the low-intensity light and reduce the overall device performance.

2. **Photo Current (I_{ph}**: As the samples are shined by the light

of energy more than the bandgap of the material, electron-hole pairs are generated. In the presence of external or built-in electric fields, the charge carriers are swept towards their respective electrodes, leading to a large current flow known as the photocurrent.

3. **Photosensitivity (S)**: It is defined as the ratio of the difference between photocurrent and dark current to the dark current.

$$Sensitivity(S) = \frac{I_{ph} - I_d}{I_d} \tag{2.7}$$

4. **Photoresponsivity (R)**: It is given by the ratio of photocurrent to incident photon power (P_o).

$$Responsivity(R) = \frac{I_{ph} - I_d}{P_o} \tag{2.8}$$

5. **Specific detectivity (D^*)**: It is another critical figure of merits for photodetectors. The device with a larger specific detectivity can detect weak signals, which is comparable to the device's noise.

$$Specificdetectivity = R\sqrt{\frac{A}{2eI_d}} \tag{2.9}$$

   where A is the active area of the device, and e is the electronic charge. The detectivity of a detector is the inverse of the noise equivalent power (NEP). However, specific detectivity (D^*) is normalised detectivity to a 1 Hz bandwidth and a 1 cm^2 area, assuming the noise proportional to rms value to area times the bandwith. Simplistically, specific detectivity is the smallest incident power the detector can sense, equivalent to noise.

6. **External quantum efficiency (EQE)**: To develop a highly sensitive UV photodetector for flexible and wearable electronics over

a flexible substrate, which could operate at low power to lengthen the battery discharge time.

Throughout this work, the Keithley 2612A dual-channel source meter has been used as an I-V characterisation tool. The specifications related to this instrument can be referred to from Keithley's official website. This instrument has been used as a software-based voltage swipe, constant voltage source, constant current source, and

2.6.2 Light source

ISS P110 monochromatic tunable light source (*lembda* from 250 nm – 900 nm) has been utilised for optoelectronic characterisation.

Chapter 3

Bandgap engineering in CuO nanostructures and fabrication of wavelength tuneable photodetectors

This chapter discusses the bandgap engineering of CuO from an indirect bandgap of 1 eV to a direct bandgap of 4 eV just by tuning the morphology of nanostructure and midgap defect states. The absorption in near-infrared (NIR) and visible regions is ordinarily suppressed by controlling the growth parameters. Considering the increasing scope and demand of varying spectral range (UV-C to NIR) photodetectors, the systematic variation of the available density of states (DOS) at a particular energy level in CuO nanostructures has been utilised to fabricate dual-band (250nm and 900 nm), broadband (250 nm–900 nm), and UV-C (250 nm) photodetectors. The sensitivity and detectivity of the photodetector for broadband detectors were 10^3 and 2.24x10^{11} Jones for the wavelengths of 900nm and 122 and 2.74x10^{10} Jones for 250 nm wavelength light, respectively. The UV-C detector showed a sensitivity of 1.8 and a detectivity of $4\text{x}10^9$ Jones for 250 nm wavelength light. A plausible mechanism for photoconduction has been proposed to explain the device operation and the effect of variation in available DOS. The obtained photodetectors are potential candidates for future optoelectronic applications.

3.1 Introduction

In recent years, the research on semiconductor-based photodetectors with UV-C (200 nm–280 nm) [47, 48] wideband [i.e., UV-C to near-infrared (NIR) (up to 1000 nm)] [49,50] and multi-band or dual-band spectra [51] has been given immense importance for a wide range of applications (summarised in Table 3.1) by the scientific community. A common approach for fabricating broadband photodetectors is to form heterojunctions between the high and low-bandgap semiconductors. Recently, high-performance photodetectors based on hetero-junctions of perovskites [52] and 2D materials [53] with other semiconductors, such as ZnO, NiO [54], etc., have been reported. However, these semiconductors have certain associated disadvantages, viz., instability of perovskites in the ambient environment [55] and a dearth of a facile technique for synthesising graphene (other 2D material systems). However, there are a few semiconductors such as ZnO, MoS_2, Bi_2Se_3, and MoO_3, [52, 56–58] which have potential for broadband photodetection and, among these semiconductors, solution-processed metal oxide-based photodetectors have some significant advantages, viz., facile and low-cost synthesis process and stability toward the ambient environment which make them prominent candidates for photodetectors [47, 59].

Generally, metal oxides are intrinsically n-type in nature. Meanwhile, the incorporation of p-type character through doping poses specific challenges such as self-compensation, instability, and reproducibility issues [60, 61]. CuO is one of the few metal oxide p-type semiconductors that have been utilised for optoelectronic applications [62] and reported to have an indirect bandgap (1 eV–1.4 eV) and a direct bandgap (2 eV–4 eV) depending on various process parameters [62]. The range of bandgaps offered by pristine CuO can be utilised to tune the optoelectronic properties, and further, it can be made useful in different optoelectronic applications [63].

Table 3.1: Spectral band wise applications of photodetectors.

PD sensitive spectral band	**UV-C**	**Wideband in UV-C to NIR**	**Multi-band or dual-band**
Applications	Flame detection and terrestrial communication	Machine vision, artificial eyes, telecommunication, and biomedical devices	Imaging technology, environment monitoring, and machine vision

Bandgap engineering is a technique that has been utilised to tune the bandgap of semiconductors to improve the device performance of solar cells, photodetectors, LEDs, gas sensing, biosensing, etc [51, 64, 65, 66]. There are several methods, such as doping, alloying, and morphology modification [50, 66, 67], which have been used to tune the bandgap of a material. However, techniques such as doping and alloying are complex processes, and therefore, morphological variation is a better option for tuning the optical bandgap of CuO.

In this work, a facile technique to deposit CuO thin films over the glass substrate is reported. Seed-layer assisted solution-processed nanostructures were synthesised where $KMnO_4$ is used as an additive in the precursor solution to control the nanostructures' growth and morphology. The choice of $KMnO_4$ as the additive was due to the following reasons:

- it provides an oxygen-rich environment in the precursor solution.
- it is ionic in nature, hence, homogeneous solubility in water compared to other organic additives.
- its versatility as an additive in precursor solution for the growth of numerous nanostructures.

As the bandgap of CuO depends on the condition of the synthesis and surface morphology [66, 68], the concentration of $KMnO_4$ in the precursor solution was optimised to systematically engineer the bandgap of CuO nanostructures from the indirect bandgap of 1 eV to the direct bandgap of 4 eV. The as-synthesized CuO nanostructure with higher available density of states (DOS) at energy levels corresponding to the NIR light source was used to fabricate dual-band photodetectors with a sensitivity and detectivity of 10^3 and 2.24x10^{11} Jones for the light with wavelength of 900 nm and 122 and 2.74x10^{10} Jones corresponding to a wavelength of 250 nm, respectively. As the DOS corresponding to NIR light was relatively suppressed, the respective photodetector shows broadband photodetection with sensitivity and detectivity of 1 and 2x10^9 Jones for UV-C light. A UV-C photodetector was fabricated to further suppress DOS available at energy levels corresponding to NIR light with a sensitivity of 1.8 and a detectivity of 4x10^9 Jones. The as-fabricated devices have shown immense potential for fabricating a large class of photodetectors and understanding the physical aspect of bandgap engineering in CuO.

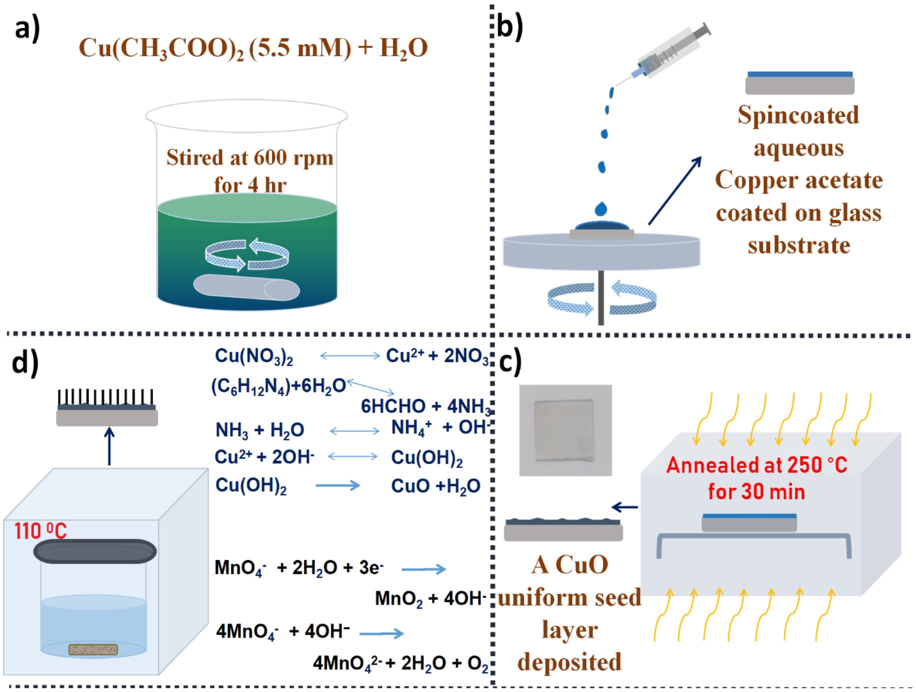

Figure 3.1: Schematic representation of steps involved in Cuo nanostructures growth.

3.2 Experimental details

The boro-silicate glass samples were cleaned by ultra-sonicating the samples in acetone, isopropanol, and deionised (DI) water, respectively, for 10 minutes each. Seed solution of 2 M concentration was prepared by 4 hours of continuous stirring of copper acetate ($Cu(CH_3COO)_2$) in DI water as shown in Fig. 3.1 (a). A spin coating technique was used to deposit seed solution over the glass substrate and annealed at 250 ℃ for 30 min in the oven (Fig. 3.1 (b)). The samples were cleaned with DI water. CuO nanostructures were grown via solution-process technique where the nutrition solution comprised of copper nitrate ($Cu(NO_3)_2$) and hexamethylenetetramine ($(CH_2)_6N_4$). A total of 12 samples were prepared, which included the samples directly grown over the glass substrate, grown over seed layer coated substrate, and the samples with varied concentrations of potassium permanganate ($KMnO_4$) ranging from 0.2 mM to 50 mM. Three sets of synthesised CuO nanostructures samples corresponding to 0.2 mM, 25 mM, and 50 mM KMnO$_4$ concentrations were used to fabricate photo-detectors by depositing 150 nm thick Cu electrodes (of 50 µm channel length) via physical vapour deposition technique at 1 Ås^{-1} rate using shadow mask. The morphology of CuO nanostructures was investigated using field emission scanning electron microscopy (FESEM), Zeiss Supra-55. Crystallinity was analysed using X-ray diffraction (XRD) having Cu-Kα radiation source of wavelength 1.54 Å. UV–vis absorption spectra were obtained (Cary 60 UV–vis, Agilent Technologies) with a range of wavelengths from 200 nm to 800 nm. Raman spectroscopy was done using Horiba, Labram HR Evolution, from 200 to 800 cm^{-1}. Electrical characterisation was performed using a Keithley 2612A dual-channel channel source meter. Photoconductivity measurements were carried out using ISS P110 monochromatic tunable light source (λ from 250 nm - 900 nm) at the intensity of 2.11 mWcm^{-2}.

3.3 Results and discussion

3.3.1 Morphology and basic characterisations

The experimental details to synthesise the CuO nanostructures and possible chemical reactions involved in CuO formation are given above (Fig. 3.1). The field emission scanning electron microscope (FESEM) image in Fig. 3.2(a) shows the shuttle-like structures with the size of 2 μm, grown in pristine nutrient solution over the glass substrate (without the incorporation of seed-layer). The nanostructures were nonuniform, scattered, and poorly adhered to the substrate. Therefore, seed-layer mediated growth has been performed, which has led to the formation of nanorods with a cross-section of 50nm [Fig.3.2(b)]. Furthermore, by adding various concentrations of KMnO$_4$, viz., 0.2, 2, 5, 10, 25, and 50

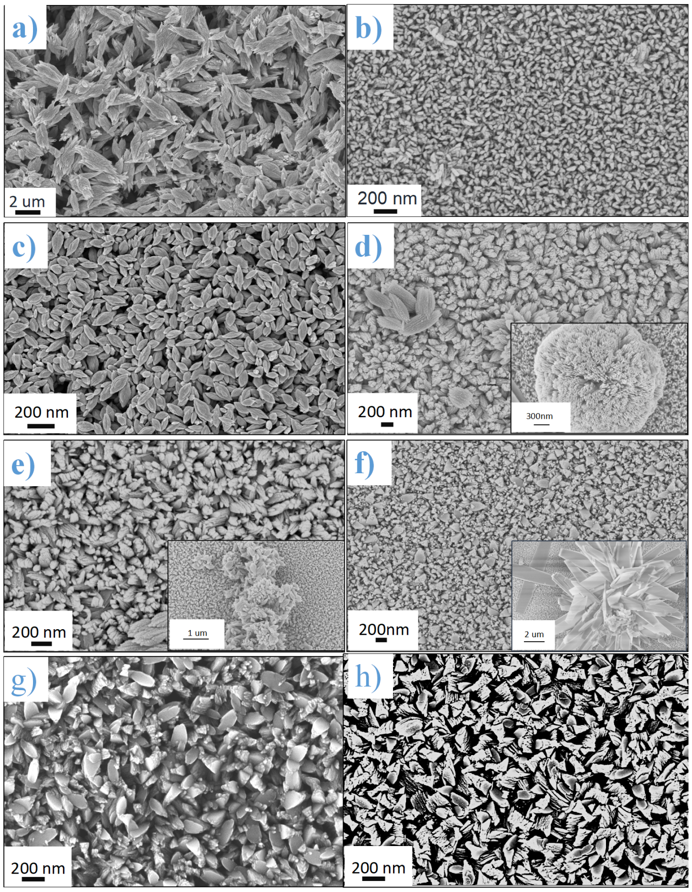

Figure 3.2: FESEM images of as-synthesized nanostructures a) without seed-layer, b) with seed-layer mediated pristine growth and c-h) with KMnO4 concentration of 0.2, 2, 5, 10, 25 and 50 mM, respectively..

mM in the nutrient solution, the growth of nanostructures was modulated, and the obtained morphologies are shown in Figs. S2(c)–S2(h), respectively. At a $KMnO_4$ concentration of 0.2 mM, nano-petals-like structures were formed [Fig. 3.2(c)]. Furthermore, a gradual increase in the $KMnO_4$ concentration (2 and 5 mM) has resulted in the formation of nano-bundle-like structures [Figs. 3.2(d) and 3.2(e)]. Moreover, at a $KMnO_4$ concentration of 10 mM, there is a mixture of nano-bundles and nano-semiparaboloid-like structures, whereas, for concentrations of 25 mM and 50 mM, nano-semi paraboloids are dominant structures.

At $KMnO_4$ concentrations below 10 mM, the growth of nanostructures took place through oriented attachment and was followed by the

Ostwald ripening process [62]. At 10 mM and higher concentrations of $KMnO_4$, the oriented attachment process starts to dominate, which results in an oval cross-section resembling the monoclinic lattice structure of CuO [62].

The phase purity of the as-synthesized CuO was confirmed by XRD analysis [Fig. 3.3(a)]. The peaks at 32.5°, 35.54°, and 38.49° correspond to planes [110], [-111], and [111] of CuO and are well-matched well-matched with the standard JCPDS card no. 72–0629 of CuO [68]. The Raman spectrum is shown in Fig. 3.3(b). The optical vibrational Raman active modes present in CuO are at 290 cm^{-1} (A_g), 340 cm^{-1} (B_{1g}), and 620 cm^{-1} (B_{2g}) [61]. The shifts in all three peaks can be attributed to the variation in the nanostructure morphology [63]. As these nanostructures were grown in the presence of $KMnO_4$, there is the possibility of Mn doping in the CuO lattice. However, the absence of the Raman peak other than the peaks corresponding to the pure CuO phase confirms that there was no doping in the CuO lattice.

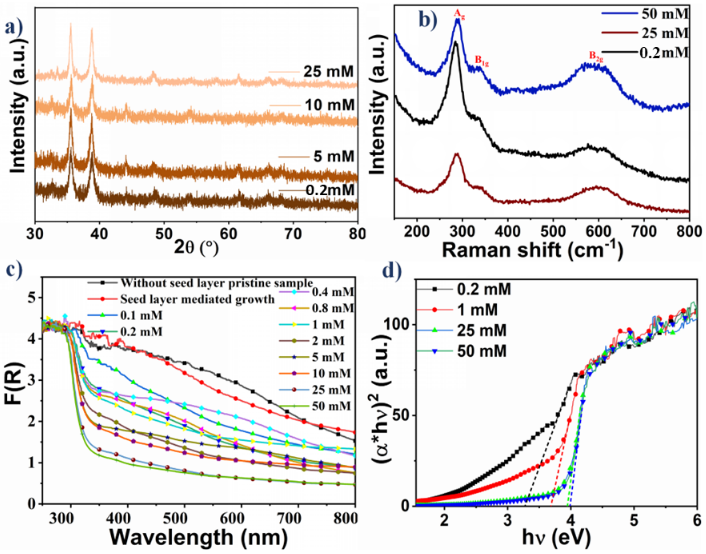

Figure 3.3: (a) XRD spectra, (b) Raman spectra, (c) absorbance spectra, and (d) Tauc-plot.

The absorption spectra [Fig. 3.3(a)] shows a systematic blueshift in the absorption edge for CuO nanostructures, with the increase in the concentration of $KMnO_4$. The indirect bandgap of the nanostructures corresponding to the lower $KMnO_4$ concentration was estimated to be 1 eV, and indirect transitions were found to be dominant in comparison with direct transitions. The direct bandgap was calculated using the Tauc plot [Fig. 3.3(d)]. As the concentration of $KMnO_4$ increased from 0.2 to 50 mM, the direct bandgap was enhanced from 3.27 to 4 eV. Such a significant variation in the optical properties can be attributed to the variation in morphology of nanostructures [66, 68-70], quantum confinement effect, and suppression of defect states [71]. The defect states act as the midgap or intragap states, which are located near the conduction band edge and lead to the decreased bandgap [71]. Defect states' suppression is subjected to the growth condition and can be attributed to the increased oxidative environment provided by $KMnO_4$ during the growth, and suppression of these midgap states manifests in the increased bandgap [63]. Moreover, blueshift in the absorption edge has suggested the suppression of indirect transitions and enhanced direct transitions.

3.3.2 Devices I-V characterization

Furthermore, to investigate the photoresponse of the device, I–V analysis has been performed in the dark (Fig. 3.4(a) shows the device schematic) and under illuminated conditions at room temperature (T=300K). The non-linear response of the device could be attributed to the mismatch between U_{Cu} (4.7 eV) and U_{CuO} (5.3 eV) [inset of Figs. 3.4(b)-3.4(d)]. The devices corresponding to 0.2, 25, and 50 mM $KMnO_4$ concentrations have shown systematic enhancement in the dark current. At 20 V applied bias, current levels for devices corresponding to 0.2 mM, 25 mM, and 50 mM $KMnO_4$ concentrations were 0.18 nA, 5 nA, and 20 nA, respectively. Enhancement in the dark current may be

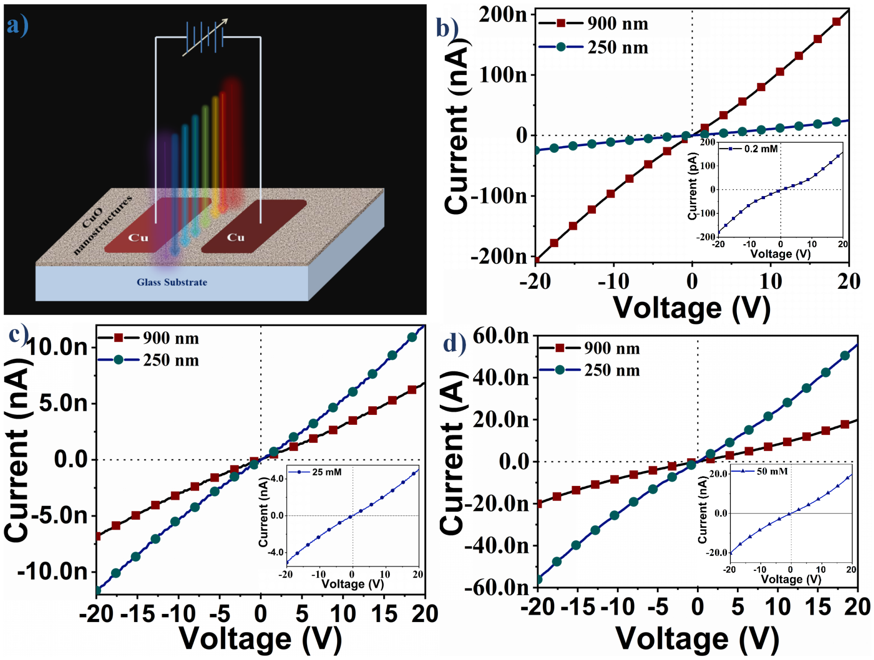

Figure 3.4: (a) Device schematic, IV plot for illuminated conditions for devices corresponding to sample with concentration (b) 0.2 mM, (c) 25 mM, and (d) 50 mM

attributed to the suppression of defect states [72], which are the cause of electron scattering, which in turn reduces the mobility of charge carriers. Figures 3.4(b)-3.4(d) show the photocurrent of the devices corresponding to 0.2 mM, 25 mM, and 50 mM concentrations, respectively, for the light source of 900 nm and 250 nm wavelengths.

All the devices show photodetection with varying spectral sensitivities toward light at wavelengths ranging from 900 nm to 250 nm. Below, a few parameters of the photodetectors are discussed, based on which the performance of the devices was evaluated.

The device corresponds to a $KMnO_4$ concentration of 0.2 mM [Fig. 3.5(a)] has shown a responsivity of 80 mAW^{-1} for the 900 nm light source and for lower wavelengths; it first decreases and then remains constant (4 mAW^{-1} from 800 nm to 300 nm light). For 250 nm light, the device's responsivity was observed to be 10 mAW^{-1}. Sensitivity and detectivity [Figs. 3.5(b) and 3.5(c)] also followed the same

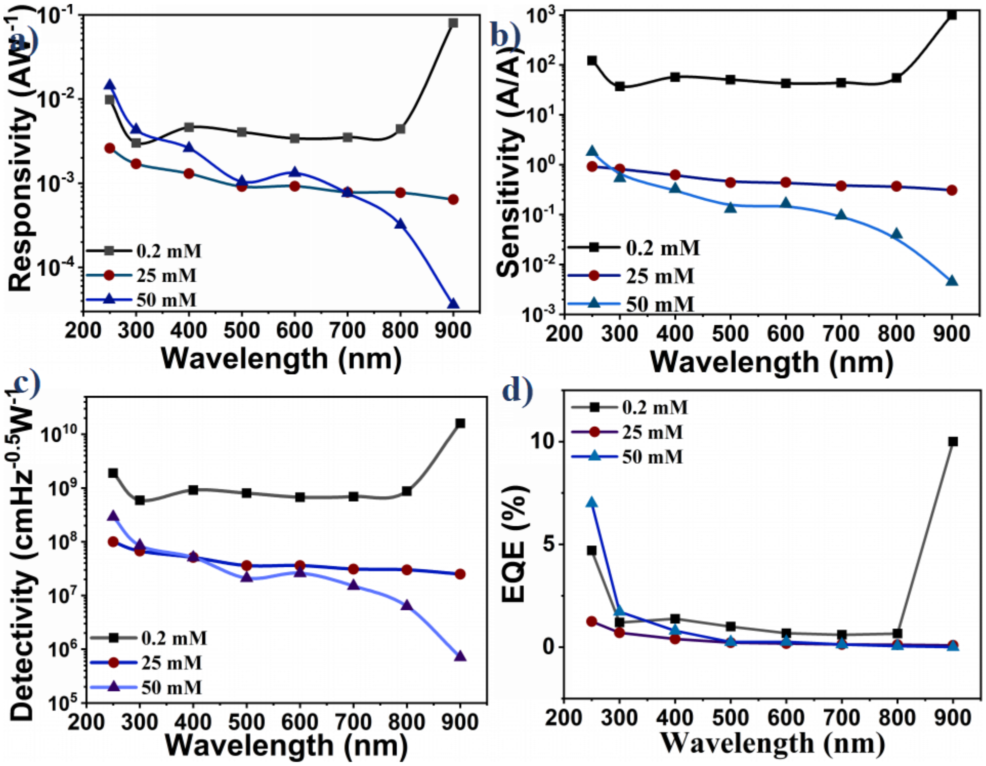

Figure 3.5: (a) Responsivity, (b) sensitivity, (c) detectivity, and (d) EQE plot for the wavelengths from 250 nm to 900 nm at 20 V bias. UV-C to visible and NIR rejection ratio for the devices.

trend. For 900 nm light, the sensitivity and detectivity were 10^3 and 2.24×10^{11} cmHz$^{0.5}$W^{-1}, respectively. Furthermore, these values got reduced for lower wavelengths and remained almost constant (for 500 nm, 50 and 1.1×10^{10} cmHz$^{0.5}$ W^{-1}, respectively) and corresponding to 250 nm light, the sensitivity and detectivity were 122 and 2.74x10^{10} cmHz$^{0.5}$W^{-1}, respectively. The EQE [Fig. 3.5(d)] of the device at 900 nm was 11%, which was highest among all the devices. For lower wavelength, it decreased and remained constant at 1% until 300 nm and steeply increased to 4.5% for 250 nm light source. This device was more sensitive toward wavelengths of light centred at 900 nm and 250 nm; hence, a dual-band photodetector response characteristic is observed in this device. The device corresponding to a $KMnO_4$ concentration of 25 mM has device parameter values of responsivity, sensitivity, and detectivity highest for a wavelength of 250 nm, which are 2.6 mAW^{-1}, 1.25, and 2×10^9 $cmHz^{0.5}W^{-1}$, respectively, whereas, at a wavelength of 500 nm, they decreased to 1 mAW^{-1}, 0.5, and 7.2×10^8 $cmHz^{0.5}W^{-1}$, respectively. Furthermore, no appreciable change in the EQE was observed for the entire wavelength range from 250 nm to 900 nm. Hence, broadband photodetection is observed with almost flat-band response for this particular device. Similarly, the device fabricated with CuO nanostructures corresponding to the $KMnO_4$ concentration of 50 mM has demonstrated the responsivity of 14.4 mAW^{-1}, the sensitivity of 1.8, and the detectivity of $4x10^9$ $cmHz^{0.5}W^{-1}$ on 250 nm wavelength light illumination. The device performance is drastically reduced for higher wavelengths. EQE of this device is 7.2% for 250 nm incident light and decreases to 0.005% for 900 nm light. Hence, the device could be assigned as a UV-C photodetector. The Fig. 3.6(d) shows the UV-C (250 nm) to visible (500 nm) and NIR (900 nm) rejection ratio of all the devices.

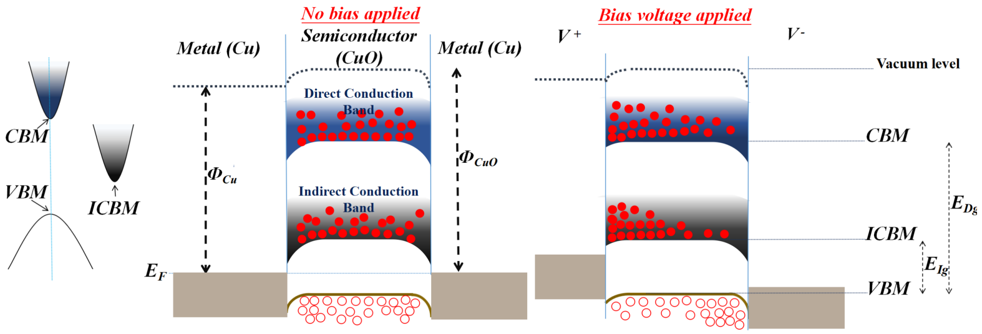

Figure 3.6: Indirect and direct conduction valleys of CuO and band diagram of the Cu/CuO/Cu device. Acronyms and symbols: CBM—conduction band minimum, VBM-valency band maximum, ICBM-indirect conduction band minimum, E_{Ig}-indirect bandgap, and E_{Dg}—direct bandgap.

It is evident from the band diagram (Fig. 3.6) that the transport of photonically generated electrons is facilitated through the indirect conduction band rather than the direct conduction band. Hence, the device corresponding to a $KMnO_4$ concentration of 0.2 mM has a dual-band character displaying more sensitivity toward 900 nm incident light. However, with the increase in the $KMnO_4$ concentration (25 mM and 50 mM), DOS in the indirect conduction band significantly reduced, which led to decreased NIR sensing response.

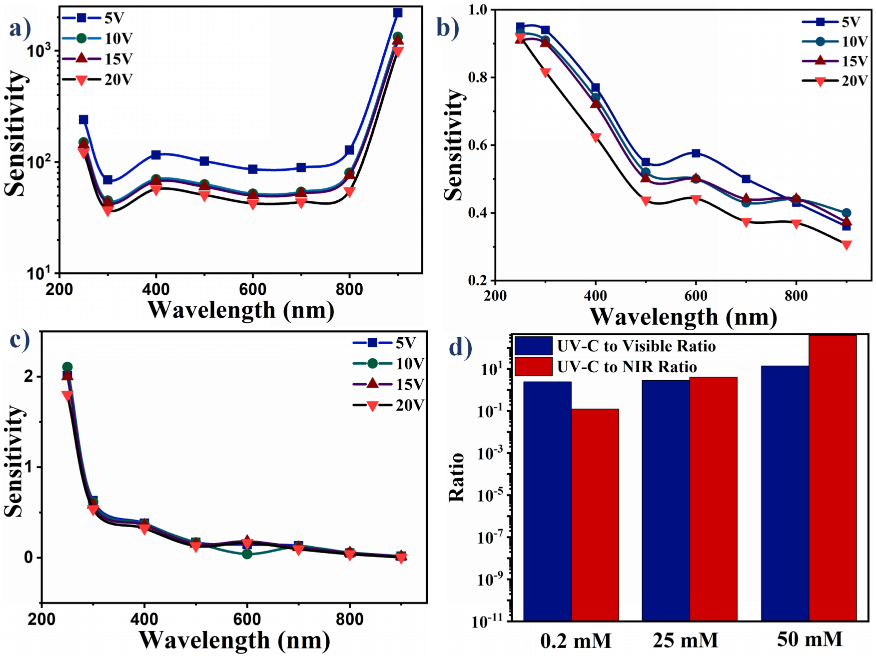

Figure 3.7: Sensitivity plot for the device corresponding to sample (a) 0.2 mM, (b) 25 mM, (c) 50 mM concentrations and (d) UV-C to Visible and UV-C to NIR ratio.

Bias-dependent sensitivity is shown in Figs. 3.7(a)–3.7(c). The sensitivity corresponding to the 0.2mM $KMnO_4$ device was the highest at a bias of 5V and reduced as the voltage was increased. This behaviour can be attributed to the most nonlinear dark current of this device. For the devices corresponding to $KMnO_4$ concentrations of 25 mM and 50 mM, no appreciable change in sensitivity with the change in applied bias has been observed, which could be assigned to the relatively linear behaviour of dark current. Table 3.2 shows the type of device with their corresponding bandgap and wavelength rejection ratio of the devices. Table 3.3 provides a comparison between the previously reported

Table 3.2: Trend of bandgap tuning and rejection ratio.

$KMnO_4$ Concentration (type of photodetector)	**Bandgap (eV)**	**Wavelength rejection ratio of device**
0.2 mM (dual-band)	3.27	2.42 (UV-C to Vis)-20 (NIR to Vis)
25 mM (broad-band)	3.93	2.9 (UV-C to Vis)-4.06 (UV-C to NIR)
50 nM (UV-C)	4.0	13.9 (UV-C to Vis)-400 (UV-C to NIR)

CuO-based photodetectors and the devices reported in this work. The dual-band photodetector reported in this work has demonstrated higher sensitivity compared to other devices. The values of all the parameters for the broadband device are calculated at a 250 nm light source.

3.3.3 Conclusion

In summary, we have demonstrated a facile and cost-effective solution-based technique for CuO nanostructure growth on glass substrates. The variation in the $KMnO_4$ concentration in the nutrient solution is used to tune the morphology and bandgap (from 1 eV to 4 eV) of the CuO nanostructures. The bandgap of pristine CuO has been systematically tuned by varying the $KMnO_4$ concentrations that were utilised to fabricate different classes of photodetectors, such as dual-band (wavelengths of 250 nm and 900 nm), broadband (250 nm–900 nm), and UV-C. This achievement of systematic bandgap engineering may be utilised for many applications. Furthermore, the obtained variety of CuO nanostructures was utilised to fabricate different classes of photodetectors like dual-band (wavelengths 250 nm and 900 nm), broadband (250 nm–900 nm), and UV-C. This work can pave the way for further research in solution-processed Cuo-based wide and varying spectrum photodetectors.

Table 3.3: Comparison between the previously reported CuO-based photodetectors and our photodetectors.

Type of photodetector (excitation wavelength and power)	**Morphology**	**Synthesis method**	**Type of substrate used**	**Responsivity**	**Sensitivity**	**Detectivity (Jones)**	**References**
Visible (404nm and 11.1 mW cm^{-2})	Nanowire	Thermal oxidation	Cu foil	-	4	-	[73]
NIR (808nm and 0.1 mW cm^{-2})	Nanorod	Electrodeposition	Silicon (p-type)	1.6 A W^{-1}	7.2	-	[74]
Visible (633nm and 0.5 W cm^{-2})	Thin film	Sol–gel	SiO$_2$	170 mAW^{-1}	10	6.38×10^{11}	[75]
NIR (808nm and 0.8 W cm^{-2})	Nanowire	Thermal oxidation	SiO$_2$	-	1.3	-	[76]
UV-C solar-blind (254nm and 2.11 mW cm^{-2})	Thin film	Hydrothermal	Glass	7.7 A W^{-1}	8.2	3.08×10^{11}	[23]
Dual-band (250nm and 900nm and 5 mW cm^{-2})	Nano-bundles and nano-semiparaboloids	Hydrothermal	Glass	10 mAW^{-1} and 80 mAW^{-1}	122 and 1000	2.74×10^{10} and 2.24×10^{11}	This work
Broadband (250 nm–900nm and 5 mWcm^{-2})	Nano-semiparaboloids	Hydrothermal	Glass	2.6 mA W^{-1}	1.25	2×10^{9}	This work
UV-C (250nm and 5 mWcm^{-2})	Nano-semiparaboloids	Hydrothermal	Glass	14.4 mA W^{-1}	1.8	4×10^{9}	This work

Chapter 4

CuO thin-film-based UV-C photodetector and PPC effect

4.1 Introduction

Solar-blind photo-detection has many applications like space, satellite communication, military and defence, etc. [78, 79]. In principle, wide band gap semiconductors are required with high rejection for the light with $\lambda > 280$ nm in order to fabricate a solar blind photodetector. In this context, semiconductors like Al-doped GaN, Mg-doped ZnO, and diamond, etc., have been demonstrated for solar blind detection [80, 81]. The Al-doped GaN and Mg-doped ZnO systems suffer from the rapid deterioration of crystallinity and phase segregation, respectively. The diamond has a large indirect band gap (5.5 eV); however, it suffers from low quantum efficiency [82]. Wide-band gap oxide semiconductors are potential contenders for solar-blind photodetectors [83, 84]. Recently, β-Ga_2O_3 has been demonstrated for solar blind photodetection [85]. However, it requires high temperatures and complex processing for growth [84]. Among oxide semiconductors, copper oxides like CuO, Cu_2O, etc., are promising semiconductors for optoelectronic applications. CuO thin films and nanostructures have been used for visible and near-infrared (NIR) photodetection by using their indirect transition (1 eV-1.5 eV) [86-89]. It is important to mention here that CuO has both direct and indirect transitions [90, 91]. The direct transition falls in the UV region and thus can be used for UV detection. Various deposition techniques, such as sputtering, pulsed laser deposition, etc., have been employed to grow CuO thin films/nanostructures, but, in general, these are complex and require high-temperature processing [92, 93]. The most common technique to grow CuO thin films/nanostructures involves annealing of Cu foil at 500 ° C in an oxygen environment [93, 94]. This process is limited to Cu foil or Cu-coated substrates and, therefore, unsuitable for transparent optoelectronic devices.

With the above background and motivation, in this chapter, we will be discussing a very simple and reliable technique to synthesise CuO thin-films using a solution process for the development of solar blind photodetectors and optical memory [95-98].

4.2 Experimental details

CuO thin films were coated using a simple solution process. Firstly, 0.1 M solution of copper acetate monohydrate, i.e. $\mathrm{Cu(CO2CH_3)_2H_2O}$ in de-ionised (DI) water, was stirred for 2 hours in order to get a stable colloid. After that, the solution was spin-coated at a rate of 1500 rpm for 30 s. Finally, the solution-coated glass substrates were annealed at 200 °C for 20 minutes to get uniform CuO thin films. The obtained films were rinsed with ethanol and finally with DI water to remove impurities. The crystal structure was investigated by grazing incidence X-ray diffraction (GIXRD Rigaku Smart Lab® system) at a small incident angle (0.3°). The Raman studies were carried out by HORIBA LabRAM with λ_{ext} of 488 nm. X-ray photoelectron spectroscopy (XPS) was performed by the Axis-Ultra DLD system. Absorbance spectra were recorded by a Perkin Elmer LAMBDA 950 UV-VIS-NIR Spectrophotometer in the 200 to 2500 nm range. CuO thin films based photoconductor was fabricated by depositing 50 nm thick lateral Au electrodes (spacing of 50 μm) using thermal evaporation. Electrical characterisation was performed using a Keithley 2612A dual-channel source meter. Photoconductivity measurements were carried out using ISS P110 monochromatic tunable light source (λ from 250 - 800 nm).

4.3 Results and discussion

4.3.1 Basic characterizations

The FESEM image of the thin film, as shown in Fig. 4.1(a) confirms the uniformity of the film. The thickness of the film was observed to be in the order of 50 nm. The phase purity of the film was confirmed by performing Grazing incidence X-ray diffraction (GIXRD) at an incidence angle of 0.3°. The GIXRD data was compared with standard JCPDS data [91], and all the peaks corresponded to the monoclinic crystal structure of CuO (Fig. 4.1(b)). The Scherrer equation used to calculate the mean crystallite size was given as:

$$D = \frac{k\lambda}{\beta \cos\theta} \tag{4.1}$$

where D is the mean crystallite size, k is the shape factor, λ is the X-ray wavelength, β is line broadening at half the maximum intensity, and θ is the Bragg angle. The calculated average crystallite size was around 10 nm.

Raman spectra of the thin film in Fig. 4.1(c) show three different peaks. All these peaks belong to 3 Raman active modes (Ag+2Bg). The peak at 300 cm^{-1} belongs to A$_g$ and the peak at 323 cm^{-1} and

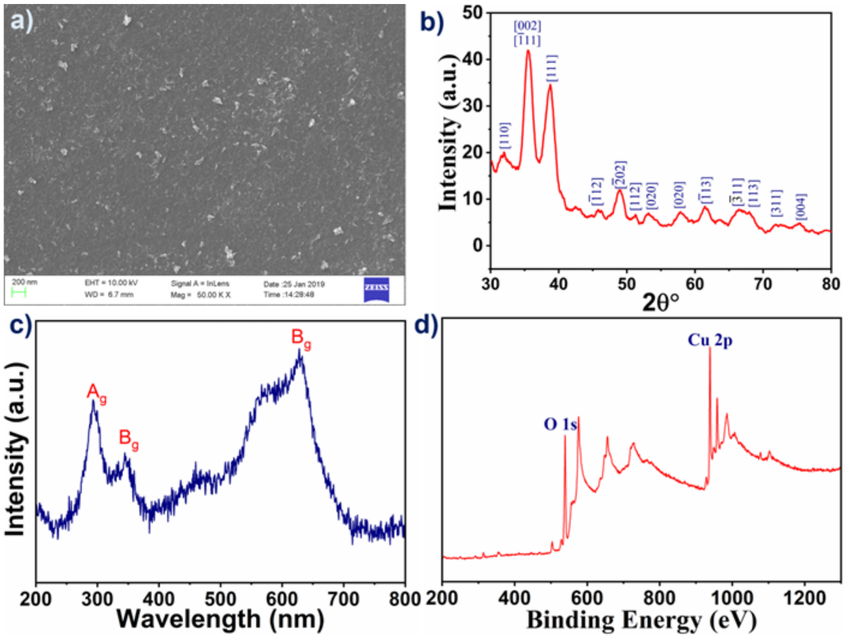

Figure 4.1: a) FESEM image, b) XRD spectra, c) Raman spectra and d) XPS spectra of CuO thin-film.

640 cm^{-1} belongs to B$_g^1$ and B$_g^2$ modes of CuO. XPS analysis of the CuO film was performed to further investigate the phase purity of the sample. Fig. 4.1(d). shows the XPS survey scan and all the peaks well matched with the pure CuO [96].

To investigate the optical property of the as-synthesised CuO film UV-Vis spectroscopy was performed (Fig. 4.2(a)). The CuO thin films were observed to be highly transparent, with a transmittance of more than 90 % in the visible region. The absorption edge was found to be near 300 nm, and the film was highly transparent in the visible region. Fig. 4.2(b) shows the Tauc plot, with the bandgap of the as-synthesised CuO film at 3.67 eV. The as-synthesised CuO thin-film could find novel applications in transparent photovoltaic windows.

4.3.2 Device I-V characterisation

A planner device with a top electrode configuration was fabricated (the device schematic is shown in Fig. 4.3(a)) as specified in the experimen-

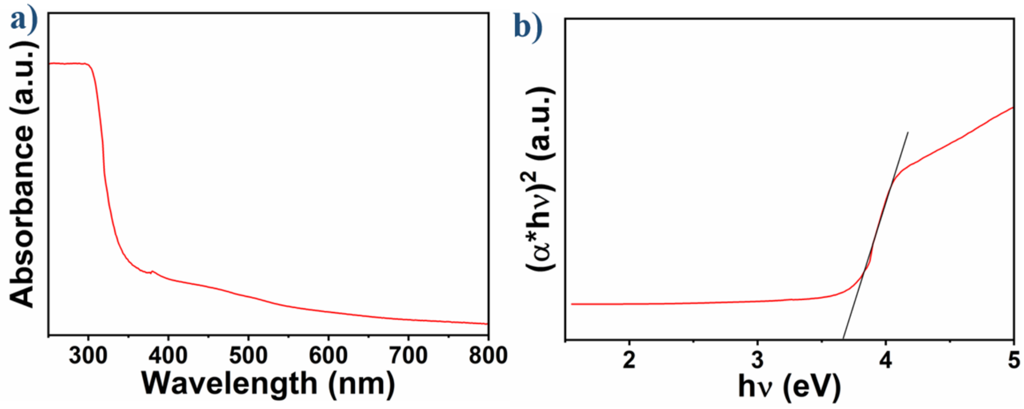

Figure 4.2: a) Absorption spectra, and b) Tauc Plot.

tal section. The I-V characterisation of the device in dark conditions has been shown in Fig. 4.3(b). At 20 V applied bias, the dark current value was 1 μA.

The dark current curve was linear in nature, which indicated the formation of ohmic contact between the CuO ($\phi_{CuO} = 5.3$ eV) and Au ($\phi_{Au} = 5.1$ eV) electrodes. To perform optical characterisation, the device was illuminated with a light source of wavelengths ranging from 254 nm to 800 nm. It was observed that an as-synthesised CuO thin-film-based device is almost insensitive towards a wavelength of more than 290 nm. In convergence with the absorbance data, the device has shown solar-blind behaviour, which can be utilised for many other opto-electronic applications, viz., flame detection, missile tracking systems, etc. Upon exposing the device with a 254 nm light source (incident power of 5 mWcm^{-2}), the photo-current saturates to the value of 4.05 μA. As the light was switched off, rather than instantaneous suppression, there was a very gradual decrease in photo-current (Fig. 3(c)). The residual photocurrent persists for 90 h (3.75 days), and it takes even more time to suppress completely, which could be attributed to the formation of a metastable state. The photo-responsivity value for the present device was calculated to be 7.77 AW^{-1}. In addition to this, the photo-detectivity value was calculated to be nearly 3.08×10^{11} cmHz$^{1/2}$W^{-1}. The device has shown large responsivity in the deep UV region and large R$_{UV}$ (photo-responsivity in UV region) to R$_{Vis}$.(photo-responsivity in the visible region) ratio (5430) with a unique feature of solar blind detection.

In the dark state, I-V characteristics were found to be linear in nature, even at low voltage ranges (-0.5 to 0.5 V). It indicated that Au forms ohmic contacts with CuO and is in good agreement with the reported literature. Moreover, Kelvin probe force microscopy (KPFM) measurements were performed on CuO thin-films and the work function of CuO was nearly ϕ_{CuO}=5.3 eV, which is close to the work function of Au (ϕ_{Au}=5.1 eV); therefore, it is certain that CuO is making ohmic contacts with Au [28].

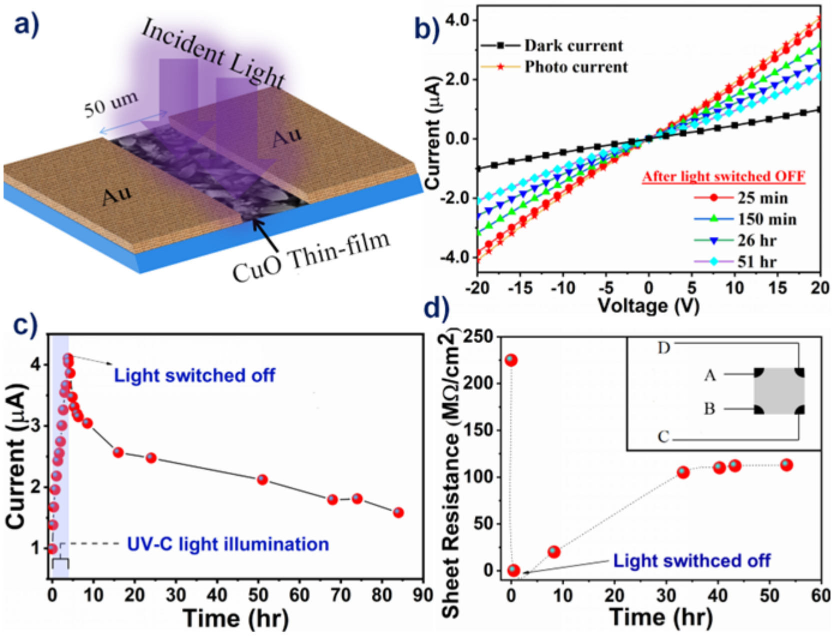

Figure 4.3: (a) Device schematic, (b) I-V characteristic of the device in dark, illuminated and after switching off the 254 nm light source, (c) current value with respect to time at a fixed bias of 20 V and (d) sheet resistance variation with respect to time and inset shows a schematic representation of the arrangement for resistivity measurement..

Figure 4.3(c) shows a clear view of device characteristics i.e. current values at -20 V for different time intervals. It can be seen that the device has been showing PPC for several days (measured up to 5 days). We did not measure the I-V characteristics after 5 days, but expect the values to remain saturated for longer days by extrapolation of the graph [19]. The decay curve for the off-current, I(t), can be fitted with the well-known Kohlrausch's law [32].

$$I(t) = I_1 exp(\frac{-t}{\tau_1})^{\beta} + I_2 exp(\frac{-t}{\tau_2})^{\beta} + I_3 exp(\frac{-t}{\tau_3})^{\beta} \tag{4.2}$$

τ_1, τ_2 and τ_3 are three decay times for the charge carriers. Although the decay time cannot be given exact values, however, it can be seen that the decay time is several orders of magnitude higher than the carrier lifetime. β is the deviation from a single-exponential decay, and it can take values from 0 to 1. Acceptor vacancies, like copper vacancies, are the prominent defect sites in CuO, which can capture holes and cause persistent photoconductivity [99, 100].

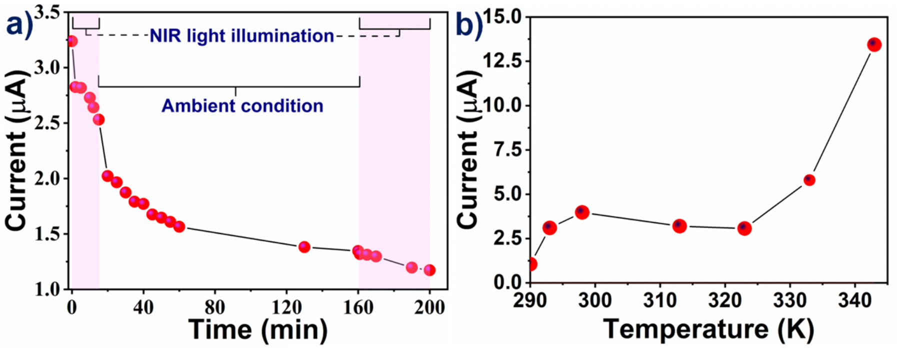

Figure 4.4: Value of current (VB = 20 V) with respect to (a) time during the optical reset process by NIR (800 nm) light source and (b) temperature.

The observed persistent photoconductivity was further investigated by measuring the sheet resistance of the CuO thin film by using the van der Pauw method [101]. Four contact points A, B, C and D were made at the four corners of the square CuO thin film sample (1.5 cm×1.5 cm) (inset of Fig. 3(d)). After illuminating the sample with 254 nm wavelength light, the sheet resistance of CuO thin film decreases by 2 orders (Fig. 4.3(d)). As the light is switched off again, the semiconductor does not attain its original sheet resistance value till the measurement is last performed (54 h).

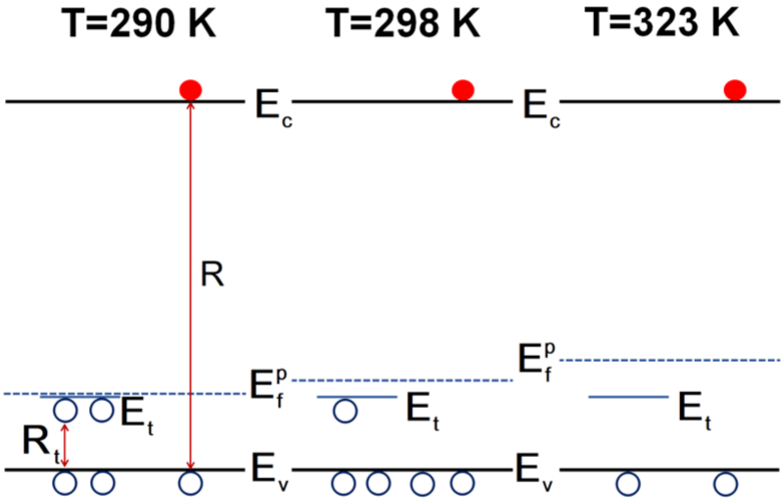

Figure 4.5: Band diagram of CuO showing the shift in quasi-Fermi level with respect to temperature.

In order to make use of the PPC phenomenon, both the Set and Reset mechanisms are required. As we have already discussed, the device was 'Set' by inducing the metastable state in the CuO thin film via UV-C illumination. Now, to make this effect usable, a 'reset' mechanism has been established. The device was reset to its high-resistivity state by thermal annealing. After annealing the device at 50 °C for 10 minutes, the PPC effect was observed to be completely suppressed, and the device recovered to its original conduction state.

Another possible way to optically reset the device is to illuminate the sample with NIR light. Therefore, in order to reset the device, which was already in a set condition, it was illuminated with an 800 nm light source. As shown in Fig. 4.4(a), after the NIR light is switched on, the photocurrent starts to decrease rapidly. Interestingly, the current continues to decrease even after the NIR light is switched off, which suggests that NIR illumination has triggered the reset mechanism, which was responsible for the continuous decrease in the photo-current. In comparison to the PPC retention time of more than 90 hours, it took only 200 minutes to reset the device using this method. This optical reset mechanism achieved in transparent CuO thin film can be further utilised in optically defined transparent electronics applications.

The optical reset mechanism was performed at room temperature, which indicates that PPC in CuO is due to random local potential fluctuations induced by defect states [102], which indicates that there are defect states present in the as-synthesised CuO. Additionally, changing the semiconductor's conductivity by light illumination and getting back to its pristine conduction state by thermal annealing is clear evidence that there is a presence of trap levels or sub-band levels that hold the charge carriers, and this process contributes to the conduction mechanism [103].

Notably, Bhatnagar et al. have probed the trap levels by the measurement of thermally stimulated currents (TSC) [103]. To probe trap states in the CuO thin-film, temperature-dependent I-V characterisation of the device was performed in the pristine state with no prior optical excitation (Fig. 4.4(b)). A bias voltage (V_B) of 20 V was applied across the electrodes, and the temperature was varied from 290 K to 343 K. With the increase in temperature, the current first increases from 1 μA at 290 K to 4 μA at 298 K. As the temperature increased above 298 K, the current started to decrease, and beyond 323 K, it again started to increase.

This behaviour of current variation in pristine CuO can be explained by assuming that the charge carriers are already in a trap state without any external stimulus. As shown in Fig. 4.5, at temperature T=290 K, the quasi-Fermi level of holes (${E^p}_f$) is very near and just above the trap state (E_t). Therefore, the trapped charge carriers would be in thermal equilibrium with the valence band. Consequently, the rate of hole transfer (R_t) from E_t to the valence band is higher as compared to the rate of charge carrier recombination (R). As the temperature increases, the quasi-Fermi level $E^p{}_f$ gradually shifts towards the mid of the bandgap. The peak current of 4 mua was observed at T=298 K, which was assigned to the maximum hole concentration in the valence band. Beyond this temperature, R overtakes R_t, and the concentration of holes in the valence band starts to decrease; hence, the current also decreases. Further, as the temperature is increased beyond 323 K, the thermal generation of the rate of electron and hole pairs exceeds R, and hence, the conductivity is enhanced with the temperature.

From the above discussion, it is inferred that CuO has trap levels which are active at room temperature, and these trap states are capable of holding the charge carrier for a long duration. Hence, as this device is illuminated with the light source of photon energy more than the bandgap, i.e. 3.67 eV, the charge carriers will be trapped, which results in a decreased rate of recombination, due to which carrier lifetime is also increased. Therefore, photoconductivity persists for a very long time.

Transmittance analysis of the pristine and illuminated sample of CuO thin film was also performed to investigate the effect of UV-C exposure on the optical property of the sample (as discussed in our previous work [10]). It was observed that after UV-C illumination, CuO thin film transmittance is decreased in the range of 400 nm to 300 nm, which suggests that there is the formation of defect states near the conduction band edge. These defect states, which were created after the illumination of the sample, could also behave as trap states apart from the already present trap states. This will be probed in our future work.

The technique to set and reset the CuO thin films at different resistivity levels using deep UV illumination and thermal annealing can open wide applications like optoelectronic devices, memory, holographic storage and energy conversion.

4.4 Conclusion

Highly transparent CuO thin films were synthesised using a simple and cost-effective solution process technique. For the first time, CuO thin films were used for solar blind photodetection with the photo-responsivity value of 7.77 AW^{-1} and photo-detectivity of $3.08 \text{x} 10^{11}$ $\text{cmHz}^{1/2}\text{W}^{-1}$. A very large PPC was observed, which lasted for more than 90 hours. Two reset mechanisms were demonstrated, viz., thermal annealing and NIR light illumination. NIR light was able to suppress the PPC effect after 200 minutes of illumination. The trap states which are active at room temperature are responsible for PPC. Set and reset mechanisms can be utilised in future applications like optical memory and making reconfigurable optical contacts between the communicating devices.

Chapter 5

Ultra-widebandgap CuO thin-film nanostructure based improved Solar-blind photodetection

5.1 Introduction

In Chapter 4, a solution-processed low-cost CuO thin-film-based solar-blind PD was discussed. In this chapter, an improved high-performance solar-blind photo-detection using highly transparent CuO nanostructures (with a bandgap of 4.15 eV) has been demonstrated. The device shows the dark current as low as 0.2 nA (-10 V applied bias) and no signature of breakdown even at a bias up to ±175 V. The device has shown record photo-sensitivity of 610, photo-responsivity of 14.02 A/W and photo-detectivity of 3.59x10^{13} cmHz$^{1/2}$W^{-1} in the UV-C region. The ratio of photo-responsivities at 210 nm and 500 nm, i.e., R210/R500, was found to be 5.05x10^{4}. Additionally, the device has shown external quantum efficiency of 5900 % at 210 nm excitation. This letter will establish CuO as one of the most promising ultra-wide bandgap semiconductors for cost-effective solar-blind photo-detection.

5.2 Introduction

Solar-blind photo-detection has enormous potential for applications like flame detection, water purification, missile tracking, non-line of sight and optical communication, bio-medicine, harmful ultraviolet radiation sensing, etc. [104, 105]. The state-of-the-art technology for solar-blind photodetectors is based on ultra-wide bandgap (UWBG) semiconductors, i.e., materials with bandgap considerably higher than GaN (Eg=3.4 eV) [106]. Among them, the potential contenders are Al-doped GaN (6.2 eV $< E_g >$ 3.4 eV), Mg-doped ZnO (E_g 3.6 eV), diamond (E_g = 5.47 eV), and β-Ga_2O_3 (Eg = 4.69 eV) [105, 106]. In the case of doped and/or alloyed materials like AlGaN, MgZnO, etc., the complex growth process and difficulty of getting high-quality semiconductors limit their viability [105]. The other disadvantages are the deterioration of the samples as well as phase segregation with time. Additionally, the bandgap of the diamond can not be easily tuned at room temperature [107]. Moreover, diamond-based detectors also agonise from low external quantum efficiency [106].

Recently, we have demonstrated solar-blind photo-detection in CuO thin films [10]. We have explored direct band transitions in CuO and utilised it for deep UV (DUV) detection. It must be pointed out here that CuO has been traditionally believed to be a material sensitive towards the near-infrared (NIR) spectral region owing to its indirect bandgap nature [108]–[110]. Semiconducting nanostructures (NSs) have several advantages over their corresponding thin films, such as a large surface-to-volume ratio, improved physical and chemical properties, etc. Here, we have optimised the process parameters to get CuO NSs with a bandgap higher than GaN. We demonstrate CuO NSs with a bandgap of 4.15 eV and transparency of >92%, along with excellent solar-blind photo-detection. The research work will establish CuO NSs as a promising candidate for UWBG-based nano/opto-electronic devices.

5.3 Experimental details

Prior to CuO NSs growth, seed layer coating was done using a simple solution-based spin-coating technique, and the details are discussed elsewhere [111]. Afterwards, 0.1 M copper acetate hemi-pentahydrate ($Cu(NO_3)_2.2.5H_2O$) with equimolar hexamethylenetetramine ($(CH_2)_6N_4$, HMTA) was mixed in 40 ml deionised (DI) water for making precursor solution. For the growth of NSs, the CuO seed layer coated samples were kept in the beaker, which was placed in a preheated oven at a temperature of 110 ° C for 30 minutes. Subsequently, the as-grown samples were washed with DI water multiple times and finally dried. For the fabrication of CuO NSs-based photodetector, Au was chosen as an electrode; concisely, 50 nm thick Au electrodes (50 μm (channel length) $\times$ 1 mm (channel width)) were deposited using the thermal evaporation technique. A Keithley 2450 source meter was used for electrical measurements. 150 W Xenon lamp was used as a broadband light source (200-800 nm) for the photo-detection measurements.

5.4 Results and discussion

5.4.1 Morphological investigation and basic characterisation

The morphology of the CuO NSs was characterised using a field emission scanning electron microscope (FESEM), as shown in Fig. 5.1(a).

It was found that the nano-bundles were formed, which appear like a bunch of smaller NSs organised in a specific fashion. The maximum size of the nano-bundles was around 100±5 nm. The inset of Fig. 5.1(a) shows the FESEM image taken at 25 K times magnification to exhibit that the growth is uniform. The Raman spectra of the CuO NSs were recorded by the HORIBA LabRAM system with λ_{ex} of 488 nm, shown in Fig. 5.1(b). The Raman spectra show three major peaks at 275 cm^{-1} (A_{1g} mode), 323 cm^{-1} (B_{1g} mode) and 630 cm^{-1} (B_{2g} mode) [1]. In order to get an idea about the crystallinity, the X-ray diffraction (XRD) measurements were performed (shown in the inset of Fig. 5.1(b)). XRD data has shown the crystalline CuO phase formation with peak positions at 35.6° and 38.8°, which can be assigned to [002] and [111] peaks of CuO, respectively. The results are in good agreement with PDF 48-1548 of CuO [112].

The UV-Vis-NIR absorption spectrum of the sample (Perkin Elmer LAMBDA-950 spectrophotometer) is shown in Fig. 5.1(c). Interestingly, a substantial absorption in the UV-C region was observed, which can be attributed to the dominating direct band transitions [46, 113]. The absorption edge was found to be around 248 nm. Moreover, an extra peak was also observed at 206 nm; its origin is still under investigation. The Tauc plot shows a bandgap of nearly 4.15 eV, which is higher than the previously reported value of 3.87 eV [10]. Most importantly, the bandgap of CuO is highly dependent on the morphology (size and shape) of the nanostructures [46, 90]. The Urbach energy (EU) has been calculated, and the value is nearly 109 meV (the plot is shown in the inset of Fig. 5.1(c)), which is much lower than the previously reported value and suggests high purity of the samples [90]. The oxidation state of Cu (i.e., Cu^{2+}) has been confirmed using XPS studies (Fig. 5.1(d)). The high-resolution spectra show the presence of Cu $2p_{3/2}$ and Cu $2p_{1/2}$ peaks at 937.9 eV and 958.2 eV, respectively

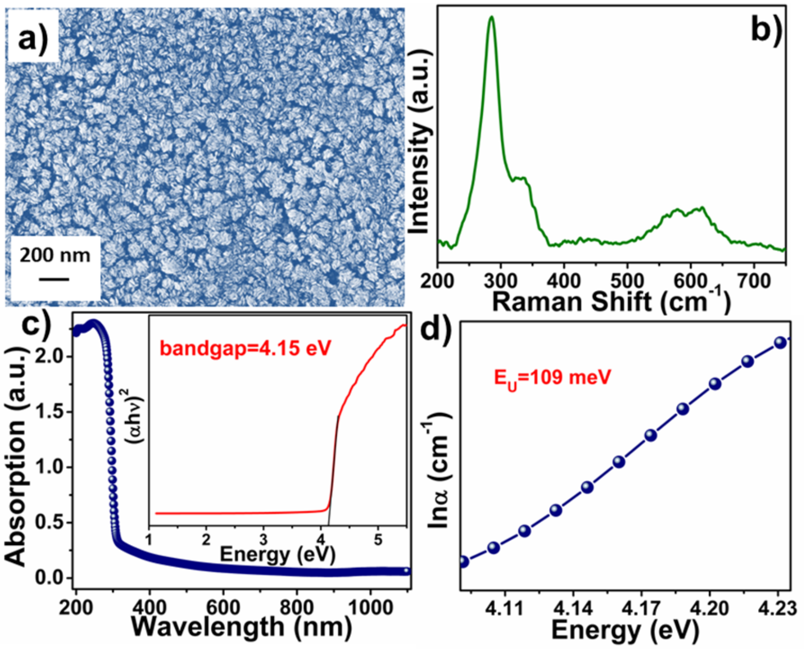

Figure 5.1: (a) FESEM images of CuO NSs at 100 K X magnification; while the inset figure was taken at 25 K X magnification; (b) Raman spectra of CuO NSs is shown in green colour; XRD plot (inset of Fig 1 (b)); (c) Absorption spectra of CuO NSs; Tauc plot (inset of Fig. 1(c)) and linear fit of Urbach tail for CuO samples; (d) Survey spectrum of XPS of CuO NSs; high-resolution spectrum of Cu 2p (inset of Fig. 1(d)).

[114]. The XPS study confirms the formation of CuO.

5.4.2 Device I-V characterisation

A schematic of the CuO NSs-based device is depicted in Fig. 5.2(a). High voltage operation has been performed to check the electrical properties of CuO NSs. The CuO NSs-based planar conductor has shown a dark current of nearly 1.7 nA at ±175 V applied bias without breakdown (shown in Fig. 5.2(b)). This excellent electrical property can be attributed to the large energy bandgap of CuO NSs and the material properties. T. C. Wei et al. have shown similar trends in Ga_2O_3 based photodetector, where the device has been used up to ±200 V without breakdown [115]. The typical Si-based devices have a much lower breakdown voltage range of 50 V. Additionally, the dark current has shown non-linear behaviour, especially for voltages more than ±10 V. This non-linear behaviour is mainly because of the space charge limited currents (SCLC) [116].

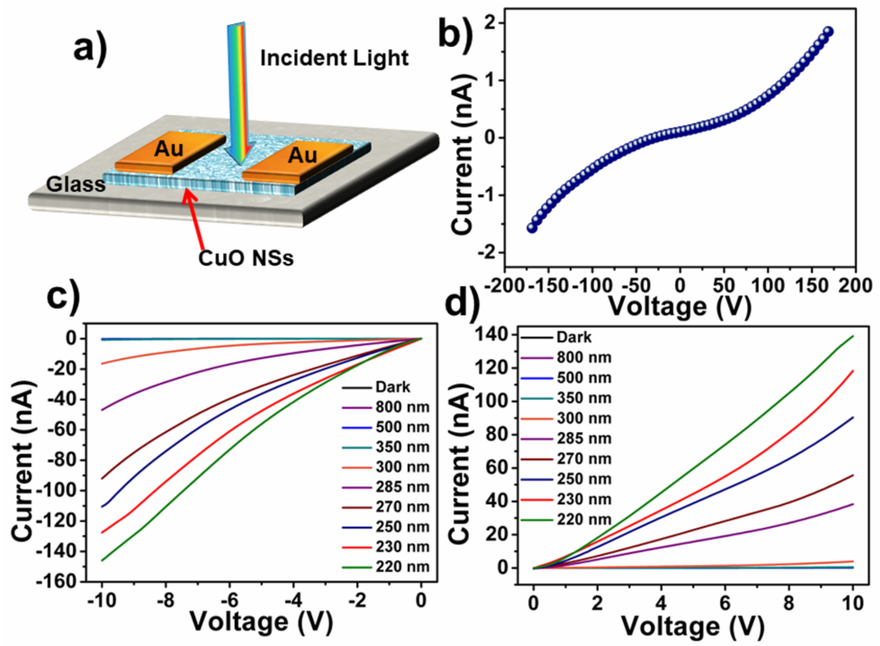

Figure 5.2: (a) FESEM images of CuO NSs at 100 K X magnification; while the inset figure was taken at 25 K X magnification; (b) Raman spectra of CuO NSs is shown in green colour; XRD plot (inset fig 1 (b)); (c) Absorption spectra of CuO NSs; Tauc plot (inset of Fig. 1(c)) and linear fit of Urbach tail for CuO samples; (d) Survey spectrum of XPS of CuO NSs; high-resolution spectrum of Cu 2p (inset of Fig. 1(d)).

For photo-detection measurements, the current (I)-voltage (V) characteristics were performed from 0 V to -10 V applied bias range (Fig. 5.2(c)) and from 0 V to +10 V (Fig. 5.2(d)). The as-fabricated CuO NSs-based device has shown near-linear I-V behaviour with a dark current value of 0.23 nA at ±10 V. The photo-induced effects on the CuO NSs-based device were studied by illuminating the device with a tunable light source. The excitation wavelengths and corresponding intensity values are shown in Fig. 5.2(c, d), which can be used for both figures. The device was found to be blind in NIR, visible, and UV-A regions and has started showing sensitivity to UV-C radiation. We can clearly see a significant enhancement in the photocurrent at 285 nm of excitation. Interestingly, CuO NSs-based photodetector has shown a systematic increment in the photocurrent till 220 nm, with a maximum photocurrent of 150 nA at 220 nm excitation. However, the non-linear behaviour suggests a gain mechanism in Au/CuO/Au planar photoconductors [116-118].

Photo-sensitivity (plot shown in Fig. 5.3(a)) clearly confirms an onset of photo-detection below 300 nm of excitation. The maximum photo-sensitivity was found to be nearly 610 at 220 nm excitation. The as-fabricated photoconductor has shown excellent photo-sensitivity between 210 nm to 250 nm spectral range, which has never been demonstrated in CuO-based devices. Photo-responsivity has been calculated for all the excitation wavelengths and is shown in the inset of Fig. 5.3(a) [119]. A photo-responsivity value of 14.02 AW^{-1} was observed at 210 nm excitation. The ratio of photo-responsivities calculated at 210 nm and 500 nm is found to be 5×10^4. This unique feature of excellent photo-responsivity between 210 nm and 280 nm establishes CuO as a potential candidate for solar-blind detection. Fig. 5.3(b) shows the schematic for the mechanism behind enhanced photo-response in the UV region. The presence of traps and photogenerated carriers will ease the charge transfer and thus increase the device's gain. Moreover, tail states and other defect states like ${V^{2+}}_{Cu}$ will also contribute to the gain mechanism [120]. This will promote internal gain under illumination (shown in the second part of Fig. 5.3(b)).

For better understanding, the variation of photo-responsivity with applied bias has been plotted (Fig. 5.3(c)). There is a linear variation in photo-responsivity with voltage for 270 nm excitation, while a non-linear variation was observed for 220 nm excitation. There are several reasons behind the non-linearity, which are: a) trap-assisted

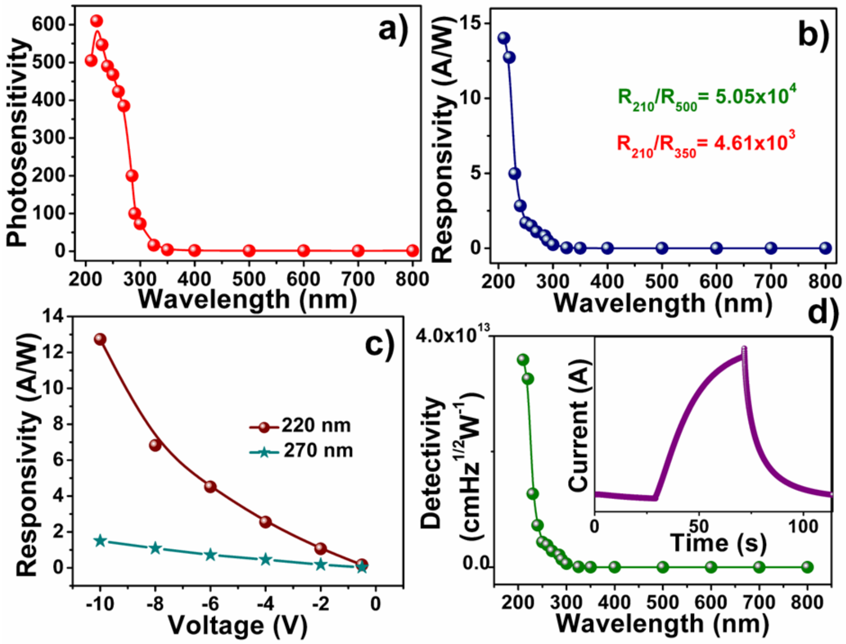

Figure 5.3: Fig. 3. (a) Sensitivity plot as a function of wavelength; the inset shows the photo-responsivity plot; (b) Schematic energy band diagrams of the device (i) in the dark, (ii) under illumination; (c) Bias dependent photo-responsivity plot at 220 nm and 270 nm; (d) Photo-detectivity plot, the inset shows the time-dependent photo-response of the device.

photocurrent generation, b) space charge limited current, c) back-to-back Schottky junction, etc. [116-118, 121, 122]. It must be noted here that there is an Ohmic contact between Au ($\Phi_{Au} = 5.1$ eV) and CuO($\Phi_{CuO} = 5.3$ eV); therefore, the possibility of Schottky junction can be discarded [116]. Planar photoconductors are generally not expected to exhibit an internal gain. The gain at 220 nm excitation can cause the generation of a large number of charge carriers with higher energy radiation, thereby causing SCLC. Additionally, non-linear behaviour can also be assigned to trap-assisted transport, which is also evident in the Urbach energy plot. Along with copper vacancies, tail states can also be a root of non-linear transport [120, 123].

We have calculated photo-detectivity for all the excitation wavelengths (Fig. 5.3(d)). The plot shows a photo-detectivity of 3.59×10^{13}

cmHz$^{1/2}$W^{-1} at 210 nm excitation, comparable to state-of-the-art solar-blind photodetectors. Linear dynamic range (LDR) is defined as the range of current as a function of illumination power over which the device response is linear. Typically, LDR is defined as: (LDR = 20log I_{ph}/ I_d), where I_d is the current in the dark state, and Iph is the photocurrent, calculated at 1 mW/cm^2 incident light intensity [119]. The value of LDR was found to be nearly 61 dB. Finally, the external quantum efficiency (EQE) of the photodetector was calculated. Nearly 5900% EQE was found at λ_{ex} of 210 nm, which sets CuO as a potential semiconductor for solar-blind detection. The device mentioned with the above parameters is compared with previously reported solar-blind detectors using AlGaN, Ga_2O_3, doped Ga_2O_3 system, ZnS, and $Zn_3Ta_2O_5$ (shown in Table I) [124, 115, 125-130]. The inset of Fig. 5.3(d) shows the time-dependent photo-response with an applied bias of -10 V and λ_{ex} = 220 nm, where the rise time was 31 s and decay time was found to be 23 s.

5.5 Conclusion

A new candidate, i.e., CuO, has been added in the category of ultra-wide bandgap semiconductors, with excellent structural, optical, and electrical properties. Highly transparent CuO nanostructures were employed for the fabrication of solar-blind photo-detection with excellent device performance in terms of high sensitivity (610), responsivity (14.02 A/W), detectivity (3.59×10^{13} cmHz$^{1/2}$W^{-1}), LDR (61 dB), and EQE (5900%). The work can pave the path for the development of low-cost solar-blind detectors.

Table 5.1: Comparison of Important Device Characteristics of Recent Literature Based on Solarblind-Detector With Our Device.

Material	**Dark Current and S**	**Spectral range (nm)**	**R(AW^{-1}) and D* (Jones)**	**LDR (dB) and EQE(%**	**R$_{DUV}$/R$_{350}$**	**References**
AlGaN	0.535 nA	250-290	0.15	-	5×10^3	[27]
Ga_2O_3	0.1 nA and 14	185-285	0.32×10^{-3} and 2.8×10^{10}	-	-	[18]
$Zn_3Ta_2O_5$	2.5 μA	Upto 380	0.052 and 9.88×10^{14}	-	-	[28]
Ga_2O_3	10 nA	250-290	0.292	1.34	-	[29]
Al-doped Ga_2O_3	0.96 pA	200-290	1.38	708 %	10^3	[5]
Grahene-β-Ga_2O_3	1 μA and 10^3	200-280	39.3 and 5.92×10^{13}	1.9×10^4 %	>100	[30]
ZnS QDs	0.5 nA and 8	254-290	0.0016 and 5.51×10^9	-	-	[31]
Ga_2O_3	$< 10^{-10}$ A	200-290	0.829	444 %	-	[32]
CuO NSs	$<$ 0.23 nA and 610	210-290	14.02 and 3.59×10^{13}	61 and 5.9×10^3	4.6×10^3	This work

Chapter 6

Improving the photodetector performance via MTE technique

Synthesis of semiconductor thin-films is a well-established process. However, obtaining features of nano-size over the thin-film surface is a time-consuming, complex and costly process. Post-synthesis morphological modification in semiconductors can be an extremely useful technique to obtain nanostructures and tune their properties on demand. In this work, a swift, facile, large-area, implementable, economical and environmentally benign post-synthesis method to tune the morphology of CuO nanostructures has been reported. The developed morphological transition engineering (MTE) technique was used to transform the surface of CuO thin-film into honeycomb-like nanostructures. A plausible mechanism based on the catalytic activity of Cu^{2+} ions in the dissociation of H_2O_2 has been proposed for such a morphological transition in CuO. Further, a photodetector fabricated using CuO thin-film has dark current, sensitivity and detectivity of 0.26 μA, 2.5 and 3.4×10^{10} cmHz$^{1/2}$W^{-1}, respectively. Whereas MTE-based photodetector has shown improved dark current, sensitivity and detectivity of 27 nA, 19.4 and 8.45×10^{10} cmHz$^{1/2}$W^{-1}, respectively. This work could lead research towards establishing MTE to obtain desired nanostructures over semiconductor thin-film surfaces.

6.1 Introduction

Since Richard Feynman's famous talk on "There's Plenty of Room at the Bottom," the world has seen unprecedented miniaturisation in semiconductor electronics through nanotechnology to achieve desired functionality and properties for prospective applications [131, 132, 133]. In most cases, the nanostructured semiconductor can have very different properties from those corresponding to the bulk. Moreover, to capitalise upon the improved semiconductor properties, such as optical and electronic properties, offered by nanostructured surfaces, nanofabrication techniques are employed. Notably, nanofabrication is a synthesis process to design, construct, and manipulate materials of minimum feature size at the scale of 1 to 100 nm [134]. Supramolecular chemistry advancements have made it possible to self-assemble molecules into larger, well-defined entities on the nanoscale through non-covalent interactions. These self-assemblies are categorised as bottom-up nanofabrication approaches (Fig. 1 [132]). However, the other way out is the top-down approach. In the top-down approach, selective etching of the semiconductor is done to obtain the desired nanostructures [135, 136]. Furthermore, in the top-down approach of nanofabrication, the nanostructures are synthesised through lithographic techniques or via chemical-based processes. Physical lithographic techniques require heavy capital investment and rely on very complex technologies [132]. Therefore, recently, the research pursued has been heading towards chemical-based routes, which are cost-effective and less complex [132, 137]. The chemical route techniques reported so far are template etching, selective dealloying, anisotropic dissolution, thermal decomposition [132], and morphological transition engineering [137], as shown in Fig. 1.

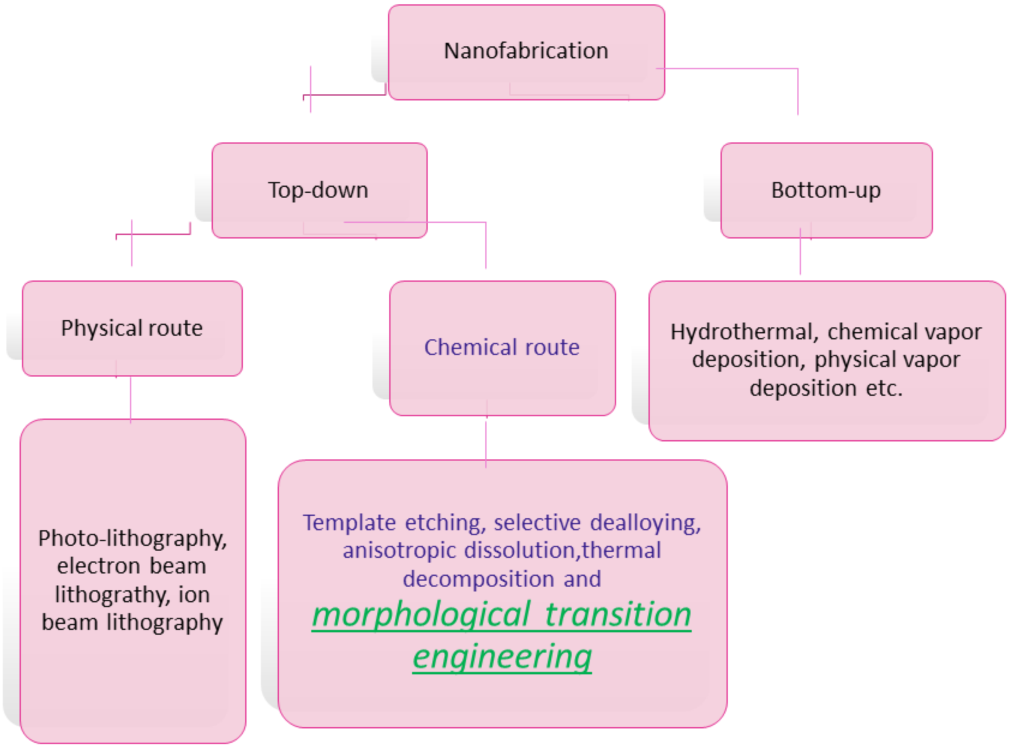

Figure 6.1: Nanofabrication methods.

Today, nanotechnology has been exquisitely developed so that we can fabricate nanostructures with limiting dimensions [138]. However, the need for a facile, cost-effective, large-area, implementable and quick approach to nanofabrication has always been a wishful quest. MTE, a technique for nanofabrication with control over the transition of the morphology of the semiconductor surface [137, 139], has the potential to be a technique of choice for producing desired nanostructures. However, after the literature survey, it is concluded that presently, the MTE technique is in an embryonic stage, which has been predominantly demonstrated in the solution phase [137]. Perhaps chemical-based MTE could be utilised further to obtain nanostructures in thin-films on demand.

So, in this work, we have developed a facile and cost-effective chemical route MTE technique to transform the CuO thin-film to honeycomb-like nanostructures via catalytic dissociation of H_2O_2.

It is worth noting here that CuO is a p-type semiconductor with the unique feature of high tunability of the bandgap from 1 eV to 4 eV [140, 62], desirable optoelectronic properties [141], phase stability [62], etc. It has been demonstrated for various applications like a photovoltaic solar cell [143], photodetector [141, 143], photocatalysis [144], gas sensors [145], biosensors [146, 147], etc. Although CuO is a semiconductor with good prospects for device applications, certain issues need to be addressed. Simple and reproducible nanostructure synthesis and doping schemes are required to be established [62]. Additionally, synthesising nanostructures via a pollution-free method is desirable [148, 149]. Owing to the above discussions, the developed MTE technique involves simple steps and is a reproducible method, and it has been ensured that there is minimal chemical usage and results in eco-friendly by-products (H_2O and O_2). Hence, this technique can be categorised as an environmentally benign method for CuO nanostructure synthesis.

In the present work, the effect of morphological change on optoelectronic properties is also investigated. Thereafter, due to morphological changes, the bandgap of the film is shifted. The effect of MTE on the electronic transport parameter was investigated, and the activation energy (E_a) for the CuO thin-film and nanostructure was obtained. Further, the optical response of the photodetector was improved after the MTE. However, the catalytic MTE approach in CuO thin-film resulted in increased effective channel length, which results in overall decreased responsivity of the catalytic MTE-based device.

6.2 Experimental details

Commercially available borosilicate glass substrates were ultrasonicated in acetone, isopropanol, and deionised water, respectively, for 10 minutes each. Hydrophilic treatment of all samples was performed for 20 min at 60 °C in a solution of H_2O:H_2O_2:NH_4OH with a ratio of 5:1:1 by volume. All the chemicals used were of reagent grade and were supplied by Sigma Aldrich. No further treatment or purification of the chemicals was performed. Figure 2. shows the steps followed to synthesise the CuO film over the substrate. Firstly, the seed solution was prepared by the continuous stirring of an aqueous colloidal solution of copper acetate for 24 hours. The second step was to spin-coat the prepared seed solution at 1000 rpm for 20 seconds over the glass substrate. Next, the sample was annealed at 250 °C for 30 min in an ambient oven. The obtained sample was cleaned in deionised water to remove the organic residue layer, and a smooth thin-film of CuO was obtained and adhered to the substrate. The obtained sample has been labelled as TF.

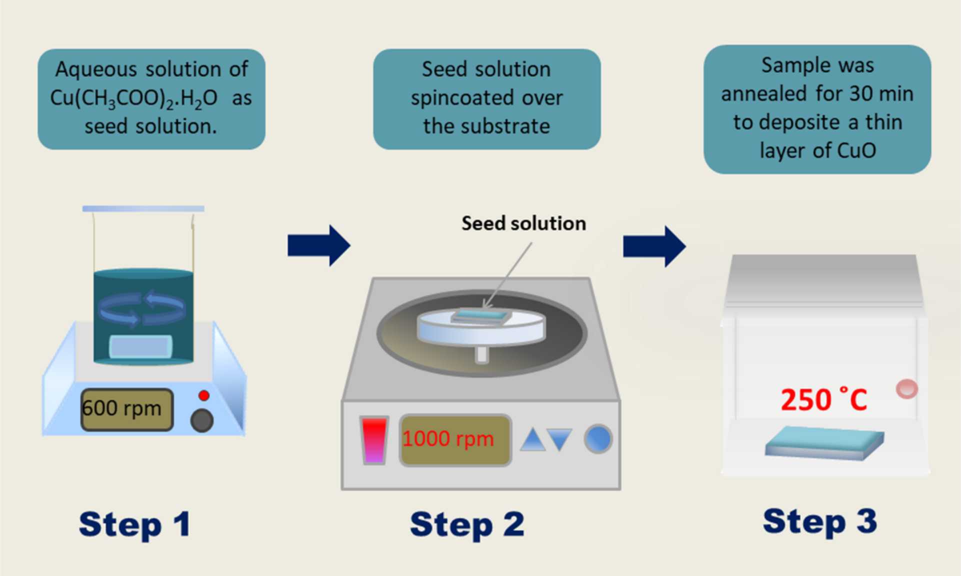

Figure 6.2: Procedure followed to synthesise CuO thin film.

Figure 3. represents the steps followed in the MTE technique. In

step 1, hydrogen peroxide (14 M) was simply dispersed drop by drop and spin-coated over the surface of the CuO thin-film. The dispersed H_2O_2 was left to soak over the sample and evaporate completely. The sample obtained after treating with H_2O_2 is denoted as NS throughout the manuscript. Notably, as compared to other solution processes (e.g., hydrothermal process) for nanostructure synthesis, this technique consumes fewer chemicals.

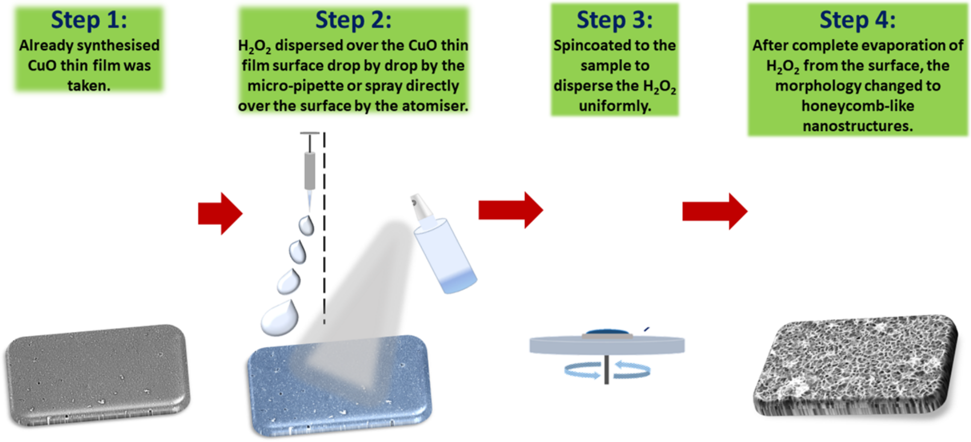

Figure 6.3: Steps involved in solution-processed morphological transition engineering technique.

Further, this article is arranged in the following manner. Firstly, a morphological investigation has been performed. Field emission scanning electron microscopy (FESEM, Zeiss Supra-55) was used to probe the morphology of the nanostructures. The synthesised semiconductor's phase purity is investigated by Raman spectroscopy. Horiba, Labram HR Evolution, from 200 cm^{-1} to 800 cm^{-1} was used for Raman spectroscopy. Subsequently, the process of MTE in CuO is discussed in detail. Then, the optical characterisation is discussed for which UV-Vis spectroscopy of the film was performed on Cary 60 UV-Vis, Agilent Technologies, in the range of 200 nm to 800 nm.

In the later section of this article, the device fabricated with CuO thin-films for UV-C light detection has been reported. The variation in the photodetector parameter has been investigated to argue for the effect of morphological transitions in the thin-film. The copper electrodes were deposited at a 1 Å/s rate by a physical vapour deposition technique, and a shadow mask was employed to define the channel region (50 μm). The electrodes were deposited up to an estimated thickness of 150 nm. The schematic of the device is shown in Fig. 6.4. The electrical characterisation of the fabricated device was performed using a Keithley 2612A dual-channel source meter. An optical light source of wavelength 254 nm at an intensity of 2.11 mWcm^{-2} was used to perform optical characterisation of the device.

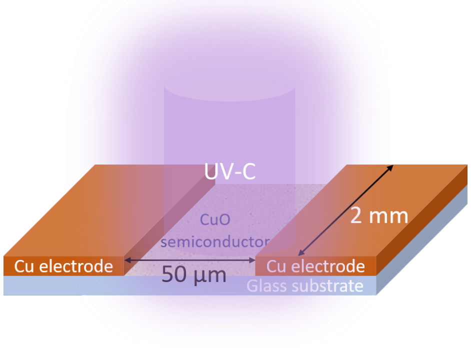

Figure 6.4: Schematic of the fabricated photodetector device

6.3 Results and discussion

6.3.1 Morphological investigation and basic characterisation

Fig. 6.5. shows the FESEM images for the morphological investigations of the TF and NS samples. Fig. 5(a). shows the TF surface texture, which confirms the formation of the smooth thin-film of CuO.

For detailed characterisation-related information about the TF (CuO thin-film) sample, reference [10] can be further referred. Thereafter, upon catalytic MTE, the morphology of sample TF completely transforms to honeycomb-like nanostructures (Fig. 6.5(b)). Moreover, the honeycomb-like nanostructure could be the manifestation of the network of nanoplates (further discussed in detail). Fig. 6.5(c) shows the cross-sectional image of the sample NS. The nanoplates formed observably have a thickness in the range of a few tens of nanometers.

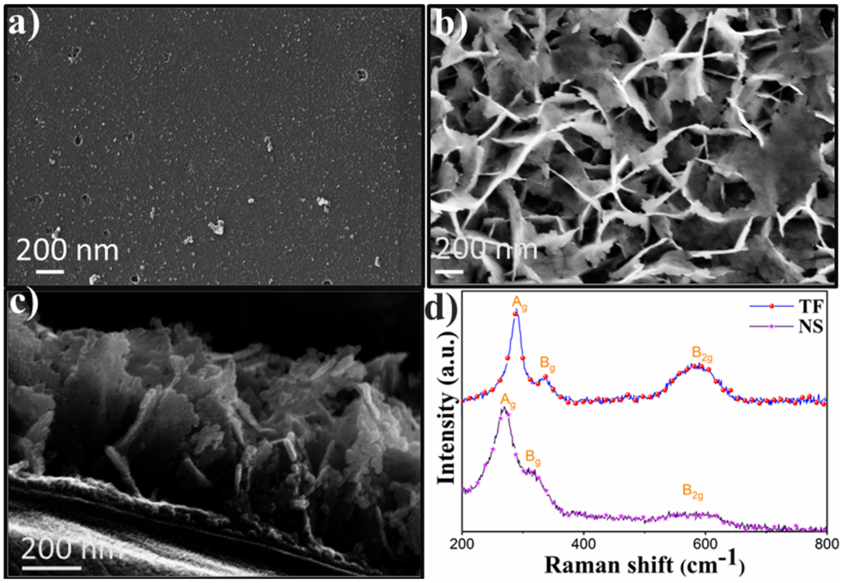

Figure 6.5: FESEM images for morphological investigation. a) TF sample, b) NS sample, c) NS sample cross-sectional image, and d) Raman spectra of TF and NS samples.

To confirm the formation of CuO, Raman spectroscopy was performed. The Raman spectra recorded for the TF and NS samples, respectively, are shown in Fig. 6.6. Raman spectra for TF shows A_g at 289 cm^{-1}, B_g at 337 cm^{-1}, and B_{2g} at 590 cm^{-1} modes, respectively, which are the three Raman active peaks of CuO. Further, the Raman spectra for the NS sample were at A_g at 270 cm^{-1}, B_g at 314 cm^{-1} and B_{2g} at 589 cm^{-1}, respectively. Table 1. below summarises the corresponding Raman peak values of the TF and NS samples. The shift in the peaks of the NS sample as compared to TF can be attributed to the nanostructure formation [44]. To investigate the optical properties of the samples, UV-Vis spectroscopy was performed. The absorption spectra in Fig. 6.6(a) show the absorption edge at 300 nm for both samples. The absorption in the TF sample is lower than the NS sample when the incident wavelength is lower than the absorption band edge. The absorption in the visible region is appreciably feeble as compared to the UV region. Moreover, in Fig. 6.5(b), the magnified image shows the effect of MTE over the absorbance of the TF sample. For the wavelength of the incident light above 300 nm, the absorption coefficient appreciably decreases in the NS sample compared to the TF sample. Similarly, the transmittance of the NS sample is higher for wavelengths higher than 300 nm as compared to the TF (Fig. 6.5(c)). Here, the change in the absorption of the NS sample can possibly be due to the suppression of midgap states [71]. The tauc-plot in Fig. 5 (d) shows the bandgap to be 4.08 eV and 4.12 eV for TF and NS samples, respectively. The blue shift in the bandgap after the MTE in the NS sample can again be attributed to the nanostructure formation and quantum confinement effect [46, 32, 140]. Further, in CuO, the electronic transitions are due to direct and indirect band transitions. However, as the bandgap of both samples is more than 3 eV, it is possibly due to direct band transitions.

6.3.2 Mechanism for morphological transition

The deposition of CuO thin-film over the glass substrate with the chemical bath deposition process is already a well-studied phenomenon. The mechanism for the same has been reported in the past [143, 150]. However, morphological transition in CuO nanostructures needs to be studied phenomenologically. In the MTE process, the CuO thin-film surface was transformed into a honeycomb-like nanostructure by treating the CuO surface with H_2O_2. It is well established that Cu^{2+} ions catalyse

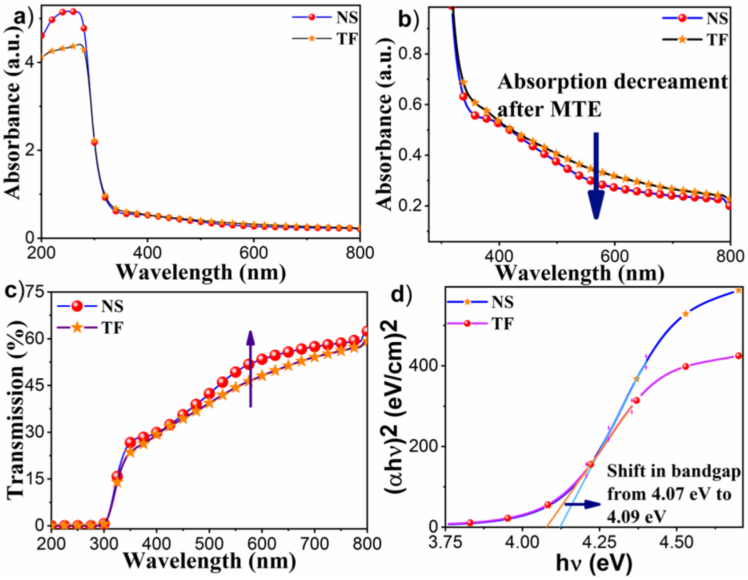

Figure 6.6: Wavelength-dependent absorption plot for TF and NS samples, b) magnified image of absorption plot for visible, c) transmission plot for TF and NS samples, and d) Tauc-plot showing the optical bandgap of the TF and NS samples.

the H_2O_2 dissociation reaction [151]. Here, we propose that the catalytic activity of Cu_{2+} in the dissociation of H_2O_2 might have led to the transformation in the morphology. As H_2O_2 is dispersed over the CuO surface, the H_2O_2 molecules get dissociated, henceforth Cu^{2+} and OH^- ions combine and result in $Cu(OH)_2$ (Fig. 6.6(a)). Further, as illustrated in Fig. 6.6(b), OH^- ions present in the solution have a tendency to combine with $Cu(OH)_2$, giving rise to ${Cu_n(OH)_{2n+2}}^{2+}$ chain, which results in strip-like structures formation. Fig. 6.6(b) also shows the possible chemical reactions involved. As the decomposition of H_2O_2 is an exothermic reaction, these chains of ${Cu_n(OH)_{2n+2}}^{2+}$ get thermally decomposed to CuO strips (Fig. 6.6(c)). The network of these CuO strips manifests itself in honeycomb-like nanostructures.

The above discussion presents the potential mechanism for the CuO thin-film transformation into honeycomb-like nanostructures via MTE. The above mechanism can be read in tandem with the references [151, 152, 153, 154]. It is noteworthy that the overall by-product of the reactions involved is H_2O and O_2. As this method does not produce any chemical wastes and ensures the least usage of chemical reagents compared to other solution-process techniques, therefore, it is an environmentally benign method to synthesise CuO nanostructures [148].

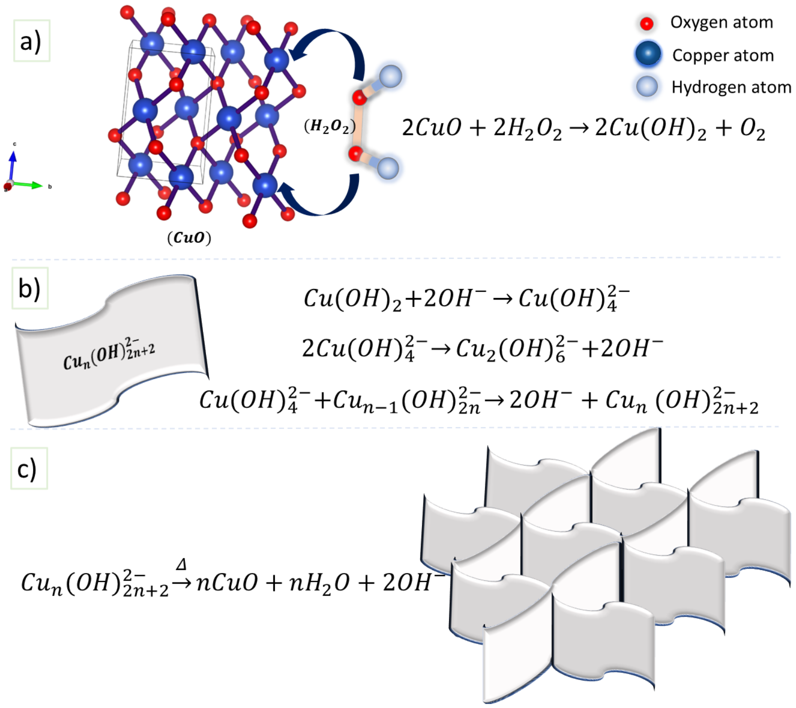

Figure 6.7: Growth mechanism of CuO nanoplates. a) upon dispersion of H_2O_2 over the CuO surface, the schematic representing the formation of $Cu(OH)_2$, b) chemical equations involved in the strip formation by aggregation of $Cun(OH)^{2-}{}_{2n+2}$ chains, and c) network of strips manifesting in honeycomb-like nanostructures.

To investigate the optoelectronic properties of the CuO samples, the planar electrode devices were fabricated (details provided in the experimental section). The active area of all the devices was 10^{-3} cm^2. In the device TF, the dark current varies linearly as the applied bias is varied between –20 V to +20 V range (Fig. 7). This confirms the formation of ohmic contact between the Cu electrode and the CuO thin-film. The temperature-dependent I-V curve is shown in the inset of Fig. 7. The enhancement in device current with the increase in temperature could be attributed to the thermal generation of charge carriers. The temperature-dependent I-V plot confirms the almost linear curve at higher temperatures. The Arrhenius plot of resistance versus reciprocal temperature was plotted to analyse the activation energy (E$_a$) of the trap states. In the case of semiconductors, the temperature dependence of resistance is governed by the equation:

$$R = R_0exp^{(}-\frac{E_a}{KT}) \tag{6.1}$$

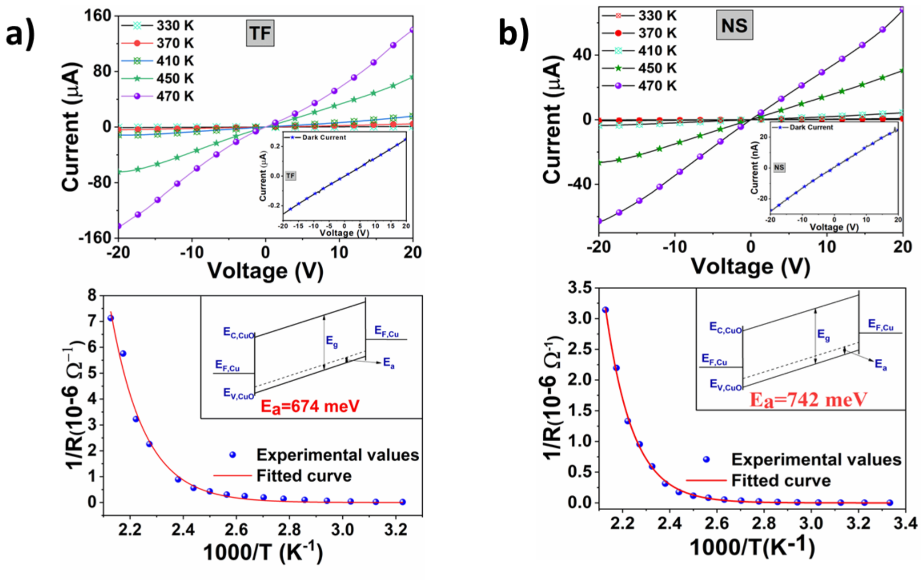

Figure 6.8: a) The top figure shows the room temperature I-V plot, and the inset shows the temperature-dependent I-V plot for the TF device. The below figure shows the Arrhenius plot of resistance versus reciprocal temperature; b) The top figure shows the room temperature I-V plot and the inset shows the temperature-dependent I-V plot for the NS device. The figure below shows the Arrhenius plot of resistance versus reciprocal temperature.

In the above equation, R$_0$ is the pre-exponential factor, k is the Boltzmann constant, and T is the temperature. Fig. 7 shows the reciprocal temperature-dependent resistance of the TF device. The value of E$_a$ was extracted by curve fitting, which was found to be 674 meV. Hence, there is a trap level above the valence band of CuO, which is predominantly due to the presence of copper vacancies [39, 150]. Similarly, Fig. 8 (a). shows the I-V plot for the NS device in ambient, and the inset shows the temperature-dependent plot. It is evident that the I-V curve is linear, hence again confirming the formation of ohmic behaviour in the transport of charge carriers. Fig. 8 (b). shows the temperature-dependent resistance offered by the CuO semiconductor thin-film after MTE. The activation energy of the NS sample is extracted to be 742 meV. The change in the activation energy reflects the change in the energy levels of the trap states, which is related to the MTE process. The change in the activation energy reflects that the MTE process may even have affected the other properties of the CuO thin-film. Further, to investigate the changes in the optoelectronic properties, UV-C light was illuminated over the devices, and different photodetector parameters were evaluated for both devices. Furthermore, here, the choice of the excitation wavelength (254 nm) was based on the spectra of light absorption, as the TF and NS samples absorb appreciably in the deep UV region.

Device fabricated with TF The TF device fabricated has a dark current, Id 0.26 µA at the applied voltage bias of 20 V (Fig. 9). Under 254 nm wavelength light illumination conditions, the device current of 0.9 µA for the bias of 20 V was recorded. The device photoresponsivity, R, was found to be 308 mAW^{-1} and photosensitivity, S of 2.5. Similarly, detectivity, D* was calculated to be 3.4×10^{10} J, and EQE was 211%.

Device fabricated with NS The dark current recorded was 27 nA for 20 V bias voltage (Fig. 10). Further, the photocurrent under 254 nm light illumination was 0.55 µA. This device's R was 248 mAW^{-1} and S was 19.4. The D* was 8.45×10^{10} J, and the EQE of the device was 128%.

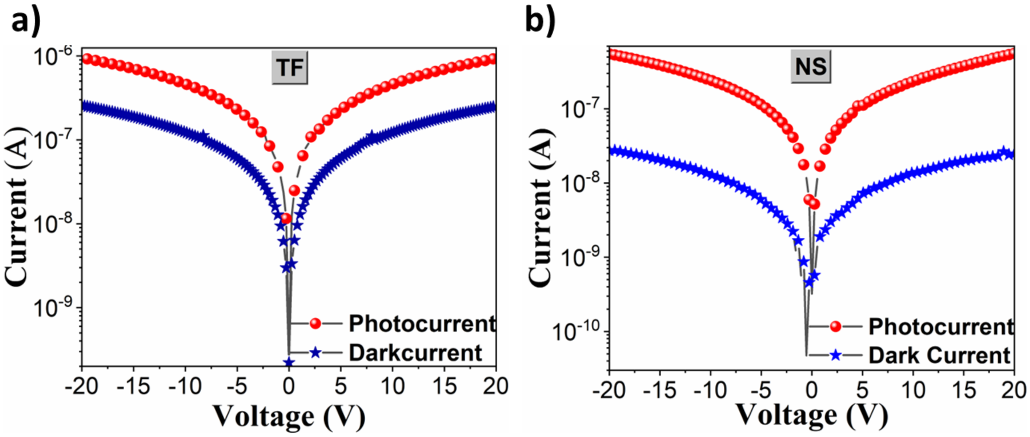

Figure 6.9: a) I-V plot in dark and illuminated conditions for TF device.; b) I-V plot in dark and illuminated conditions for NS device.

Table 2. shows the summary of the devices' performance. It is evident that most of the photodetector device parameters are improved upon applying the MTE process. The dark current reduction in device NS in comparison to device TF can be attributed to nanostructure formation in the NS sample. The effective resistive path length in the channel region is enhanced since the charge carriers have to traverse a zig-zag path, unlike the smooth thin-film device 30. However, the responsivity of the TF device is better. This could possibly be again due to the shorter channel length offered by the TF device. The photogenerated carriers in TF have a better probability of reaching the other electrode before recombination. But in the case of the NS device, there is much possibility that the generated carriers get recombined while travelling through the zig-zag path. Therefore, the photo-current is higher in TF and is much better compared to the NS device. Although NS offers improved sensitivity and detectivity. This could be attributed to the improved dark current in the NS device, i.e., reduced dark current as compared to the TF device.

6.4 Conclusions

In summary, solution-processed CuO nanostructures were utilised to fabricate UV-C (254 nm) photodetector with dark current, specific detectivity, and photosensitivity of 260 nA, 3.4×10^{10} Jones, and 2.5, respectively. A novel method has been developed for the morphological transformation of the as-synthesised smooth thin-film into a honeycomb-like nanostructured surface. The developed MTE technique also tunes the absorbance and, hence, the bandgap of the CuO film. The device fabricated by the MTE technique shows dark current 27 nA, specific detectivity, and photosensitivity of 8.5×10^{10} Jones, and 19.4, respectively. This article highlights that the developed novel chemical-based MTE process can be used to improve the device's performance. This achievement could pave the way for further maturing of the chemical route for nanofabrication for the fabrication of devices. This work might also open a new avenue for research in alternative device fabrication techniques that can be cheaper and more facile than the existing ones.

The main highlights of this technique are:

1. Cheaper, fast, facile and environmentally benign.
2. The morphological transition from CuO thin-film to honey-comb-like nanostructure.
3. Bandgap tuning of the CuO semiconductor.
4. Performance of photodetector improved.
5. Future scope of this could be to achieve doping certain elements in CuO lattice.

Chapter 7

Conclusion and Future Work

7.1 Conclusions

In summary, a hydrothermal seed-layer-assisted growth technique has been employed to synthesise CuO nanostructure. Potassium permanganate ($KMnO_4$) has been used as an additive in the precursor solution. To control the morphology and optoelectronic properties of the CuO nanostructures, the concentration of $KMnO_4$ is varied. Bandgap-tuned CuO nanostructures were synthesised from broadband absorption to UV-C absorbance with the varied available density of states for direct and indirect bandgap transitions. Bandgap-tuned CuO nanostructure-based UV-C, broadband, and NIR photodetectors have been fabricated and demonstrated.

The CuO seed layer synthesised was used as a thin-film for the fabrication of the photodetector device. The synthesised thin-film has shown more than 90 % transparency for the visible spectral region and had appreciable absorption in the UV region for wavelengths smaller than 300 nm. The fabricated device shows the least response to the light source of wavelengths in the visible region. The device's R_{DUV}/R_{Vis} ratio is close to 5400, which confirms the solar-blind photodetection. In addition, the device has also shown PPC effect with a huge retention time. To project the applicability of the PPC in real applications, we have developed a technique for set and reset mechanisms based on thermal and NIR heating.

Further, to improve the solar-blind characteristics of the device, the quality of the thin-flim was enhanced. A pristine half-hour growth of nanostructure over the seed layer was performed. The resulting nanostructured thin-film shows enhanced transparency in the visible region and absorption in the UV region due to improved crystallinity and quantum confinement effect. The synthesised nanostructured thin-flim has a bandgap of 4.13 eV, which categorises it into an ultrawide-bandgap semiconductor. Compared to the smooth thin-film-based device, the nanostructured thin-film-based device has shown improved photodetection based on all parameters like responsivity, sensitivity, detectivity, and response time. This device's performance, if not better, is comparable to the other reported devices based on different wide-bandgap semiconductors.

Lastly, a unique environmentally benign technique for the synthesis of CuO nanostructure has been developed. This post synthesise morphological transition engineering (MTE) technique was employed over the smooth thin-flim to transform it into a nanostructured thin-flim. In this technique, hydrogen peroxide (H_2O_2) is dispersed over the CuO thin-film and let it evapourate. The catalytic activity of Cu^{2+} ions driven reaction results in a chain-like reaction, which ultimately results in a strip-like structure. These strip-like structures form a network of strips and manifest into honeycomb-like structures.

7.2 Future Work

We have explored CuO semiconductors for varied bandgaps and, hence, fabricated photodetector devices with variable spectral ranges. The direct and indirect transition bandgaps are tuned to obtain the desired bandgap. We have employed a photoconductor device configuration with planar electrodes for the fabrication of the devices. Following are the limitations of this work and the scope for future works:

1. In this thesis, we have only considered pristine CuO semiconductors to attain desirable optoelectronic characteristics. However, appropriate dopping with careful selection of the dopant can result in desirable optoelectronic properties.
2. Different synthesis processes could be explored to synthesise CuO semiconductors with varied bandgap.
3. Different device configurations like photodiodes based on the Schottky junction could be employed for improving the transient response time of the photodetector.
4. Heterojunction device could be fabricated with the proper selection of the n-type semiconductor like ZnO to improve the transient response and spectral selectivity of the device.
5. The phenomena of the PPC effect in CuO could be a topic for further investigation.
6. The process of MTE can offer huge potential for on-demand CuO nanostructure synthesis. In addition to H_2O_2, other reactants could be employed to modify the reaction rate or the mechanism to attain the desirable morphology of nanostructures.

References

[1] Q. Zhang, K. Zhang, D. Xu, G. Yang, H. Huang, F. Nie, C. Liu, and S. Yang (2014), CuO nanostructures: Synthesis, characterisation, growth mechanisms, fundamental properties, and applications, Prog. Mater. Sci. 60, 208 (doi: http://dx.doi.org/10.1016/j.pmatsci.2013.09.003)

[2] Steven A. McDonald, Gerasimos Konstantatos, Shiguo Zhang, Paul W. Cyr, Ethan J. D. Klem, Larissa Levina, Edward H. Sargent (2005), Solution-processed PbS quantum dot infrared photodetectors and photovoltaics, Nature Materials, 4, 138-142 (doi: https://doi.org/10.1038/nmat1299)

[3] Malkeshkumar Patel, Hong-Sik Kim, Hyeong-Ho Park, and Joondong Kim (2016), Silver nanowires-templated metal oxide for broadband Schottky photodetector, Appl. Phys. Lett. 108, 141904 (doi: https://doi.org/10.1063/1.4945432)

[4] Antoni Rogalski (2003), Infrared detectors: status and trends, Progress in Quantum Electronics, 27, 2-3, 59-210 (doi: https://doi.org/10.1016/S0079-6727(02)00024-1)

[5] F. H. L. Koppens, T. Mueller, Ph. Avouris, A. C. Ferrari, M. S. Vitiello and M. Polini (2014), Photodetectors based on graphene, other two-dimensional materials and hybrid systems, Nat. Nanotechnol., 9, 780–793 (doi: https://doi.org/10.1038/nnano.2014.215)

[6] Fakun Wang, Yue Zhang, Yu Gao, Peng Luo, Jianwei Su, Wei Han, Kailang Liu, Huiqiao Li, and Tianyou Zhai (2019), 2D metal chalcogenides for IR photodetection, 1901347 (doi: https://doi.org/10.1002/smll.201901347)

[7] M. Patel, H. S. Kim, H. H. Park, and J. Kim (2006), Silver nanowires-templated metal oxide for broadband Schottky photodetector, Appl. Phys. Lett., 108, 141904 (doi: https://doi.org/10.1063/1.4945432)

[8] P.V. Karthik Yadav, B. Ajitha, Y. Ashok Kumar Reddy, Adem Sreedhar (2021), Recent advances in development of nanostructured photodetectors from ultraviolet to infrared region: A review, Chemosphere, 279, 130473 (doi: https://doi.org/10.1016/j.chemosphere.2021.130473)

[9] M. Razeghi (2002), Short-wavelength solar-blind detectors-status, prospects, and markets, Proc. IEEE. 90, 1006 (doi: https://doi.org/10.1109/JPROC.2002.1021565)

[10] T. Dixit, A. Tripathi, K. L. Ganapathi, I. A. Palani, M. S. R. Rao, and V. Singh (2019), Solution-processed transparent CuO thin films for solar-blind photodetection, IEEE Electron Device Lett. 40, 255 (doi: https://doi.org/10.1109/LED.2018.2886928)

[11] Rui Dong, Cheng Bi, Qingfeng Dong, Fawen Guo, Yongbo Yuan, Yanjun Fang, Zhengguo Xiao, Jinsong Huang (2014), An ultraviolet-to-NIR broad spectral nanocomposite photodetector with gain, Adv. Optical Mater., 2, 549-554 (doi: https://doi.org/10.1002/adom.201400023)

[12] N. Alidoust, M. C. Toroker, J. A. Keith, and E. A. Carter (2014), Significant Reduction in NiO Band Gap

Upon Formation of $\mathrm{Li}_x\mathrm{Ni}_(1 - x)\mathrm{O}$ alloys: Applications To Solar Energy Conversion, ChemSusChem 7, 195 (doi: https://doi.org/10.1002/cssc.201300595)

[13] Chun-Ho Lin, Hui-Chun Fu, Bin Cheng, Meng-Lin Tsai, Wei Luo, Lihui Zhou, Soo-Hwan Jang, Liangbing Hu and Jr-Hau He (2018), A flexible solar-blind 2D boron nitride nanopaper-based photodetector with high thermal resistance, npj 2D Mater Appl, 2, 23 (doi: https://doi.org/10.1038/s41699-018-0070-6)

[14] Dung-Sheng Tsai, Wei-Cheng Lien, Der-Hsien Lien, Kuan-Ming Chen, Meng-Lin Tsai, Debbie G. Senesky, Yueh-Chung Yu, Albert P. Pisano and Jr-Hau He (2013), Solar-Blind Photodetectors for Harsh Electronics, Sci. Rep, 3, 2628 (doi: https://doi.org/10.1038/srep02628)

[15] Dinesh Pratap Singh and Naushad Ali (2010), Synthesis of TiO_2 and CuO Nanotubes and Nanowires, Science of Advanced Materials, 41, 295-335 (doi: https://doi.org/10.1166/sam.2010.1095)

[16] Sambandam Anandan and Shihe Yang (2007), Emergent methods to synthesise and characterise semiconductor CuO nanoparticles with various morphologies, Journal of Experimental Nanoscience, 1, 2, 23-56 (doi: https://doi.org/10.1080/17458080601094421)

[17] Li, Y., Yang, X.Y., Feng, Y., Yuan, Z.Y. and Su, B.L., 2012, One-dimensional metal oxide nanotubes, nanowires, nanoribbons, and nanorods: synthesis, characterizations, properties and applications. Critical Reviews in Solid State and Materials Sciences, 37, 1, 1-74 (doi: https://doi.org/10.1080/10408436.2011.606512)

[18] Filipič, G., and Cvelbar, U. 2012, Copper oxide nanowires: a review of growth. Nanotechnology, 23, 19, 194001 (doi: https://doi.org/10.1088/0957-4484/23/19/194001)

[19] Liu, Y., Chu, Y., Zhuo, Y., Li, M., Li, L., and Dong, L. 2007, Anion-controlled construction of CuO honeycombs and flowerlike assemblies on copper foils. Crystal growth and design, 7, 3, 467-470 (doi: https://doi.org/10.1021/cg060480r)

[20] Vaseem, M., Umar, A., Kim, S. H., and Hahn, Y. B. 2008, Low-temperature synthesis of flower-shaped CuO nanostructures by solution process: formation mechanism and structural properties. The Journal of Physical Chemistry C, 112, 15, 5729-5735 (doi: https://doi.org/10.1021/jp710358j)

[21] Zheng, X. G., Xu, C. N., Tomokiyo, Y., Tanaka, E., Yamada, H., and Soejima, Y. 2000, Observation of charge stripes in cupric oxide. Physical Review Letters, 85, 24, 5170 (doi: https://doi.org/10.1103/PhysRevLett.85.5170)

[22] Hugh MacDonald, A. 2001, Copper oxides get charged up. Nature, 414(6862), 409-410 (doi: https://doi.org/10.1038/35106685)

[23] Song, M. K., Park, S., Alamgir, F. M., Cho, J., and Liu, M. (2011), Nanostructured electrodes for lithium-ion and lithium-air batteries: the latest developments, challenges, and perspectives. Materials Science and Engineering: R: Reports, 72, 11, 203-252 (doi: https://doi.org/10.1016/j.mser.2011.06.001)

[24] Choi, K. J., and Jang, H. W. (2010), One-dimensional oxide nanostructures as gas-sensing materials: review and issues. Sensors, 10, 4, 4083-4099 (doi: https://doi.org/10.3390/s100404083)

[25] Rahman, M. M., Saleh Ahammad, A. J., Jin, J. H., Ahn, S. J., and Lee, J. J. (2010), A comprehensive review of glucose biosensors based on nanostructured metal-oxides. Sensors, 10(5), 4855-4886 (doi: https://doi.org/10.3390/s100504855)

[26] Zhu, Y. W., Yu, T., Cheong, F. C., Xu, X. J., Lim, C. T., Tan, V. B. C., ... and Sow, C. H. (2004), Large-scale synthesis and field emission properties of vertically oriented CuO nanowire films. Nanotechnology, 16(1), 88 (doi: https://doi.org/10.1088/0957-4484/16/1/018)

[27] Zhang, X., Shi, W., Zhu, J., Kharistal, D. J., Zhao, W., Lalia, B. S., ... and Yan, Q. (2011), High-power and high-energy-density flexible pseudocapacitor electrodes made from porous CuO nanobelts and single-walled carbon nanotubes. ACS nano, 5(3), 2013-2019. (doi: https://doi.org/10.1021/nn1030719)

[28] Ali, I. (2012), New generation adsorbents for water treatment. Chemical Reviews, 112, 10, 5073-5091 (doi: https://doi.org/10.1021/cr300133d)

[29] Yu, X. Y., Xu, R. X., Gao, C., Luo, T., Jia, Y., Liu, J. H., and Huang, X. J. (2012), Novel 3D hierarchical cotton-candy-like CuO: surfactant-free solvothermal synthesis and application in As (III) removal. ACS Applied materials and interfaces, 4, 4, 1954-1962. (doi: https://doi.org/10.1021/am201663d)

[30] Kumar, R. V., Diamant, Y., and Gedanken, A. (2000), Sonochemical synthesis and characterisation of nanometer-size transition metal oxides from metal acetates. Chemistry of Materials, 12, 8, 2301-2305 (doi:https://doi.org/10.1021/cm000166z)

[31] Wei Zhou and Naoto Umezawa (2015), Band gap engineering of bulk and nanosheet SnO: an insight into the interlayer Sn-Sn lone pair interactions, Physical Chem. Chemical. Phy., 15, 17816-17820 (doi: https://doi.org/10.1039/C5CP02255J)

[32] Emma P. Mukhokosi, Saluru B. Krupanidhi and Karuna K. Nanda (2017), Band Gap Engineering of Hexagonal $SnSe_2$ Nanostructured

Thin Films for Infra-Red Photodetection, Sci. Rep., 7, 1703209 (doi: https://doi.org/10.1038/s41598-017-15519-x)

[33] Wei Chen, Juan Chen, Ye-Bin Feng, Lei Hong, Qi-Ying Chen, Ling-Feng Wu, Xin-Hua Lina and Xing-Hua Xia (2012), Peroxidase-like activity of water-soluble cupric oxide nanoparticles and its analytical application for detection of hydrogen peroxide and glucose, Analyst, 137, 1706 (doi: https://doi.org/10.1039/C2AN35072F)

[34] Su, D., Xie, X., Dou, S., and Wang, G. (2014), CuO single crystal with exposed 001 facets-A highly efficient material for gas sensing and Li-ion battery applications. Scientific reports, 4(1), 1-9 (doi: https://doi.org/10.1038/srep05753)

[35] Markus Heinemann, Bianca Eifert, and Christian Heiliger (2013), Band structure and phase stability of the copper oxides Cu_2O, CuO, and Cu_4O_3, Physical Review B 87, 115111 (doi: https://doi.org/10.1103/PhysRevB.87.115111)

[36] S. Asbrinnk and L.-J. Norrby (1970), Refinement of the Crystal Structure of Copper(II) Oxide with a Discussion of Some Exceptional E.s.d.'s, Acta Cryst., B26, 8 (doi: https://doi.org/10.1107/s0567740870001838)

[37] B. K. Meyer, et. al. (2013), Binary copper oxide semiconductors: From materials towards devices, Phys. Status Solidi B, 249(8), 1487-1509 (doi: https://doi.org/10.1002/pssb.201248128)

[38] Aleksandar Živkovic, Alberto Roldan, and Nora H. de Leeuw (2019), Density functional theory study explaining the underperformance of copper oxides as photovoltaic absorbers, Physical Review B, 99, 035154 (doi: https://doi.org/10.1002/pssb.201248128)

[39] Zufang Lin, et. al. (2018), Defect-concentration dependence of electrical transport mechanisms in CuO nanowires, RSC Adv., 8, 2188 (doi: https://doi.org/10.1039/c7ra11862g)

[40] F. P. Koffyberg, and F. A. Benko (1982), A photoelectrochemical determination of the position of the conduction and valence band edges of p-type CuO, J. Appl. Phys., 53(2), 1173-1177 (doi: https://doi.org/10.1063/1.330567)

[41] Tyler J. Smart, Allison C. Cardiel, Feng Wu, Kyoung-Shin Choi and Yuan Ping (2018), Mechanistic insights of enhanced spin polaron conduction in CuO through atomic doping, njp Computational Materials, 4, 61 (doi: https://doi.org/10.1038/s41524-018-0118-3)

[42] Junnan Wu, Bo Yin, Fei Wu, Yoon Myung, and Parag Banerjee (2014), Charge transport in single CuO nanowires, Applied Physics Letters, 105, 183506 (doi: https://doi.org/10.1038/s41524-018-0118-3)

[43] Aarti Sharma, Raj Kumar Dutta, Anirban Roychowdhury, and Dipankar Das (2016), Studies on structural defects in bare, PVP cappedand TPPO capped copper oxide nanoparticles by positron annihilation lifetime spectroscopy and their impact on photocatalytic degradation of rhodamine B, RSC Adv., 6, 74812 (doi: https://doi.org/10.1039/c6ra12795a)

[44] Anagh Bhaumik, Austin M. Shearin, A Rishi Patel and Kartik Ghosh (2014), Significant enhancement of optical absorption through nano-structuring of copper based oxide semiconductors: possible future materials for solar energy applications, Phys. Chem. Chem. Phys., 16, 11054 (doi: https://doi.org/10.1039/c4cp00827h)

[45] Bhusankar Talluri, Edamana Prasad, and Tiju Thomas (2018), Ultra-small (r$<$2 nm), stable ($>$1 year) copper oxide quantum dots with wide band gap, Superlattices and Microstructures, 113, 600-607 (doi: https://doi.org/10.1016/j.spmi.2017.11.044)

[46] X. Y. Chen, H. Cui, P. Liu, and G. W. Yang (2007), Shape-induced ultraviolet absorption of CuO shuttlelike nanoparticles, Applied Physics Letters, 90, 183118 (doi: https://doi.org/10.1063/1.2736285)

[47] Taegyun Kim, et al. (2017), Improvement in the Performance of Sol–Gel Processed In_2O_3 Thin-Film Transistor Depending on Sb Dopant Concentration, IEEE Electron Device Lett., 38, 8, 1027 (doi: https://doi.org/10.1063/1.2736285)

[48] M. Razeghi (2002), Short-wavelength solar-blind detectors-status, prospects, and markets, Proceedings of IEEE, 90, 6, 1027 (doi: https://doi.org/10.1109/JPROC.2002.1021565)

[49] M. Patel, Hong-Sik Kim, Hyeong-Ho Park, and Joondong Kim (2016), Silver nanowires-templated metal oxide for broadband Schottky photodetector, Applied Physics Letters, 108, 141904 (doi: https://doi.org/10.1063/1.4945432)

[50] Rui Dong, et al. (2014), An Ultraviolet-to-NIR Broad Spectral Nanocomposite Photodetector with Gain, Applied Physics Letters, 2, 6, 549-554 (doi: https://doi.org/10.1002/adom.201400023)

[51] Nima Alidoust, Maytal Caspary Toroker, John A. Keith, and Emily A. Carter (2013), Significant Reduction in NiO Band Gap Upon Formation of $Li_xNi_{1-x}O$ alloys: Applications To Solar Energy Conversion, ChemSusChem, 7, 1, 195-201 (doi: https://doi.org/10.1002/cssc.201300595)

[52] Fengren Cao, Wei Tian, Bangkai Gu, Bangkai Gu, Hao Lu, and Liang Li (2013), High-performance UV–vis photodetectors based on electrospun ZnO nanofiber-solution processed perovskite hybrid structures, Nano Research, 10, 2244-2256 (doi: https://doi.org/10.1007/s12274-016-1413-2)

[53] Ling Ning, Tianhao Jiang, Zhibin Shao, Ke Ding, Xiujuan Zhang, and Jiansheng Jie (2018), Light-trapping enhanced ZnO–MoS_2 core-shell nanopillar arrays for broadband ultraviolet-visible-near infrared photodetection, J. Mater. Chem. C, 6, 7077-7084 (doi: https://doi.org/10.1039/C8TC02139B)

[54] Kuo-Chin Wang, et al. (2014), Light-trapping enhanced ZnO-MoS_2 core-shell nanopillar arrays for broadband ultraviolet-visible-near infrared photodetection, J. Mater. Chem. C, 4, 4756 (doi: https://doi.org/10.1038/srep04756)

[55] Lei Meng, Jingbi You, and Yang Yang (2018), Addressing the stability issue of perovskite solar cells for commercial applications, Nature Communications, 9, 5265 (doi: https://doi.org/10.1038/s41467-018-07255-1)

[56] Zhongzheng Huang, et al. (2019), Amorphous MoS_2 Photodetector with Ultra-Broadband Response, ACS Appl. Electron. Mater., 1, 7, 1314-1321 (doi: https://doi.org/10.1021/acsaelm.9b00247)

[57] Alka Sharma, Biplab Bhattacharyya, A. K. Srivastava, T. D. Senguttuvan, and Sudhir Husale (2019), High performance broadband photodetector using fabricated nanowires of bismuth selenide, Scientific Reports, 6, 19138 (doi: https://doi.org/10.1038/srep19138)

[58] Du Xiang, Cheng Han, Jialin Zhang, T. D. Senguttuvan, and Wei Chen (2014), Gap States Assisted MoO_3 Nanobelt Photodetector

with Wide Spectrum Response, Scientific Reports, 4, 4891 (doi: https://doi.org/10.1038/srep04891)

[59] Jitesh Agrawal, Tejendra Dixit, I A Palani, M S Ramachandra Rao and Vipul Singh (2018), Fabrication of high responsivity deep UV photo-detector based on Na doped ZnO nanocolumns, J. Phys. D: Appl. Phys., 51, 185106 (doi: https://doi.org/10.1088/1361-6463/aab8d3)

[60] Hannes Raebiger, Stephan Lany, and Alex Zunger (2007), Origins of the p-type nature and cation deficiency in Cu_2O and related materials, Physical Review B, 76, 045209 (doi: https://doi.org/10.1103/PhysRevB.76.045209)

[61] Stephan Lany, and Alex Zunger (2007), Dopability, Intrinsic Conductivity, and Nonstoichiometry of Transparent Conducting Oxides, Physical Review Letters, 76, 045501 (doi: https://doi.org/10.1103/PhysRevLett.98.045501)

[62] Qiaobao Zhang, et al. (2014), CuO nanostructures: Synthesis, characterization, growth mechanisms, fundamental properties, and applications, Progress in Materials Science, 60, 208-337 (doi: https://doi.org/10.1016/j.pmatsci.2013.09.003)

[63] A. Bhaumik, A. M. Shearin, R. Patel, and K. Ghosh, (2014), Significant enhancement of optical absorption through nano-structuring of copper based oxide semiconductors: possible future materials for solar energy applications, Physical Chemistry Chemical Physics, 16, 11054-11066 (doi: https://doi.org/10.1039/C4CP00827H)

[64] Jiancheng Yang, Zachary Sparks, Fan Ren, Stephen J. Pearton, and Marko Tadjer, (2018), Effect of surface treatments on electrical

properties of β-Ga_2O_3, Journal of Vacuum Science and Technology B, 36, 061201 (doi: https://doi.org/10.1116/1.5052229)

[65] Jian-Jun Wang, Jin-Song Hu, Yu-Guo Guo, and Li-Jun Wan (2011), Eco-friendly visible-wavelength photodetectors based on bandgap engineerable nanomaterials, Journal of Materials Chemistry, 21, 17582-17589 (doi: https://doi.org/10.1039/C1JM12173A)

[66] Rui Dong, et al. (2014), An Ultraviolet-to-NIR Broad Spectral Nanocomposite Photodetector with Gain, Advanced Optical Materials, 2, 6, 549-554 (doi: https://doi.org/10.1002/adom.201400023)

[67] Wei Zhou and Naoto Umezawa (2015), Band gap engineering of bulk and nanosheet SnO: an insight into the interlayer Sn-Sn lone pair interactions, Phys. Chem. Chem. Phys., 17, 17816-17820 (doi: https://doi.org/10.1039/C5CP02255J)

[68] Wei Chen, et al. (2012), Peroxidase-like activity of water-soluble cupric oxidenanoparticles and its analytical application for detection of hydrogen peroxide and glucose, Analyst, 137, 1706-1712 (doi: https://doi.org/10.1039/C2AN35072F)

[69] X. Y. Chen, H. Cui, P. Liu, and G. W. Yang (2007), Shape-induced ultraviolet absorption of CuO shuttlelike nanoparticles, Applied Physics Letters, 90, 183118 (doi: https://doi.org/10.1063/1.2736285)

[70] Vani Pawar, Pradeep K. Jha, S. K. Panda, Priyanka A. Jha, and Prakhar Singh (2018), Band-Gap Engineering in ZnO Thin Films A Combined Experimental and Theoretical Study, Phys. Rev. Applied, 9, 054001 (doi: https://doi.org/10.1103/PhysRevApplied.9.054001)

[71] Shama Rehman, A. Mumtaz, and S. K. Hasanain (2011), Size effects on the magnetic and optical properties of CuO nanoparticles, Journal of Nanoparticle Research, 13, 2497-2507 (doi: https://doi.org/10.1007/s11051-010-0143-8)

[72] Zufang Lin, et al. (2018), Defect-concentration dependence of electrical transport mechanisms in CuO nanowires, RSC Advances, 8, 2188-2195 (doi: https://doi.org/10.1039/C7RA11862G)

[73] Yeong Hwan Ko, Goli Nagaraju, Soo Hyun Lee, and Jae Su Yu (2014), Facile preparation and optoelectronic properties of CuO nanowires for violet light sensing, Materials Letters, 117, 217-220 (doi: https://doi.org/10.1016/j.matlet.2013.11.119)

[74] Khaled M. Chahrour, Naser M. Ahmed, M. R. Hashim, Nezar G. Elfadill, M. Bououdina (2016), Self-assembly of aligned CuO nanorod arrays using nanoporous anodic alumina template by electrodeposition on Si substrate for IR photodetectors, Sensors and Actuators A: Physical, 239, 209-219 (doi: https://doi.org/10.1016/j.sna.2016.01.034)

[75] Sojeong Lee, et al. (2018), Sol-Gel Processed p-Type CuO Phototransistor for a Near-Infrared Sensor, IEEE Electron Device Letters, 39, 1, 47-50 (doi: https://doi.org/10.1109/LED.2017.2779816)

[76] Lin-Bao Luo, et al. (2014), One-dimensional CuO nanowire: synthesis, electrical, and optoelectronic devices application, Nanoscale Research Letters, 9, 637 (doi: https://doi.org/10.1186/1556-276X-9-637)

[77] Tejendra Dixit, Akash Tripathi, K. L. Ganapathi, I. A. Palani, M. S. Ramachandran Rao, and Vipul Singh (2018), Solution-

Processed Transparent CuO Thin Films for Solar-Blind Photodetection, IEEE Electron Device Letters, 40, 2, 255-258 (doi: https://doi.org/10.1109/LED.2018.2886928)

[78] Zhen Guang Shao, et al. (2014), High-Gain AlGaN Solar-Blind Avalanche Photodiodes, IEEE Electron Device Letters, 35, 3, 372 - 374 (doi: https://doi.org/10.1109/LED.2013.2296658)

[79] Yangke Peng, et al. (2018), Arrays of Solar-Blind Ultraviolet Photodetector Based on β-Ga_2O_3 Epitaxial Thin Films, IEEE Photonics Technology Letters, 30, 11, 993-996 (doi: https://doi.org/10.1109/LPT.2018.2826560)

[80] Hongyu Chen, Kewei Liu, Linfeng Hu, Ahmed A. Al-Ghamdi, Xiaosheng Fang (2015), New concept ultraviolet photodetectors, Materials Today, 18, 9, 493-502 (doi: https://doi.org/10.1016/j.mattod.2015.06.001)

[81] Marco Girolami, et al. (2012), Diamond Detectors for UV and X-Ray Source Imaging, IEEE Electron Device Letters, 33, 2, 224-226 (doi: https://doi.org/10.1109/LED.2011.2176907)

[82] Frank Mendoza, Vladimir Makarov, Brad R. Weiner, and Gerardo Morell (2015), Solar-blind field-emission diamond ultraviolet detector, Applied Physics Letters, 107, 20, 201605 (doi: https://doi.org/10.1063/1.4936162)

[83] E Monroy, F Omnès, and F Calle (2003), Wide-bandgap semiconductor ultraviolet photodetectors, Semiconductor Science and Technology, 18, 4, R33 (doi: https://doi.org/10.1088/0268-1242/18/4/201)

[84] Wei Tian, Hao Lu, and Liang Li (2015), Nanoscale ultraviolet photodetectors based on onedimensional metal oxide nanostructures,

Nano Research, 8, 382–405 (doi: https://doi.org/10.1007/s12274-014-0661-2)

[85] Anamika Singh Pratiyush, et al. (2017), High responsivity in molecular beam epitaxy grown β-Ga_2O_3 metal semiconductor metal solar blind deep-UV photodetector, Applied Physics Letters,110, 22, 221107 (doi: https://doi.org/10.1063/1.4984904)

[86] Lin-Bao Luo, et al. (2016), Electronic structures of A joint experimental and theoretical study, Physical Review B, 94, 245418 (doi: https://doi.org/10.1103/PhysRevB.94.245418)

[87] Anamika Singh Pratiyush, et al. (2014), One-dimensional CuO nanowire: synthesis, electrical, and optoelectronic devices application, Nanoscale Res Lett., 9, 637 (doi: https://doi.org/10.1186/1556-276X-9-637)

[88] Yeong Hwan Ko, Goli Nagaraju, Soo Hyun Lee, Jae Su Yu (2014), Facile preparation and optoelectronic properties of CuO nanowires for violet light sensing, Materials Letters, 117, 217-220 (doi: https://doi.org//10.1016/j.matlet.2013.11.119)

[89] Sojeong Lee, et al. (2018), Sol-Gel Processed p-Type CuO Phototransistor for a Near-Infrared Sensor, IEEE Electron Device Letters, 39, 1, 47-50 (doi: https://doi.org/10.1109/LED.2017.2779816)

[90] N. R. Dhineshbabu, V. Rajendran, N. Nithyavathy, and R. Vetumperumal (2016), Study of structural and optical properties of cupric oxide nanoparticles, Applied Nanoscience, 6, 933–939 (doi: https://doi.org/10.1007/s13204-015-0499-2)

[91] Yasser K. Abdel-Monem, Sanaa M. Emam, and Hager M. Y. Okda (2017), Solid state thermal decomposition synthesis of CuO

nanoparticles from coordinated pyrazolopyridine as novel precursors, Journal of Materials Science: Materials in Electronics, 28, 2923–2934 (doi: https://doi.org/10.1007/s10854-016-5877-3)

[92] K.C. Sanal, L.S. Vikas, and M.K. Jayaraj (2017), Room temperature deposited transparent p-channel CuO thin film transistors, Applied Surface Science, 297, 153-157 (doi: https://doi.org/10.1016/j.apsusc.2014.01.109)

[93] D. Tahir, and S. Tougaard (2012), Electronic and optical properties of Cu, CuO and Cu_2O studied by electron spectroscopy, Journal of Physics: Condensed Matter, 24, 175002 (doi: https://doi.org/10.1088/0953-8984/24/17/175002)

[94] Peng Wang, Xinhong Zhao, and Baojun Li (2011), ZnO-coated CuO nanowire arrays: fabrications, optoelectronic properties, and photovoltaic applications, Optics Express, 19, 12, 11271-11279 (doi: https://doi.org/10.1364/OE.19.011271)

[95] Min-Kun Dai, Yi-Rou Liou, Jan-Tien Lian, Tai-Yuan Lin, and Yang-Fang Chen (2015), Multifunctionality of Giant and Long-Lasting Persistent Photoconductivity: Semiconductor–Conductor Transition in Graphene Nanosheets and Amorphous InGaZnO Hybrids, ACS Photonics, 2, 8, 1057–1064 (doi: https://doi.org/10.1021/acsphotonics.5b00084)

[96] Violet M. Poole, Slade J. Jokela, and Matthew D. McCluskey (2017), Using persistent photoconductivity to write a low-resistance path in $SrTiO_3$, Scientific Reports, 7, 6659 (doi: https://doi.org/10.1038/s41598-017-07090-2)

[97] Patrick J. Snyder, Ronny Kirste, Ramon Collazo, and Albena Ivanisevic (2017), Persistent Photoconductivity, Nanoscale

Topography, and Chemical Functionalization Can Collectively Influence the Behavior of PC12 Cells on Wide Bandgap Semiconductor Surfaces, Small, 13, 24, 1700481 (doi: https://doi.org/10.1002/smll.201700481)

[98] K. Macielak, M. Maciaszek, M. Igalson, P. Zabierowski, and N. Barreau (2017), Persistent Photoconductivity in Polycrystalline Cu(In,Ga)Se_2 Thin Films: Experiment Versus Theoretical Predictions, IEEE Journal of Photovoltaics, 5, 4, 1206-1211 (doi: https://doi.org/10.1109/JPHOTOV.2015.2423491)

[99] Dangxin Wu, Qiming Zhang, and Meng Tao (2006), LSDA+U study of cupric oxide: Electronic structure and native point defects, Physical Review B, 73, 235206 (doi: https://doi.org/10.1103/PhysRevB.73.235206)

[100] Stephan Lany and Alex Zunger (2005), Anion vacancies as a source of persistent photoconductivity in II-VI and chalcopyrite semiconductors, Physical Review B, 72, 035215 (doi: https://doi.org/10.1103/PhysRevB.72.035215)

[101] S. H. N. Lim, D. R. McKenzie, and M. M. M. Bilek (2009), Anion vacancies as a source of persistent photoconductivity in II-VI and chalcopyrite semiconductors, Physical Review B, 80, 075109 (doi: https://doi.org/10.1063/1.3183503)

[102] H. X. Jiang, G. Brown, and J. Y. Lin (1991), Persistent photoconductivity in II-VI and III-V semiconductor alloys and a novel infrared detector, Journal of Applied Physics, 69, 9, 6701–6703 (doi: https://doi.org/10.1063/1.348889)

[103] A. Bhatnagar, Y. H. Kim, D. Hesse, and M. Alexe (2014), Persistent photoconductivity in strained epitaxial

$BiFeO_3$ thin films, Nano Letters, 14, 9, 5224–5228 (doi: https://doi.org/10.1021/nl502183j)

[104] M. Razeghi (2002), Short-wavelength solar-blind detectors-status, prospects, and markets, Proc. IEEE, 90, 6, 1006–1014 (doi: https://doi.org/10.1109/JPROC.2002.1021565)

[105] C. Xie, et al. (2019), Recent progress in solar-blind deep-ultraviolet photodetectors based on inorganic ultrawide bandgap semiconductors, Adv. Funct. Mater., 29, 9, 1806006 (doi: https://doi.org/10.1109/JPROC.2002.1021565)

[106] J. Y. Tsao, et al. (2018), Ultrawide-bandgap semiconductors: Research opportunities and challenges, Adv. Electron. Mater., 4, 1, 1600501 (doi: https://doi.org/10.1002/aelm.201600501)

[107] F. Mendoza, V. Makarov, B. R. Weiner, and G. Morell (2018), Solar-blind field-emission diamond ultraviolet detector, Appl. Phys. Lett., 107, 20, 201605 (doi: https://doi.org/10.1063/1.4936162)

[108] S. Lee, et al. (2018), Sol-gel processed p-Type CuO phototransistor for a nearinfrared sensor, Appl. Phys. Lett., 39, 1, 47–50 (doi: https://doi.org/10.1109/LED.2017.2779816)

[109] W. B. Choi, et al. (1999), Sol-gel processed p-Type CuO phototransistor for a nearinfrared sensor, Appl. Phys. Lett., 75, 20, 3129 (doi: https://doi.org/10.1063/1.125253)

[110] K. Xu (2019), Silicon MOS optoelectronic micro-nano structure based on reverse-biased PN junction," Phys. Status Solidi (A), 216, 7, 1800868, (doi: https://doi.org/10.1002/pssa.201800868)

[111] W. Ouyang, F. Teng, J. H. He, and X. Fang (2019), Enhancing the photoelectric performance of photodetectors

based on metal oxide semiconductors by charge-carrier engineering," Adv. Funct. Mater., 29, 9, 1807672 (doi: https://doi.org/10.1002/adfm.201807672)

[112] D. Zhu, L. Wang, W. Yu, and H. Xie (2018), Intriguingly high thermal conductivity increment for CuO nanowires contained nanofluids with low viscosity," Sci. Rep., 8, 5282, (doi: https://doi.org/10.1038/s41598-018-23174-z)

[113] Y. K. Abdel-Monem, S. M. Emam, and H. M. Y. Okda (2017), Solid state thermal decomposition synthesis of CuO nanoparticles from coordinated pyrazolopyridine as novel precursors," J. Mater. Sci., Mater. Electron., 28, 3, 2923–2934 (doi: https://doi.org/10.1007/s10854-016-5877-3)

[114] T. Dixit, A. Tripathi, K. L. Ganapathi, M. S. R. Rao, and V. Sing (2020), Longlasting persistent photoconductivity in Au/CuO thin films for optical memory, IEEE Photon. Technol. Lett., 36, 6, 329–332, (doi: https://doi.org/10.1109/LPT.2020.2973725)

[115] T. C. Wei, et al. (2014) See-through Ga_2O_3 solar-blind photodetectors for use in harsh environments," IEEE J. Sel. Top. Quantum Electron., 20, 6, 372 (doi: https://doi.org/10.1109/JSTQE.2014.2321517)

[116] J. Wu, B. Yin, F. Wu, Y. Myung, and P. Banerjee (2014), Charge transport in single CuO nanowires," Appl. Phys. Lett., 105, 18, 183506 (doi: https://doi.org/10.1063/1.4900966)

[117] S. Rathkanthiwar, A. Kalra, S. V. Solanke, N. Mohta, R. Muralidharan, S. Raghavan, and D. N. Nath (2017), Gain mechanism and carrier transport in high responsivity AlGaN-based solar blind metal semiconductor metal photodetectors," J. Appl. Phys., 121, 16, 164502, (doi: https://doi.org/10.1063/1.4982354)

[118] X. Xie, Z. Zhang, B. Li, S. Wang, and D. Shen (2015), Ultra-low threshold avalanche gain from solar-blind photodetector based on graded-bandgap-cubic-MgZnO, Opt. Express, 23, 25, 32329 (doi: https://doi.org/10.1364/OE.23.032329)

[119] T. Dixit, J. Agrawal, K. L. Ganapathi, V. Singh, and M. S. R. Rao (2019), High-performance broadband photodetection in solution-processed ZnO-$ZnCr_2O_4$ nanowalls, IEEE Electron Device Lett., vol. 40, no. 7, 143–1146, (doi: https://doi.org/10.1109/LED.2019.2916628)

[120] L. Qian, Z.-H. Wu, Y.-Y. Zhang, P. T. Lai, X.-Z. Liu, and Y.-R. Li (2017), Ultrahigh-responsivity, rapid-recovery, solar-blind photodetector based on highly nonstoichiometric amorphous gallium oxide, ACS Photon., 4, 9, 2203–2211 (doi: https://doi.org/10.1021/acsphotonics.7b00359)

[121] M. Marie, S. Mandal, and O. Manasreh (2015), An electrochemical glucose sensor based on zinc oxide nanorods, Sensors, 15, 8, 18714 (doi: https//doi.org/10.3390/s150818714)

[122] K. Xu, Y. Chen, T. A. Okhai, and L. W. Snyman(2019), Micro optical sensors based on avalanching silicon light-emitting devices monolithically integrated on chips, Opt. Mater. Express, vol. 9, no. 10, p. 3985 (doi: https://doi.org/10.1364/OME.9.003985)

[123] L. Dong, J. Yu, R. Jia, J. Hu, Y. Zhang, and J. Sun (2019), Self-powered MSM deep-ultraviolet β-Ga_2O_3 photodetector realized by an asymmetrical pair of Schottky contacts, Opt. Mater. Express, 9, 3, 1191–1199 (doi: https://doi.org/10.1364/OME.9.001191)

[124] S.-H. Yuan, C.-C. Wang, S.-Y. Huang, and D.-S. Wuu (2018), Improved responsivity drop from 250 to 200 nm in sput-

tered gallium oxide photodetectors by incorporating trace aluminum, IEEE Electron Device Lett., 39, 2, 220–223 (doi: https://doi.org/10.1109/LED.2017.2782693)

[125] Z. G. Shao, et al. (2014), High-gain AlGaN solar-blind avalanche photodiodes, IEEE Electron Device Lett., 35, 3, 372–374, (doi: https://doi.org/10.1109/LED.2013.2296658)

[126] C. H. Chen and C. T. Lee (2015), Solar blind ultraviolet photodetectors with high dynamic resistance using $Zn_3Ta_2O_5$ layer, IEEE Photon. Technol. Lett., 27, 17, 1817–1820 (doi: https://doi.org/10.1109/LPT.2015.2443502)

[127] D. P. Chaudhari, et al. (2015), Solar blind photodetectors enabled by nanotextured β-Ga_2O_3 films grown via oxidation of GaAs substrates," IEEE Photon. J., 9, 2, 2300207 (doi: https://doi.org/10.1109/JPHOT.2017.2688463)

[128] W. Y. Kong, G. A. Wu, K. Y. Wang, T. F. Zhang, Y. F. Zou, D. D. Wang, and L. B. Luo (2016), Graphene-β-Ga_2O_3 heterojunction for highly sensitive deep uv photodetector application, Adv. Mater., 28, 48, 10725–10731 (doi: https://doi.org/10.1002/adma.201604049)

[129] W. J. Kuang, X. Liu, Q. Li, Y. Liu, J. Su, and H. Tolner (2018), Solution-processed solar-blind ultraviolet photodetectors based on ZnS quantum dots, IEEE Photon. Technol. Lett., 30, 15, 1384–1387, (doi: https://doi.org/10.1109/LPT.2018.2849345)

[130] Y. Peng, Y. Zhang, Z. Chen, D. Guo, X. Zhang, P. Li, Z. Wu, and W. Tang (2018), Arrays of solar-blind ultraviolet photodetector based on β-Ga_2O_3 epitaxial thin films," IEEE Photon. Technol. Lett., 30, 11, 993-996,(doi: https://doi.org/10.1109/LPT.2018.2826560)

[131] R. Feynman (1960), There's plenty of room at the bottom, Eng. Sci., 23, 22

[132] H.-D. Yu, M. D. Regulacio, E. Ye, and Ming-Yong Han (2013), Chemical routes to top-down nanofabrication, Chem. Soc. Rev. Rev, 42, 6006-6018 (doi: https://doi.org/10.1039/C3CS60113G)

[133] P. Iqbal, J. A. Preece, and P. M. Mendes, Nanotechnology The 'Top-Down' and 'Bottom-Up' Approaches, in Supramolecular Chemistry: From Molecules to Nanomaterials, John Wiley and Sons, Ltd., 2012

[134] H. Ahmed (1991), Nanostructure Fabrication, Proc. IEEE, 79, 8, 1140-1148 (doi: https://doi.org/10.1109/5.92073)

[135] H. Wang, M. Sun, K. Ding, M. T. Hill, and C. Ning (2011), A Top-down Approach to Fabrication of High Quality Vertical Heterostructure Nanowire Arrays, Nano Lett., 11, 1646-1650 (doi: https://doi.org/10.1021/nl2001132)

[136] A. Biswas, I. S. Bayer, A. S. Biris, T. Wang, E. Dervishi, and F. Faupel (2012), Advances in Top-Down and Bottom-up Surface Nanofabrication Techniques, Applications and Future Prospects, Adv. Colloid Interface Sci., 170, 1-2, 2-27 (doi: https://doi.org/10.1016/j.cis.2011.11.001)

[137] A. H. Abdelmohsen, W. M. A. E. Rouby, N. Ismail, and A. A. Farghali (2017), Morphology Transition Engineering of ZnO Nanorods to Nanoplatelets Grafted Mo8O_{23}-MoO_2 by Polyoxometalates Mechanism and Possible Applicability to other Oxides, Sci. Rep., 7, 1, 1-26

[138] D. Eigler, M and E. Scweizer (1990), K, Positioning single atoms with a scanning tunnelling microscope, Nature, 344, 524-526

[139] S. Yerra, S. Supriya, and S. K. Das (2013), “Reversible morphological transition between nano-rods to micro-flowers through micro-hexagonal crystals in a sonochemical synthesis based on a polyoxovanadate compound,” Inorg. Chem. Commun., 35, 54-57

[140] A. Tripathi, T. Dixit, J. Agrawal, and V. Singh (2020), Bandgap engineering in CuO nanostructures: Dual-band, broadband, and UV-C photodetectors, Appl. Phys. Lett., 116, 11, 111102

[141] H. J. Song, M. H. Seo, K. W. Choi, M. S. Jo, J. Y. Yoo, and J. B. Yoon (2019), High-Performance Copper Oxide Visible-Light Photodetector via Grain-Structure Model, Sci. Rep., 9, 1, 1-10

[142] P. Raksa, S. Nilphai, A. Gardchareon, and S. Choopun (2009), Copper oxide thin film and nanowire as a barrier in ZnO dye-sensitized solar cells, Thin Solid Films, 517, 17, 4741-4744

[143] T. Dixit, A. Tripathi, S. V. Solanke, K. L. Ganapathi, M. S. R. Rao, and V. Singh (2020), Ultra-Wide Bandgap Copper Oxide High Performance Solar-Blind Photo-detection, IEEE Electron Device Lett., vol. 41, 12, 1790-1793

[144] A. F. Zedan, A. T. Mohamed, M. S. El-Shall, S. Y. Alqaradawi, and A. S. Aljaber (2018), Tailoring the reducibility and catalytic activity of CuO nanoparticles for low temperature CO oxidation, RSC Adv., 8, 35, 19499-19511

[145] J. Zhang, J. Liu, Q. Peng, X. Wang, and Y. Li (2006), Nearly monodisperse Cu2O and CuO nanospheres: Preparation and applications for sensitive gas sensors, Chem. Mater., 18, 4, 867-871

[146] E. R. Glucose (2020), “CuO Nanowire-Based Extended-Gate Field-Effect-Transistor (FET) for pH Sensing,” IEEE Sens. J., vol. 20, no. 9, pp. 5039-5047

[147] N. Verma and N. Kumar (2019), Synthesis and Biomedical Applications of Copper Oxide Nanoparticles: An Expanding Horizon, ACS Biomater. Sci. Eng., 5, 1170-1188

[148] J. M. Patete, X. Peng, C. Koenigsmann, Y. Xu, B. Karn, and S. S. Wong (2011), Viable methodologies for the synthesis of high-quality nanostructures, Green Chem., 13, 3, 482-519

[149] K. Hassan, R. Hossain, and V. Sahajwalla (2021), Novel microrecycled ZnO nanoparticles decorated macroporous 3D graphene hybrid aerogel for efficient detection of NO2 at room temperature, Sensors Actuators, B Chem., 330, 129278

[150] A. Tripathi, J. Agrawal, T. Dixit, and V. Singh (2020), Trap Assisted Persistent Photo-Conductivity in Solution-Processed CuO Thin Film, IEEE J. Quantum Electron., 56, 1, 1-5

[151] L. C. Carvalho, A. C. Matias, C. S. Nomura, and G. Cerchiaro (2011), Radical production by hydrogen peroxide / bicarbonate and copper uptake in mammalian cells Modulation by Cu(II) complexes, J. Inorg. Biochem., 105, 2, 189-194

[152] J. F. Perez-Benito (2001), Copper(II)-catalyzed decomposition of hydrogen peroxide: Catalyst activation by halide ions, Monatshefte fur Chemie, 132, 12, 1477-1492

[153] V. Mucka (1976), Decomposition of hydrogen peroxide on copper(II) oxide, Czechoslov. Chem. Commun., 41, 1717-1726

[154] Y. Cudennec and A. Lecerf (2003), The transformation of $Cu(OH)_2$ into CuO, revisited, Solid State Sci., 5, 11-12, 1471-1474